Direct Numerical Simulation, Lie Group Analysis and Modeling of a Turbulent Channel Flow with Wall-normal Rotation

vom Fachbereich Maschinenbau
an der Technischen Universität Darmstadt

zur
Erlangung des Grades eines Doktor-Ingenieurs (Dr.-Ing.)
genehmigte

Dissertation

vorgelegt von

M.Sc. Amirfarhang Mehdizadeh
aus Mahallat / Iran

Berichterstatter:	Prof. Dr.-Ing. M. Oberlack
Mitberichterstatter:	Prof. Dr. rer. nat. A. Sadiki
Tag der Einreichung:	17.11.2009
Tag der mündlichen Prüfung:	10.02.2010

D17
Darmstadt, 2010

Kurzfassung

In dieser Arbeit wurden laminare und turbulente Kanalströmungen mit wand-normaler Rotation mittels numerischer und analytischer Ansätze untersucht. Im Gegensatz zu der um die Hauptsrömungsrichtung und Spannweitenrichtung rotierende Kanalströmung, ist die Kanalströmung mit wand-normaler Rotation nur selten untersucht worden. Es gibt keine Möglichkeit diese Strömungen experimentell zu studieren. Aus diesem Grund können diese nur numerisch oder analytisch untersucht werden. Allerdings ist ein analytischer Ansatz nur im laminaren Fall möglich. Um die Effekte der wand-normalen Rotation auf die turbulente Strömung zu erforschen und auch Referenzdaten für den turbulenten Fall bereit zu stellen, wurden Direkte Numerische Simulationen bei $Re_{\tau_0} = 180, 360$ mit unterschiedlichen Rotationszahlen durchgeführt, wobei Re_{τ_0} die Reynoldszahl basierend auf Reibungsgeschwindigkeit in nichtrotierender Kanalströmung ist.

Es wurde gezeigt, dass sowohl laminare als auch turbulente Kanalströmungen sehr empfindlich auf wand-normale Rotation reagieren. Für den turbulenten Fall ist die Strömung aufgrund der Induktion der Geschwindigkeit in die Spannweitenrichtung dreidimensional. Deshalb sind alle Komponenten des Reynoldsspannungstensors ungleich null. Durch Erhöhung der Rotationszahl tauchen Relaminarisierungssymptome auf und schliesslich erreicht die Strömung bei sehr grossen Rotationszahlen einen laminaren stationären Zustand.

Ferner wurde der Lie-Symmetrie-Ansatz auf die RANS-Gleichungen, die die Kanalströmung mit wand-normaler Rotation bei sehr hohen Reynoldszahlen beschreiben, angewendet. Basierend auf den Ergebnissen kann man schliessen, dass der Ansatz mit dem System von Differentialgleichungen mit ungeschlossenen Termen nicht gut umgehen kann.

Schliesslich wurde die die DNS-Daten ausgenutzt, um die Fähigkeit von einfachen Turbulenzmodellen zur Vorhersage wand-normaler, rotierender Kanalströmungen zu untersuchen. Mit anderen Worten wurden die einfachen Turbulenzmodellen mittel der DNS-Daten validiert. Die überzeugenden Ergebnisse zeigen, dass relativ einfache Turbulenzmodelle in der Lage sind, die Kanalströmung mit wand-normaler Rotation vorherzusagen.

Abstract

In this thesis laminar and turbulent channel flows with wall-normal rotation have been investigated by means of numerical and analytical approaches. Contrary to the streamwise and the spanwise rotating channel flow, channel flows with wall-normal rotation has been rarely studied. Since there is no possible experimental approach to the investigation of this flow, they can be studied only numerically and analytically. However, an analytical approach is only possible in the laminar case. In order to establish the effects of the wall-normal rotation on the turbulent channel flow and also to provide reference data for the turbulence case, direct numerical simulations at $Re_{\tau_0} = 180, 360$ based on the friction velocity in the non-rotating case for various rotation rates (from very small to relatively high) have been performed. It has been found that the both flow states are very sensitive to the wall-normal rotation and are highly affected even with a very small rotation rate. In the turbulent case due to the induction of the spanwise velocity the flow is three-dimensional and as a result all of the Reynolds stress tensor components are non-zero. By increase in the rotation rate relamonarization effects have been observed and finally at very high rotation rates the flow reaches a fully laminar steady state.

Further, the Lie symmetry approach has been applied to the Reynolds averaged Navier-Stokes equations describing a turbulent wall-normal rotating channel flow at very high Reynolds numbers to study the ability of this method to predicting the flow. Based on the results, one can conclude that Lie symmetry approach can not deal with the system of differential equations with unclosed terms.

Finally the DNS results have been used to investigate the capability of relatively simple turbulence models to predict the flow. In other words we have used the DNS data to validate the simple RANS turbulence models. For weak rotation rates the convincing results indicate that in contrast to the streamwise and the spanwise rotating channel flows, the present flow could be predicted by this simple turbulence model. However, predicting of the flow at higher rotation numbers requires obviously advanced RANS models including relaminarization effects

Acknowledgments

First of all I would like to thank my supervisor Prof. Dr. Ing. M. Oberlack for accepting me as a PhD student in his group and also for his precious and useful discussions during my work. I would also like to thank Prof. Dr. rer. nat. Amsini Sadiki, who agreed to be my co-referee.

A special thanks to the Deutsche Forschungsgemeinschaft (DFG) for the financial support, making my work possible.

I would like to express my gratefulness to the support team from HHLR, TU-Darmstadt who helped me to run the code on the supercomputer.

Many thanks to my colleagues, George Khujadze and Michael Frewer from whom I benefited during numerous valuable discussions.

Special thanks to Andreas Rosteck for the help to the final formating of my dissertation.

Finally, I would like to address my sincere gratitude to my parents and my wife for their patience and respect.

Contents

List of Figures

List of Tables

1 Introduction

1.1 The Phenomena of Turbulence

Fluid flows in nature and engineering are turbulent. Turbulence appears in every fluid flow if the inertial, buoyancy, centrifugal or other forces overcome the local viscous force that suppress natural disturbances and flow instabilities. If the inertial and body forces are sufficiently large compared to viscous force, they amplify random disturbances that are present in every flow. Finally they become unstable and nonlinear, interact and agglomerate into a chaotic, three-dimensional complex motion. This includes low momentum diffusion, high momentum convection as well as rapid variation of pressure and velocity in space and time. The condition leading to laminar or turbulent flow can be determined by the Reynolds number.

In turbulent flow, unsteady vortices appear on many scales and interact with each other. Drag due to boundary layer skin friction increases. The structure and location of boundary layer separation often changes, sometimes resulting in a reduction of overall drag. Because laminar-turbulent transition is governed by the Reynolds number, the same transition occurs if e.g. the size of the object is gradually increased, the viscosity of the fluid is decreased, or the density of the fluid is increased.

Although the mathematical basic equations to describe turbulence were derived independently more than 150 years ago from the French mathematician and physician Claude L.M.H. Navier (1775-1836) and the Irish mathematician and physician George G. Stokes (1819-1903), turbulence remains an important unsolved problem of classical physics. During the last centuries, many leading researchers worked on this problem. To mention are e.g. Leonardo da Vinci (1452-1519), Osborne Reynolds (1842-1912), Ludwig Prandtl (1875-1953), Theodor von Kármán (1881-1963) and Werner Heisenberg (1901-1976) to name only a few.
Turbulence can appear in all fluid media at all speeds ranging from almost stagnant fluids such as in a large water accumulations-lakes and oceans and in atmospheric air at high latitude (Clear Air Turbulence, CAT), to hypersonic speeds. It is commonly encountered in almost all flows of practical engineering and environmental relevance:

- in most internal flows such as pipes and conduits, heat exchangers and other thermal and chemical equipments, pumps, compressors, turbines, internal combustion engines, hydraulic machinery and etc.
- in most external flows such as around and in wakes of aircrafts, ships, trains and road vehicles, tennis, golf and soccer balls.

- in earth atmosphere and also on and around other planets (planetary boundary layer) .
- in natural water flows-rivers, lakes and oceans.

In figures 1.1-1.4 four examples are displayed. Figure 1.1 shows turbulent swirls and eddies in a fast flowing river, while in figure 1.2 turbulence is observed in the ash plume of the Mt. Spurr volcano as it erupts. Further in figure 1.3 turbulent air currents in the atmosphere is visualized and in figure 1.4 the highly turbulent outer layer of the sun, i.e. the convection zone.

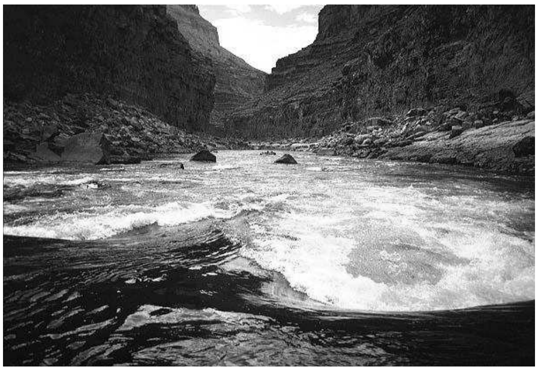

Figure 1.1: Fast flowing river.

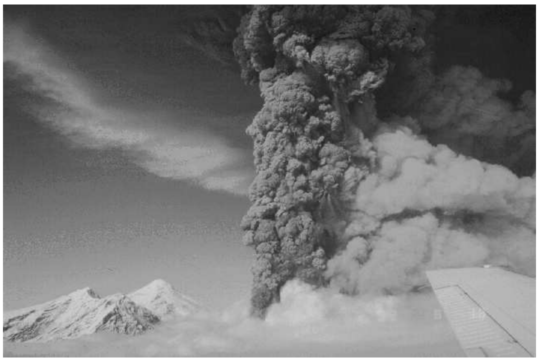

Figure 1.2: Mt. Spurr volcano.

Figure 1.3: Atmosphere.

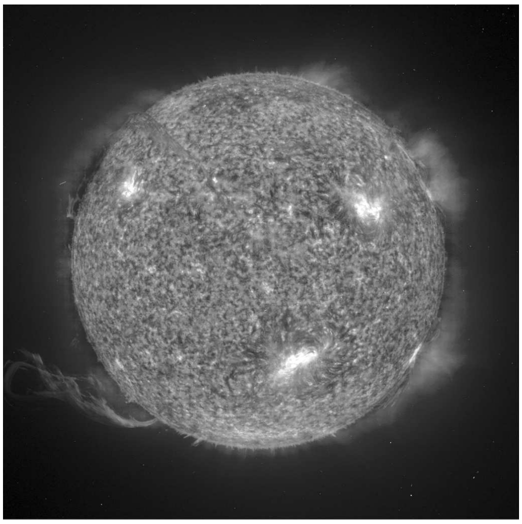

Figure 1.4: Sun.

Although turbulence is ubiquitous and a part of our daily life, there is no unique and clear definition of turbulence. We can state that turbulence denotes a state of fluid in which all properties (velocity, pressure, density, ...) fluctuate continuously in an irregular, chaotic, non-repeating and unpredictable manner.

1.2 Solution to the Turbulence: needs for modeling and simulation

The basic mechanism in turbulence is a continuous stretching of vortex filaments, both internally (self-stretching) and externally (due to mean flow deformation or action of body forces). Turbulence consists of a hierarchy of eddies of various orders and sizes. Eddies of different sizes are responsible for different interactions in turbulence, but they all contribute to the overall effects. Even in a flow with steady boundary conditions, the turbulent field is different at every time instant. In the other words, Navier-Stokes equations, which are believed to describe the turbulence motion of fluid in differential form with a very high degree of accuracy, are satisfied by infinite number of solutions-realizations of turbulent flows. Because of their nature, they can not be solved analytically. The alternative is the numerical solution of the original or statistically averaged equations. A direct numerical solution of the original Navier-Stokes equations, which is the only reliable computational method, requires, therefore a numerical discretisation which should resolve even the smallest eddies. Hence the application of direct numerical simulation depends on the span of eddy sizes in the considered flow. As mentioned, although one can solve numerically the complete set of the Navier-Stokes equations in three-dimensional space and time (so called Direct Numerical Simulation, DNS), because of large demand on computer resources this method is at present limited to relative low Reynold numbers and simple geometries. For practical problems of industrial and environmental relevance, the only possible approach is to consider Reynolds-averaged Navier-Stokes (RANS) equations, the solution of which provides information about the averaged flow field and requires such computer resources which are normally affordable to any user. Since the averaged field is strongly affected by the irregular motion (fluctuating field), predicting of the averaged field is a non-trivial task. The influence of the irregular turbulent motion must be represented if the mean flow is to be accurately predicted. The representation must be constructed in a manner that permits a wide range of applications. Models for such general purposes are usually phrased in terms are differential equations. For instance, a widely used model for computing engineering flows, the $k-\epsilon$ model, consists of differential transport equations for turbulent energy k and its rate of dissipation, ϵ. From their solution, an eddy viscosity is created for the purpose of predicting the mean flow. Other models in this category (RANS Models) represent turbulent influence by a stress tensor, the Reynolds stress. Transport models, or algebraic formulas are developed for these stresses. However, the RANS models because of their empirical nature, can hardly provide any information about the turbulence spectral dynamics and, thus they can not be regarded as a reliable approach for investigations the physics of turbulence and turbulent transport processes. A compromise of the route between DNS and RANS is the method of large eddy simulation (LES) which resolves in space and time only the large-scale eddy motion, but employs statistical models for subscale motion, usually defined in terms of numerical mesh size. This brings in a significant savings both in time and computer memory. For this reason, LES can deal with higher Reynolds numbers and more complex geometries. However, LES is still quit demanding in terms of computer resources, closer to the DNS than to RANS. This is because both DNS and LES require always to solve the instantaneous Navier-Stokes equations in time and three dimensional space, even if the time and ensemble-averaged properties are steady and two or one-dimensional. Unlike DNS and LES, RANS can be used in steady form and the problem can be solved only in two or even one-dimensional if the averaged flow conditions satisfy these constrains. Recognizing the limitations of RANS and LES and in research for more efficient methods, the CFD community has recently turned its attention to hybrid RANS/LES modeling as an alternative strategy for flows at high Reynolds numbers.

1.3 Characterization and Scales of Turbulence

Because of our inability to analytically describe turbulence in real flow, physical intuition supported by similarity arguments and dimensional analysis have been extensively used to characterize the turbulence and its properties in various flows. Experiments and more recently the DNS have played crucial role in verifying of disproving the findings. Such analyses have led to establishing laws which govern various processes and interaction in turbulence, as well as to deduce some general conclusions about turbulence structure and its behavior. Examples of such laws are the definition of characteristic turbulence length, time and velocity scales for the full spectrum or its parts, their relationship, characteristic distribution of mean-flow and turbulence properties in some simple generic flows.

1.3.1 Turbulence Scales

Turbulence and its interaction are characterized by turbulent time and length scales. Different interactions are governed by different scales. Turbulence generation and its transport are associated with large eddies, while the viscous dissipation occurs at the smallest scales. Large eddies in a shear layer or in an enclosure grow until they fill the layer or the entire flow domain. Hence the largest length scale can be related to the characteristic flow dimension. Generation of turbulence in a shear layer occurs due to the mean flow deformation and its interaction with most energetic eddies (energy containing eddies). Through the process of their generation large eddies extract energy from the mean motion. Energy containing eddies are large in size though not the largest and they are most efficient in extracting energy from the mean motion. However, they also control the amount of energy which they give away to the smaller eddies. This energy will be dissipated by viscosity. We denote the dissipation rate of the turbulent kinetic energy by ϵ . Hence, we can define the time and length scale of the energy containing eddies in terms of the total content of turbulence kinetic energy k and its dissipation rate, i.e as f(k, ϵ). Dimensional analysis yields to the following time and length scale for energy containing eddies:

$$\tau = \frac{k}{\epsilon} \quad , \qquad l = \frac{k^{3/2}}{\epsilon}.$$

The process of dissipation of turbulence mechanical energy into heat due to viscosity (ν) is associated with finest eddy structure, i.e very small vortex tubes and sheets. Their (Kolmogorov) scales are determined by two quantities, namely ν and ϵ. Dimensional arguments yields the following time and length scales for smallest eddies:

$$\vartheta = (\frac{\nu}{\epsilon})^{\frac{1}{2}} \qquad \text{and} \qquad \eta = \frac{\nu^3}{\epsilon}^{\frac{1}{4}}.$$

An intermediate length scale, called Taylor microscale, can be defined in terms of all three characteristic parameters, k, ν , ϵ as below:

$$\lambda = \sqrt{10\nu\frac{k}{\epsilon}}.$$

The various turbulence scales and corresponding Reynolds numbers have been summarized in the following table.

Table 1.1: Turbulence Scales.

Eddy size	Length scale	Time scale	Velocity scale	Reynolds No.
Large energetic eddies	$l = \frac{k^{3/2}}{\epsilon}$	$\tau = \frac{k}{\epsilon}$	$k^{\frac{1}{2}}$	$Re_t = \frac{k^{\frac{1}{2}}l}{\nu}$
Small eddies	$\lambda = \sqrt{10\nu\frac{k}{\epsilon}}$	$\vartheta = (\frac{\nu}{\epsilon})^{\frac{1}{2}}$	$k^{\frac{1}{2}}$	$Re_\lambda = \frac{k^{\frac{1}{2}}\lambda}{\nu}$
Dissipative eddies	$\eta = (\frac{\nu^3}{\epsilon})^{\frac{1}{4}}$	$\vartheta = (\frac{\nu}{\epsilon})^{\frac{1}{2}}$	$(\nu\epsilon)^{\frac{1}{4}}$	$Re_k = 1$

Relations between various scales are as belows:

$$\frac{l}{\lambda} = \frac{Re_t^{\frac{1}{2}}}{\sqrt{10}} = \frac{Re_\lambda}{10},$$

$$\frac{\lambda}{\eta} = \sqrt{10}Re_t^{\frac{1}{4}} = 10^{\frac{1}{4}}Re_\lambda^{\frac{1}{2}},$$

$$\frac{l}{\eta} = Re_t^{\frac{3}{4}} = \frac{Re_\lambda^{\frac{3}{2}}}{10^{\frac{3}{4}}},$$

$$\frac{\mathcal{T}}{\vartheta} = Re_t^{\frac{1}{2}} = \sqrt{10} Re_\lambda.$$

1.4 Motivation

Turbulent flows in a rotating frame exist in a variety of industrial, geophysical and astrophysical applications. In these flows the structures of turbulence and mechanism of momentum transport are highly affected by additional body forces, namely, Coriolis and centrifugal forces. One of the simplest wall dominated flow mode in this category is the fully developed turbulent flow in a rotating channel, where the rotating axis is one of three directions: the streamwise, wall-normal or spanwise direction. Among these, the spanwise rotating channel flow has been extensively studied through experiments, Johnson, Halleen & Lezius (1972) and Nakabayashi & Kitoh (1996) and direct numerical simulations (DNS), Kim (1982).

By increasing the rotation number, the turbulence is amplified in the pressure side and suppressed in the suction side of the channel and an asymmetric distribution of the mean flow and Reynolds stresses are observed, Johnson et al. (1972). As a result of the Taylor-Görtler instability, the large-scale cells appear. If the rotation rate is further increased beyond a critical point, turbulence on the pressure side is reduced and certain characteristic roll cells become much smaller and eventually disappear due to the thickening of the relaminarized region on the suction side, Elsamni & Kasagi (2001) and Kristoffersen & Andersson (1993) and the flow eventually relaminarized as is shown in the extensive DNS study of Grundesttam, Wallin & V. Johansson (2008).

Compared to the spanwise rotating channel flow, the effect of the streamwise rotation on the turbulent channel flow is much weaker. A first integrated study using DNS, Lie symmetry method and RANS models were presented by Oberlack, Cabot & Rogers (1998), and later considerably extended in Oberlack, Cabot, Pettersson Reif & Weller (2006). This rotation induces a mean velocity in spanwise direction and as a result, all six Reynolds stresses become non-vanishing. The streamwise mean velocity stays symmetrical with respect to the channel center line. By increasing the rotation number the streamwise mean velocity becomes more flattened but remains symmetric. It has also been observed that in this flow, with the exception of the log-law, in the flow regions with the weakest wall influence the highest degree of symmetry is usually obtained. Therefore, it is expected that, two linear regions may emerge in the proximity of the center region, Oberlack et al. (2006). Parallel to the DNS and theoretical studies an experiment was set up to validate the results. The experiment results were presented and compared to the DNS, showing a good overall agreement, Recktenwald, Weller, Schroeder & Oberlack (2007). In this context it should be noted that a stability analysis of the streamwise rotating channel flow has been conducted by Hickey, Khujadze & Oberlack (2008), showing that the induced cross flow appears to be closely related to a fundamental instability of the flow.

Although the turbulent channel flow with wall-normal rotation can be regarded as a archetype of three dimensional boundary layers (Ekman type boundary layers), it has been rarely investigated and if studied only for very small rotation rates. Since there is no possible experimental approach to investigate a wall-normal rotating channel flow with homogeneous directions, direct numerical simulation (DNS) and analytical analysis are the only available methods to examine them. Elsamni & Kasagi (2001) and Wu & Kasagi (2004) have performed investigations to study the effects of arbitrary directional system rotation on the turbulent channel flow. In a pure and very weak wall-normal rotation it has been established that the flow is very sensitive to this rotation. Furthermore, they argued that the turbulent channel flow with wall-normal rotation could be regarded as a 2D channel flow. Li, Liu & Lu (2006) have studied the effects of wall-normal rotation on a turbulent channel flow driven by a constant pressure gradient. They also found that the channel flow is very sensitive to the wall-normal rotation. A slight rotation can induce a strong secondary motion in the spanwise direction and reduce the streamwise mean velocity substantially. As a result, all six Reynolds stresses will become non zero. However, their study concerns also very small rotation rates.

The present study complements the previous investigation performed by Li et al. (2006). Here turbulent wall-normal rotating channel flow will be investigated numerically for a wide range of rotation rates, varying from very small to high providing a reference data base, and also analytically using Lie symmetry approach. Finally the ability of a relatively simple turbulence model to predict the flow will also be studied. The thesis is organized as follows:

In the next chapter the governing equations, which are the Navier-Stokes equations, the Reynolds averaged Navier-Stokes equations and the two-point correlation equations are given. In the third chapter the laminar wall-normal rotating channel flow is investigated. In chapter four DNS results at different rotation rates for $Re_{\tau_0} = 180$ and $Re_{\tau_0} = 360$ are presented and discussed. The fifth chapter gives a short introduction into Lie-Group analysis and presents the results obtained by Lie Symmetry approach. Chapter 6 is to give a brief introduction about two- equation RANS models and then to study that in what extent a simple two-equation RANS model can predict the flow. The thesis concludes with the summary of our discussions and the results.

2 Basic Equations

2.1 Navier-Stokes Equations

The Navier-Stokes equations, named after Claude-Louis Navier and George Gabriel Stokes, are a set of equations that describe the motion of a Newtonian fluid. The assumption of incompressibility implies that the Mach number is zero and the temperature variations do not affect the material properties and hence the scalar transport is not investigated. The equations governing viscous incompressible flow in cartesian coordinate system, whether turbulent or laminar are as follows:
continuity equation, which expresses the incompressibility of fluid volume:

$$\frac{\partial u_k}{\partial x_k} = 0 \tag{2.1}$$

and the momentum equation:

$$\frac{Du_i}{Dt} = -\frac{1}{\rho}\frac{\partial p}{\partial x_i} + \nu\frac{\partial^2 u_i}{\partial x_k \partial x_k} - 2\Omega_k e_{ikl} u_l - \Omega_i \Omega_k x_k + x_i \Omega_k \Omega_k \tag{2.2}$$

with

$$\frac{D}{Dt} = \frac{\partial}{\partial t} + u_k \frac{\partial}{\partial x_k}, \tag{2.3}$$

where t and x are time and coordinates in space. u_i, p, ρ, ν and Ω_k are respectively the instantaneous velocity vector, pressure, density, kinematic viscosity and the rotation vector of the reference frame. e_{ikl} is an antisymmetric tensor of third rank, which is denoted permutation tensor.

The permutation tensor e_{ijk} is defined by:

$$e_{ijk} = \begin{cases} 1, & \text{for} \quad ijk = 123, 312, 231 \\ -1, & \text{for} \quad ijk = 321, 132, 213 \\ 0, & \text{otherwise} \end{cases} . \tag{2.4}$$

Since centrifugal forces do not affect the turbulence dynamic, they can be expressed as a potential field and in the case of incompressible fluid can be absorbed into the pressure in the following form:

$$p_{eff} = \frac{p}{\rho} + \frac{1}{2}(\Omega_k \Omega_l x_k x_l - \Omega_k \Omega_k x_l x_l). \tag{2.5}$$

Replacing of the effective pressure gradient (p_{eff}) in the equation (2.2) leads to a new momentum equation as below:

$$\frac{Du_i}{Dt} = -\frac{\partial p}{\partial x_i} + \nu \frac{\partial^2 u_i}{\partial x_k \partial x_k} - 2\Omega_k e_{ikl} u_l. \tag{2.6}$$

Note that for simplicity p_{eff} is replaced by p. Henceforth p represent the effective pressure gradient (p_{eff}). Together with the continuity equation, the Navier-Stokes equations yield a system of four equations with four unknowns, namely pressure and three velocity components. Thus, the system of equations (2.1) and (2.2) is closed. Unfortunately, this does not automatically guarantee that the solutions to those equations satisfy the given physics. In fact, it is not even guaranteed a priori that a satisfactory solution exists, see Foias, Manley, Rosa & Temam (2001). It is very important to know the nature of the solutions to the Navier-Stokes equations because the equations must be solved by numerical methods and the nature of the solutions directly influences, which type of method will be most effective.

2.2 Reynolds averaged Navier-Stokes Equations

The Navier-Stokes equations govern fluid turbulence. The problem is that the phenomenon of turbulence is the complete solution to these equations – a chaotic, spatially and temporally complex solution. Such solutions are not easy to obtained, even on massively parallel supercomputers. A much simpler level of description is needed. This calls for a statistical approach. There are no closed equations for the statistics of turbulent flow. The equations can be obtained by decomposing of the velocity and pressure fields into a sum of its mean and a fluctuation, substituting in the original Navier-Stokes equations and then average them. This decomposition was first proposed by Osborne Reynolds and the equations have been named Reynolds averaged Navier-Stokes (RANS) equation. The Reynolds decomposition can be rewritten as follows:

$$u = \bar{u} + u', \quad p = \bar{p} + p'. \tag{2.7}$$

The quantities marked with a bar denote the mean quantities, while the quantities marked with primes are the fluctuations. The average is in general build as:

$$\bar{u} = \lim_{N\to\infty} \big(\frac{1}{N}\sum_{n=1}^{N} u_n\big), \quad \bar{p} = \lim_{N\to\infty} \big(\frac{1}{N}\sum_{n=1}^{N} p_n\big). \tag{2.8}$$

Substituting the Reynolds decomposition (2.7) into (2.1) and (2.6) and averaging gives the Reynolds averaged continuity

$$\frac{\partial \bar{u}_k}{\partial x_k} = 0 \tag{2.9}$$

and momentum equations

$$\frac{\bar{D}\bar{u}_i}{\bar{D}t} = -\frac{\partial \bar{p}}{\partial x_i} + \nu \frac{\partial^2 \bar{u}_i}{\partial x_k \partial x_k} - 2\Omega_k e_{ikl}\bar{u}_l - \frac{\partial \overline{u_i' u_k'}}{\partial x_k}. \tag{2.10}$$

The equations (2.9) and (2.10) together are the RANS equations. The extra term in the equation (2.10) compared to the equation (2.6) is called Reynolds stress tensor and coming after averaging the advection term in the momentum equations. Existence of this term, causes that the system of equations (2.9) and (2.10) are unclosed. The statistical problem for the mean or first moment needs the knowledge of the second moment. This is because the Navier-Stokes equations have a quadratic non-linearity. Any non-linearity causes moment equations to be unclosed. Here it means the first moment contains second moments, the second moment equation contains third moments, and so on up to the infinity. A dynamical equation for the Reynolds stress tensor can be derived from the fluctuating velocity in the following form:

$$\frac{\partial \overline{u_i' u_j'}}{\partial t} + \bar{u}_k \frac{\partial \overline{u_i' u_j'}}{\partial x_k} = P_{ij} - \epsilon_{ij} + \Phi_{ij} + D^t_{ij} + D^\nu_{ij} + D^p_{ij} + C_{ij}, \tag{2.11}$$

where the abbreviated notations are as follows:

$$\begin{aligned}
P_{ij} &= -\Big[\overline{u_i' u_k'}\frac{\partial \bar{u}_j}{\partial x_k} - \overline{u_j' u_k'}\frac{\partial \bar{u}_i}{\partial x_k}\Big], \\
\epsilon_{ij} &= \nu \overline{\frac{\partial u_i'}{\partial x_k}\frac{\partial u_j'}{\partial x_k}}, \\
\Phi_{ij} &= \overline{\frac{p'}{p}\Big(\frac{\partial u_i'}{\partial x_j} + \frac{\partial u_j'}{\partial x_i}\Big)}, \\
D^t_{ij} &= -\frac{\partial \overline{u_i' u_j' u_k'}}{\partial x_k}, \\
D^\nu_{ij} &= \nu \frac{\partial^2 \overline{u_i' u_j'}}{\partial x_k \partial x_k}, \\
D^p_{ij} &= -\frac{\partial}{\partial x_k}\Big[\overline{\frac{p'}{\rho}(\delta_{kj}u_i' + \delta_{ki}u_j')}\Big], \\
C_{ij} &= -2\Omega_k \Big[e_{kli}\overline{u_j' u_l'} + e_{klj}\overline{u_i' u_l'},\Big]
\end{aligned} \tag{2.12}$$

where P_{ij} represents the energy production, ϵ_{ij} the dissipation, Φ_{ij} the pressure strain correlation, D_{ij} the diffusion (turbulent, molecular and pressure diffusion) or the third moment and C_{ij} the Coriolis term. Because the dissipation, pressure strain correlation and turbulent diffusion (pressure and triple term diffusion) term are unknown, further equations are necessary.

2.3 Multi- and Two-Point Correlation Equations

Because of the complex nature of turbulent flows, sometimes it is an advantage to study multi-point statistics. The motion of any point in a turbulent flow affects the motion at other distant points through the pressure field. For this reason an adequate description cannot be obtained by considering only mean values associated with a single point. To obtain a proper description of a turbulent flow it is necessary to consider two or more turbulent quantities at two or more positions. The multi-point correlation (MPC) equations can be used for studying the spatial configurations of the flow field. The MPC is suitable to model statistical quantities of turbulence at all scales. To write the MPC equations in a compact form we introduce the definition

$$R_{i_{n+1}} = R_{i_{(0)}i_{(1)}\ldots i_{(n)}} = \overline{u'_{i_{(0)}}(\boldsymbol{x}_{(0)}) \cdot \ldots \cdot u'_{i_{(n)}}(\boldsymbol{x}_{(n)})} \tag{2.13}$$

at $n+1$ points, where $u'_{i_{(k)}}$ denotes velocity fluctuations around the mean velocity $\bar{u}_{i_{(k)}}$ at the point $\boldsymbol{x}_{(k)}$.

Including the definition of equation (2.13) it is possible to derive the MPC equations from the Navier-Stokes equations (Oberlack 2000)

$$\begin{aligned}
\Theta_{i_{\{n+1\}}} =& \frac{\partial R_{i_{\{n+1\}}}}{\partial t} + \sum_{l=0}^{n} \Bigg[\bar{u}_{k_{(l)}}(\boldsymbol{x}_{(l)}) \frac{\partial R_{i_{\{n+1\}}}}{\partial x_{k_{(l)}}} + R_{i_{\{n+1\}}[i_{(l)} \mapsto k_{(l)}]} \frac{\partial \bar{u}_{i_{(l)}}(\boldsymbol{x}_{(l)})}{\partial x_{k_{(l)}}} \\
&+ \frac{\partial P_{i_{\{n\}}[l]}}{\partial x_{i_{(l)}}} - \nu \frac{\partial^2 R_{i_{\{n+1\}}}}{\partial x_{k_{(l)}} \partial x_{k_{(l)}}} - R_{i_{\{n\}}[i_{(l)}] \mapsto \emptyset} \frac{\partial \overline{u'_{i_{(l)}} u'_{k_{(l)}}}(\boldsymbol{x}_{(l)})}{\partial x_{k_{(l)}}} \\
&+ \frac{\partial R_{i_{\{n+2\}}[i_{(n+1)} \mapsto k_{(l)}]}[\boldsymbol{x}_{(n+1)} \mapsto \boldsymbol{x}_{(l)}]}{\partial x_{k_{(l)}}} + 2\Omega_k e_{i_{(l)}km} R_{i_{\{n+1\}}[i_{(l)} \mapsto m]} \Bigg] = 0 \\
&\text{for} \quad n = 1, \ldots, \infty.
\end{aligned} \tag{2.14}$$

by using the additional definitions

$$\begin{aligned}
&R_{i_{\{n+1\}}[i_{(l)} \mapsto k_{(l)}]} = \\
&\quad \overline{u'_{i_{(0)}}(\boldsymbol{x}_{(0)}) \cdot \ldots \cdot u'_{i_{(l-1)}}(\boldsymbol{x}_{(l-1)}) u'_{k_{(l)}}(\boldsymbol{x}_{(l)}) u'_{i_{(l+1)}}(\boldsymbol{x}_{(l+1)}) \cdot \ldots \cdot u'_{i_{(n)}}(\boldsymbol{x}_{(n)})},
\end{aligned} \tag{2.15}$$

$$R_{i_{\{n+2\}}[i_{(n+1)} \mapsto k_{(l)}]}[\boldsymbol{x}_{(n+1)} \mapsto \boldsymbol{x}_{(l)}] = \overline{u'_{i_{(0)}}(\boldsymbol{x}_{(0)}) \cdot \ldots \cdot u'_{i_{(n)}}(\boldsymbol{x}_{(n)}) u'_{k_{(l)}}(\boldsymbol{x}_{(l)})}, \tag{2.16}$$

$$R_{i_{\{n\}}[i_{(l)} \mapsto \emptyset]} = \overline{u'_{i_{(0)}}(\boldsymbol{x}_{(0)}) \cdot \ldots \cdot u'_{i_{(l-1)}}(\boldsymbol{x}_{(l-1)}) u'_{i_{(l+1)}}(\boldsymbol{x}_{(l+1)}) \cdot \ldots \cdot u'_{i_{(n)}}(\boldsymbol{x}_{(n)})}, \tag{2.17}$$

and

$$P_{i_n[l]} = \overline{u'_{i_{(0)}}(\boldsymbol{x}_{(0)}) \cdot \ldots \cdot u'_{i_{(l-1)}}(\boldsymbol{x}_{(l-1)}) p'(\boldsymbol{x}_{(l)}) u'_{i_{(l+1)}}(\boldsymbol{x}_{(l+1)}) \cdot \ldots \cdot u'_{i_{(n)}}(\boldsymbol{x}_{(n)})}, \tag{2.18}$$

The notation in the square brackets denotes the replacement of certain variables or indices with some other quantities standing on the right side of the arrow. Each Θ-equation of the tensor oder $n+1$ only contains one unclosed term of the order n+2. For any of the remaining terms (Oberlack 2000), e.g. $P_{i_n[l]}$, exact equations can be derived from the continuity equation or the Poisson equation for the pressure.

The Two-point correlation (TPC) tensor admits two additional identities,

$$\lim_{x_{(k)}\to x_{(l)}} R_{i_{\{2\}}} = \lim_{x_{(k)}\to x_{(l)}} R_{i_{(0)}i_{(1)}} = \overline{u'_{i_{(0)}} u'_{i_{(1)}}}(\boldsymbol{x}_{(l)}) \text{ with } k \neq l \tag{2.19}$$

where $x_{(k)}$ and $x_{(l)}$ can be an arbitrary position vector taken from $x_{(0)}, ..., x_{(n)}$ and the null identity

$$R_{i_{\{1\}}[i_{(l)}\mapsto\emptyset]} = 0. \tag{2.20}$$

The latter is traced back to the fact that the average of a single fluctuating velocity is zero.

The following two sets of equations are derived from the continuity equation, which have to be employed as additional kinematic constrains

$$\frac{\partial R_{i_{\{n+1\}}[i_{(l)}\mapsto i_{(l)}]}}{\partial x_{k_{(l)}}} \text{ for } l = 0, ..., n \tag{2.21}$$

and

$$\frac{\partial P_{i_{\{n\}}[k][i_{(l)}\mapsto m_{(l)}]}}{\partial x_{m_{(l)}}} \text{ for } k, l = 0, ..., n \text{ and } k \neq l. \tag{2.22}$$

For simplification it will be continued with the TPC equations. The TPC equations have a similar structure as the full set of MPC equations, particularly they have the same symmetry properties. In order to simplify the notation, the following short form is introduced

$$R_{i_{\{2\}}} = R_{ii_{\{1\}}} = R_{ij}. \tag{2.23}$$

For the derivation of the TPC equations the transport equation for the turbulent fluctuating velocities at the point $\boldsymbol{x}$ is multiplied with the fluctuating velocity at the point $\boldsymbol{x}_1$ and vice versa. In the case of adding the resulting equations together, we obtain (Rotta 1972)

$$
\begin{aligned}
\Theta_{i_{\{2\}}} =& \frac{\bar{D}R_{ij}}{\bar{D}t} + R_{kj}\frac{\partial \bar{u}_i(\boldsymbol{x},t)}{\partial x_k} + R_{ik}\frac{\partial \bar{u}_j(\boldsymbol{x},t)}{\partial x_k}\Bigg|_{\boldsymbol{x}+\boldsymbol{r}} \\
&+[\bar{u}_k(\boldsymbol{x}+\boldsymbol{r},t)-\bar{u}_k(\boldsymbol{x},t)]\frac{\partial R_{ij}}{\partial r_k} + \frac{\partial \overline{p'u'}_j}{\partial x_i} - \frac{\partial \overline{p'u'}_j}{\partial r_i} + \frac{\partial \overline{u_i'p'}}{\partial r_j} \\
&-\nu\left[\frac{\partial^2 R_{ij}}{\partial x_k \partial x_k} - 2\frac{\partial^2 R_{ij}}{\partial x_k \partial r_k} + \frac{\partial^2 R_{ij}}{\partial r_k \partial r_k}\right] \\
&+\frac{\partial R_{(ik)j}}{\partial x_k} - \frac{\partial}{\partial r_k}[R_{(ik)j} - R_{i(jk)}] + 2\Omega_k\Big[e_{kli}R_{lj} + e_{klj}R_{il}\Big] = 0,
\end{aligned}
\tag{2.24}
$$

where the difference between two points has been introduced according to

$$
\boldsymbol{x} = \boldsymbol{x}_{(0)}, \quad \boldsymbol{r} = \boldsymbol{x}_{(1)} - \boldsymbol{x}_{(0)}. \tag{2.25}
$$

$\frac{\bar{D}}{\bar{D}t} = \left(\frac{\partial}{\partial t} + \bar{u}_k \frac{\partial}{\partial x_k}\right)$ is the mean substantial derivative. $\boldsymbol{x}$ and $\boldsymbol{r}$ are coordinates in physical and correlation spaces respectively.

The fluctuating pressure-velocity vectors are special cases of $P_{i_{\{n\}}[k]}$ and are specified as

$$
\overline{p'u_j'}(\boldsymbol{x},\boldsymbol{r},t) = \overline{p'(\boldsymbol{x},t)u_j'(\boldsymbol{x}+\boldsymbol{r},t)}, \quad \overline{u_i'p'}(\boldsymbol{x},\boldsymbol{r},t) = \overline{u_i'(\boldsymbol{x},t)p_j'(\boldsymbol{x}+\boldsymbol{r},t)}, \tag{2.26}
$$

while the triple correlation vectors respectively defined as

$$
R_{(ik)j} = \overline{u_i'(\boldsymbol{x},t)u_k'(\boldsymbol{x},t)u_j'(\boldsymbol{x}+\boldsymbol{r},t)}, \quad R_{i(jk)} = \overline{u_i'(\boldsymbol{x},t)u_j'(\boldsymbol{x}+\boldsymbol{r},t)u_k'(\boldsymbol{x}+\boldsymbol{r},t)}. \tag{2.27}
$$

For the TPC equations case the continuity equations (2.21) and (2.22) simplify to

$$
\frac{\partial R_{ij}}{\partial x_i} - \frac{\partial R_{ij}}{\partial r_i} = 0, \quad \frac{\partial R_{ij}}{\partial r_j} = 0, \quad \frac{\partial \overline{p'u_i'}}{\partial r_i} = 0, \quad \frac{\partial \overline{u_j'p'}}{\partial x_j} - \frac{\partial \overline{u_j'p'}}{\partial r_j} = 0. \tag{2.28}
$$

The TPC tensor is defined as:

$$
R_{ij}(\boldsymbol{x},\boldsymbol{r},t) = \overline{u_i'(\boldsymbol{x},t)u_j'(\boldsymbol{x}+\boldsymbol{r},t)}. \tag{2.29}
$$

2.4 Flow Geometry and Dimensionless Parameters

The flow domain and the coordinate system in the present study are shown in the figure 2.1. The flow between two parallel infinite walls is driven by a streamwise constant pressure gradient.

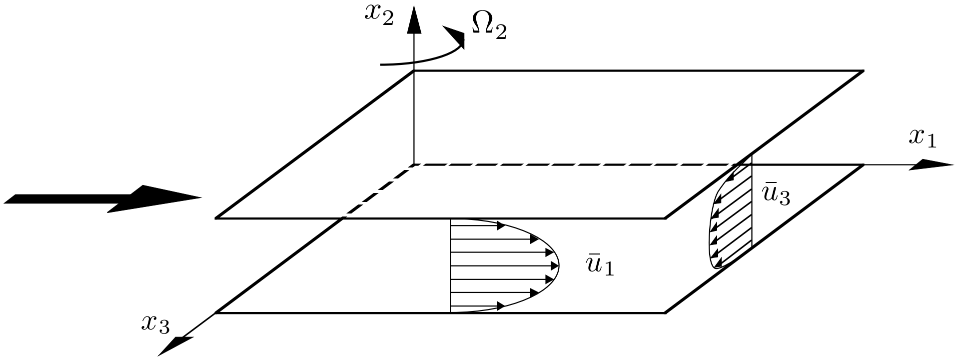

Figure 2.1: Sketch of the flow geometry of a channel flow rotating about the wall-normal axes.

The governing equations, i.e. the Navier-Stokes equations for an incompressible flow in the present geometry in a dimensionless form can be written as follows:

$$\frac{\partial u_i}{\partial t} = -\frac{\partial p}{\partial x_i} + \frac{1}{Re_{\tau 0}}\frac{\partial^2 u_i}{\partial x_j^2} - u_j\frac{\partial u_i}{\partial x_j} - \epsilon_{i2k}Ro_2 u_k \tag{2.30}$$

$$\frac{\partial u_i}{\partial x_i} = 0, \tag{2.31}$$

where Ro_2 is dimensionless rotation number in the x_2 direction and ϵ_{i2k} is the alternating unit tensor. The componential rotation number is defined as follows:

$$Ro_2 = \frac{2\Omega_2 h}{u_{\tau 0}} \quad . \tag{2.32}$$

In the present study, all of the variables, i.e the velocities u_i, pressure p, time t, and space x_i are non-dimensionalized by the channel half height h and $u_{\tau 0}$, which is the friction velocity in the non-rotating case. Note that the latter is a constant value independent of Ro_2, since it is a function of the constant streamwise pressure gradient, density and the channel half height. Because of incompressibility and homogeneity in the x_1 and the x_3 directions, the centrifugal force and the constant fluid density are already absorbed in the pressure.

The instantaneous velocity field can be decomposed into mean and fluctuating parts as below:

$$u_i = \bar{u}_i + u_i' \quad , \tag{2.33}$$

where $\bar{u}_i$ is the mean velocity.
The Reynolds number based on the friction velocity in the non-rotating case i.e. Re_{τ_0} is defined as follows:

$$Re_{\tau_0} = \frac{u_{\tau_0} h}{\nu} \quad , \tag{2.34}$$

where ν is the kinematic viscosity of the fluid.
For the rotating cases the friction velocities in the streamwise ($u_{\tau 1}$), in the spanwise ($u_{\tau 3}$) and effective friction velocity ($u_{\tau_{eff}}$) depending on the rotation rate are defined in the following form:

$$u_{\tau_i} = \sqrt{\frac{1}{Re_{\tau_0}} \left| \frac{\partial \bar{u}_i}{\partial x_2} \right|_{wall}} \quad \text{and} \quad i = 1,3 \quad , \tag{2.35}$$

$$u_{\tau_{eff}} = \sqrt{u_{\tau 1}^2 + u_{\tau 3}^2} \quad . \tag{2.36}$$

Bulk mean velocities in the streamwise direction (u_{b1}), in the spanwise direction (u_{b3}) ant the effective bulk mean velocity (u_{beff}) are defined as follows:

$$u_{bi} = \frac{1}{2} \int_{-1}^{+1} \bar{u}_i(x_2) dx_2 \quad \text{and} \quad i = 1,3 \quad , \tag{2.37}$$

$$u_{b_{eff}} = \sqrt{u_{b1}^2 + u_{b3}^2} \quad . \tag{2.38}$$

Note that the friction velocities and the bulk mean velocities are also non-dimensionalized by u_{τ_0} .
One quantity, which is an essential feature of turbulent flows is vorticity. Vorticity is the curl of velocity field

$$\omega = \nabla \times u. \tag{2.39}$$

The Rossby number (Ro), a ratio of the convective term to the Coriolis force, provides an overall estimate of the importance of non-linear term of the Navier-Stokes equations in a rotating reference frame, is defined as below:

$$Ro = \frac{2u_{b_{eff}}}{Ro_2} \quad . \tag{2.40}$$

Ekman number (E) is also an important dimensionless parameter to analyze the rotating flows, which is a approximate measure of how the typical viscous force compares to the Coriolis force. It is defined as follows:

$$E = \frac{2}{Ro_2 Re_{\tau_0}} \quad . \tag{2.41}$$

No slip boundary condition and impermeability are used on the walls and the peri-

odic boundary conditions are employed in the streamwise (x_1) and the spanwise (x_3) directions.
Homogeneity condition has been also considered in the x_1 and in the x_3 directions, i.e all statistics depend only on x_2 .

3 Laminar Channel Flow with Wall-normal Rotation

3.1 Governing Equations

The Navier-Stokes equations (2.2) in the case of a steady, incompressible laminar wall-normal rotating channel flow can be reduced to the following form:

$$1 + \frac{\partial^2 \tilde{u}_1}{\partial x_2 \partial x_2} - 2\tilde{u}_3 T^2 = 0 \quad , \tag{3.1}$$

$$\frac{\partial^2 \tilde{u}_3}{\partial x_2 \partial x_2} + 2\tilde{u}_1 T^2 = 0 \quad , \tag{3.2}$$

where in order to get a one parameter solution depending only on T, the following non-dimensional notations for velocity and rotation rate have been introduced:

$$\tilde{u}_i \equiv \frac{u_i}{Re_{\tau_0}} \quad \text{and} \quad i = 1, 3 \quad , \qquad T^2 \equiv \frac{\Omega_2 h^2}{\nu} = \frac{Ro_2 Re_{\tau_0}}{2},$$

where T^2 is half of the root of the classical Taylor number and henceforth will be termed as rotation-Reynolds parameter. Note that u_i is already in non-dimensionalized by u_{τ_0}, according to the definition in the last chapter.

3.2 Analytical Solution

The system i.e. (3.1), (3.2), extended by the boundary condition (mentioned in the last chapter) has an analytical solution (obtained also by Wollkind & Diprima (1973)) in the following form:

$$\tilde{u}_1(x_2) = \frac{1}{T^2(cos(2T) + cosh(2T))}[sin(T)sinh(T)cos(Tx_2)cosh(Tx_2) - \\ cos(T)cosh(T)sin(Tx_2)sinh(Tx_2)] \quad , \tag{3.3}$$

$$\tilde{u}_3(x_2) = \frac{-1}{T^2(cos(2T) + cosh(2T))}[cos(T)cosh(T)cos(Tx_2)cosh(Tx_2) + \\ sin(T)sinh(T)sin(Tx_2)sinh(Tx_2)] + 1/2T^2 \quad . \tag{3.4}$$

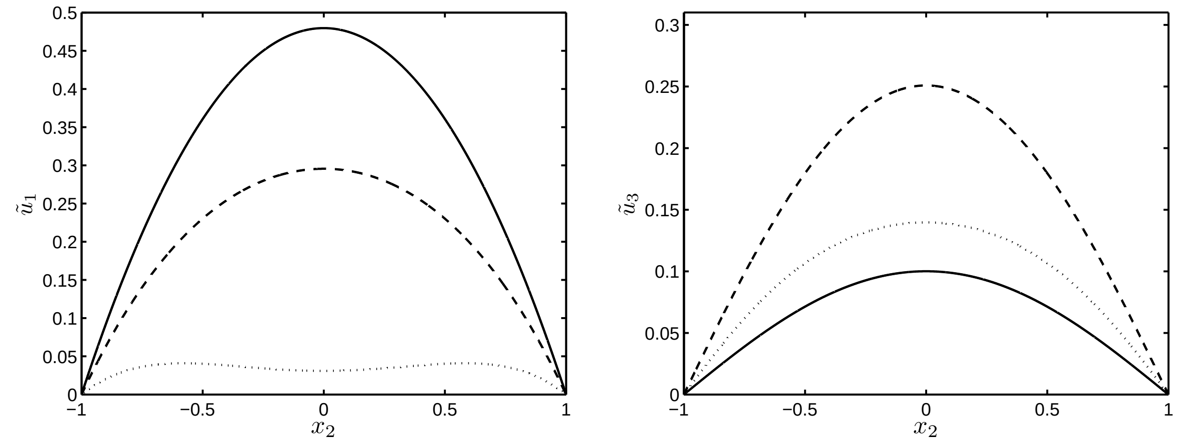

Figure 3.1: Velocity profile in the streamwise and the spanwise directions for different rotation-Reynolds parameter T : $T = 0.5$ —— ; $T = 1$ – – – ; $T = 2$ · · · .

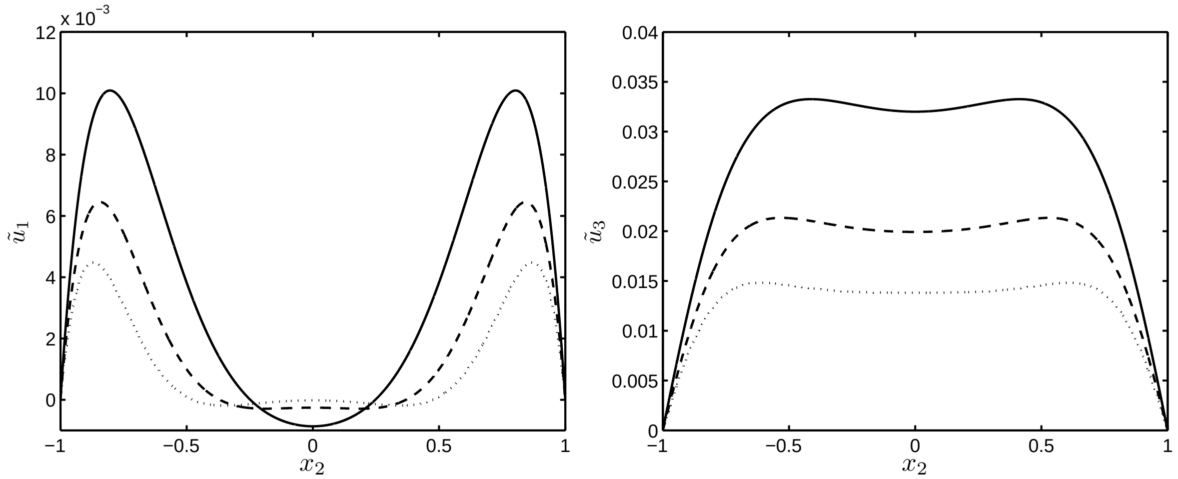

Figure 3.2: Velocity profile in the streamwise and the spanwise directions for different rotation-Reynolds parameter T : $T = 4$ —— ; $T = 5$ – – – ; $T = 6$ · · · .

Existence of the spanwise velocity leads to the development of an Ekman-like spiral flow field, which means that the flow direction rotates, as one moves away from the wall to the channel's center line. In figures 3.1 and 3.2 the velocity profiles for $\tilde{u}_1(x_2)$ and $\tilde{u}_3(x_2)$ at different rotation rates are presented. The strong coupling of the streamwise and the cross-flow induced by the Coriolis force leads to a decrease in the streamwise velocity and an increase in the spanwise velocity up to a maximum around $T = 1$ due to the increase in the rotation rate. Further increasing the rotation rate leads to a reduction of velocities in both directions and also to development of a region around the channel's center line, in which increased Coriolis force overcomes the pressure gradient and a result is the appearance of inflection points in the velocity profiles. This region is extended towards the wall due to the further increasing the rotation rate. Therefore the location of the inflection points is also a function of the rotation rate, i.e.the higher the rotation rate, the closer the inflection points to the wall. This can be seen in figure 3.2. The same region exists in the laminar Ekman layer (discovered by (Ekman 1905)) and also investigated by Greenspan (Greenspan 1980). From the analytical solution it has been obtained that at $T = \pi$ the streamwise velocity at the channel's center line becomes zero and as a result a tapering oscillation about zero has been observed by further increasing the rotation rate. Finally at very high rotation rates ($T \rightarrow \infty$) the oscillation will disappear completely. The tapering behavior is shown in figure 3.3. The same behavior has been observed in the other regions of the channel. The streamwise velocity at every point starts to oscillate at a certain rotation rate, which depends on its location in the channel. The closer the point to the wall, the higher rotation rate that is needed to start the oscillation. In contrast to the streamwise velocity, the spanwise velocity decreases slower and tends asymptotically to zero without any oscillation due to the increase in the rotation rate. The behavior of the spanwise direction velocity in the middle of the channel is also shown in figure 3.4. Based on the behavior of the velocities in the streamwise and the spanwise directions, it can be established that at $T = \pi$ the direction of the flow with respect to the streamwise direction (γ), reaches exactly 90° and then it oscillates about 90° at higher rotation rates. The same is the case for other regions of the channel due to the increase in the rotation rate. For high rotation rates, where $Ro \ll 1$, the analytical solutions for the velocities show similar behaviors compared to the analytical solution of the laminar Ekman-layer.

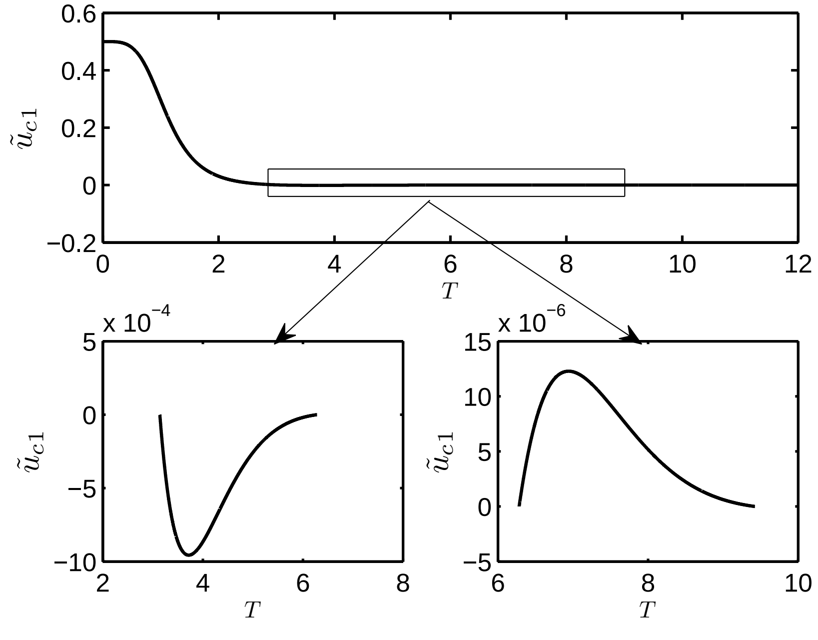

Figure 3.3: Behavior of the streamwise velocity in the middle of the channel as a function of rotation-Reynolds parameter (T).

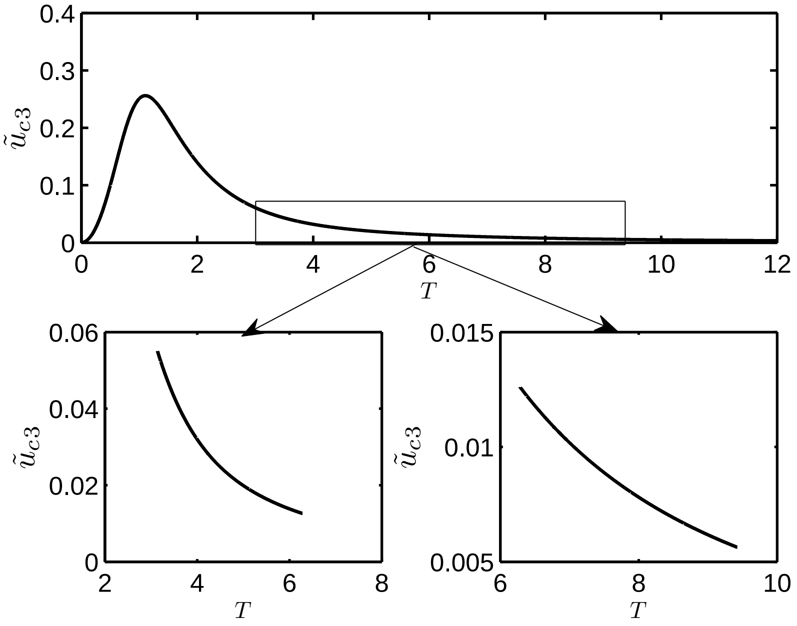

Figure 3.4: Behavior of the spanwise velocity in the middle of the channel as a function of rotation-Reynolds parameter (T).

Bulk mean velocities in the streamwise and the spanwise directions can easily be obtained in the following form:

$$\tilde{u}_{b1} = \frac{-(4e^{2T}sin(T)cos(T) - e^{4T} + 1)}{4T^3(-2e^{2T} + 4e^{2T}(cos(T))^2 + e^{4T} + 1)} \quad , \tag{3.5}$$

$$\tilde{u}_{b3} = \frac{(2T + 1 - e^{4T} - 4e^{2T}sin(T)cos(T) - 4Te^{2T} + 2Te^{4T} + 8Te^{2T}(cos(T))^2)}{4T^3(-2e^{2T} + 4e^{2T}(cos(T))^2 + e^{4T} + 1)} \quad . \tag{3.6}$$

The global behavior of the velocities can be nicely illustrated by plotting the height averaged bulk velocity in each direction for various rotation rates. In figure 3.5 the bulk mean velocity in the streamwise $\tilde{u}_{b1}$ and the spanwise direction $\tilde{u}_{b3}$ and their ratio $\frac{\tilde{u}_{b3}}{\tilde{u}_{b1}}$ are plotted. The bulk mean velocity in the streamwise direction $\tilde{u}_{b1}$ decreases according to $(Ro_2 Re_{\tau_0})^{-3/2}$ from the maximum to nearly zero as the rotation rate goes to infinity. While the in the spanwise direction $\tilde{u}_{b3}$ initially increases and reaches its maximum, it then decreases to almost zero according to $(Ro_2 Re_{\tau_0})^{-1}$ as the rotation rate tends to infinity. It can also be observed that, as the ratio increases, the bulk mean velocity in the streamwise direction decreases much faster than in the spanwise direction. The situation in which the pressure gradient is not sufficient to drive the flow through the channel has been termed as blockage effect. The direction of the average movement of the flow (u_{beff}) with respect to the streamwise direction, which is denoted by β tends to $90°$ as the rotation rate is increased (figure 3.6).

Friction velocities in the streamwise and the spanwise directions can also be derived as follows:

$$u_{\tau_1} = \sqrt{\frac{(4e^{2T}cos(T)sin(T) + e^{4T} - 1)}{(2T(e^{4T} - 2e^{2T} + 4(cos(T))^2e^{2T} + 1))}} \quad , \tag{3.7}$$

$$u_{\tau_3} = \sqrt{\frac{-4e^{2T}cos(T)sin(T) + e^{4T} - 1}{(2T(e^{4T} - 2e^{2T} + 4(cos(T))^2e^{2T} + 1))}} \quad . \tag{3.8}$$

The behavior of the friction velocities in the streamwise and the spanwise directions, their ratio and the effective friction velocity has been indicated in figure 3.7. The same tendency can be observed for the friction velocities in the spanwise and the streamwise directions compared to the bulk mean velocities. However, the friction velocities in both directions approach almost the same value from a certain rotation rate (their ratio is very close to one). It implies that the angle of the effective friction velocity (α) is also very close to $45°$ with respect to the streamwise direction. However, the angle oscillates about $45°$ (figure 3.8) and the oscillation are damped very fast due to the increase in the rotation rate and finally the angle reaches like the Ekman layer $45°$ as the rotation rate tends to infinity and $Ro \rightarrow 0$ as a consequence.

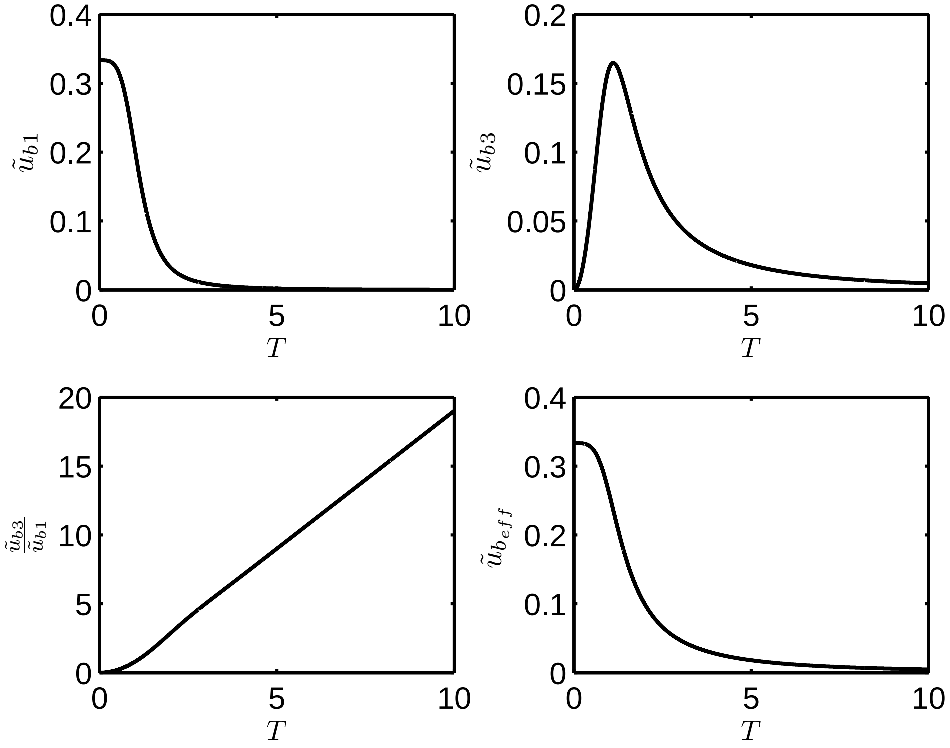

Figure 3.5: Bulk mean velocity in the streamwise and the spanwise directions, their ratio and effective bulk mean velocity as a function of rotation-Reynolds parameter (T).

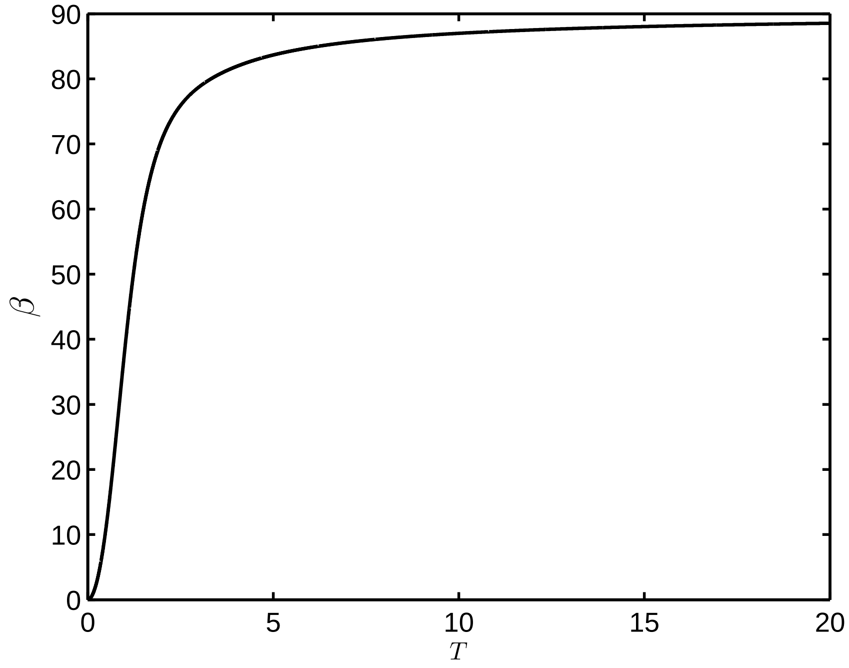

Figure 3.6: Direction of the u_{beff} with respect to the streamwise direction as a function of rotation-Reynolds parameter (T).

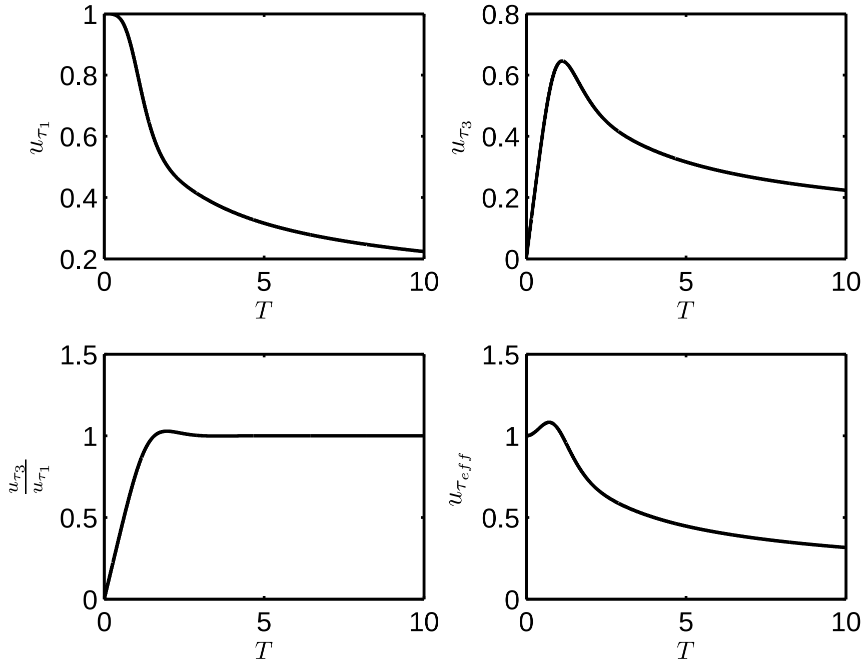

Figure 3.7: Friction velocity in the streamwise and the spanwise directions, their ratio and effective friction velocity as a function of rotation-Reynolds parameter (T).

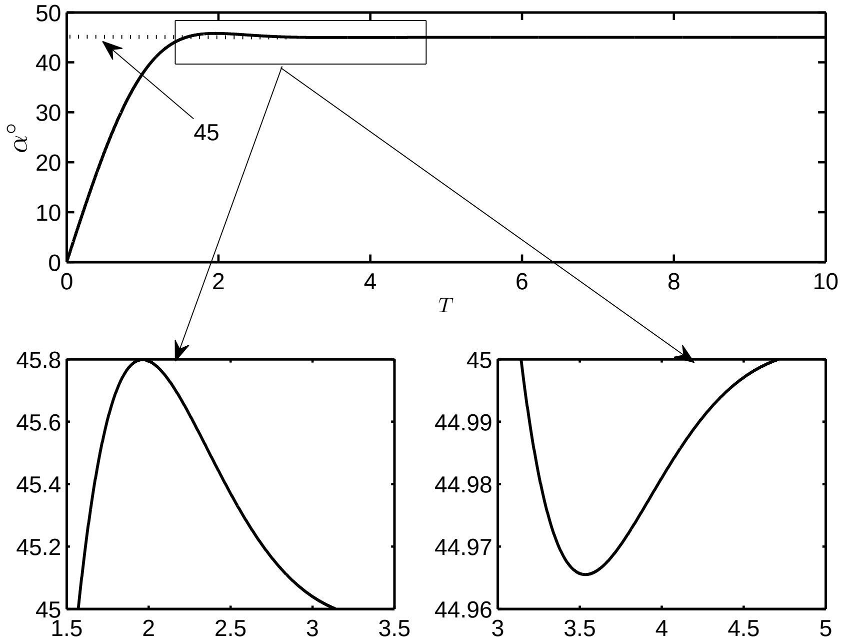

Figure 3.8: Angle of the effective friction velocity with respect to the streamwise direction as a function of rotation-Reynolds parameter (T).

3.3 Summary and Conclusion

In this chapter a laminar channel flow with wall-normal rotation has been investigated. Since the Navier-Stokes equations have an analytical solution for this case, it was possible to study the flow exactly. Based on the obtained results, it has been established that the flow is very sensitive to the wall-normal rotation and is highly affected even by a very small rotation rate. It has also been found that at high rotation rates where the Rossby number takes very small values ($Ro \rightarrow 0$), the present flow has certain commonalities with the laminar Ekman layer. It should also be noted that the analytical solution for the Ekman layer has been obtained from the linear theory for the motion of a viscous incompressible fluid, see (Greenspan 1980). The linear theory concerns motions which represent slight deviations from an established state of rigid rotation. It means the velocity magnitude characteristic of the motion is then small compared to the basic rotation rates and $Ro \ll 1$. Non-linear terms in the Navier-Stokes equations are negligible as a consequence.

4 Direct Numerical Simulation

4.1 Introduction

Orszag & Patterson Jr. (1972) have opened a new horizon in theory of turbulence by indicating the possibility of performing computer simulations of a fully developed turbulent flow. It is important to understand that these simulations do not require any turbulence model to parameterize the influence of the turbulent eddies, since every eddy, from the largest to the smallest, is computed. Started from specified initial conditions the Navier-Stokes equations are integrated forward in some specific domain. It is like carrying out an experiment, only on the computer rather than in a real channel. Indeed, such simulations are called numerical experiments. The potential benefits were immediately clear. Initial conditions can be controlled in such simulations in a way which is just not possible in the laboratory. Moreover, the amount of data which can be recovered is overwhelming: in effect, the entire history of the velocity field is available for inspection. The possibilities seem endless and many fluid dynamicists are attracted to the growing field of direct numerical simulation (DNS). DNS, which are excepted to resolve numerically all eddy sizes, require therefore that the numerical grid resolves the smallest, dissipative eddies so that the average size of grid cell Δ must be smaller than Kolmogorov length scale,i.e $\Delta < \eta$. The large scale eddies are usually of the size comparable with the characteristic flow dimension L and the turbulent velocity fluctuations $k^{\frac{1}{2}}$ is of the same or similar order of magnitude as characteristic mean flow velocity $\bar{u}$. Thus, the mean flow Reynolds number is proportional to the turbulence Reynolds number i.e. $Re \propto Re_t$. Hence , for a three-dimensional turbulent flow, the minimum number of grid points is :

$$N_g \propto \left(\frac{L}{\eta}\right)^3 \propto Re^{\frac{9}{4}}.$$

The number of numerical operations required to reach a statistically convergent solutions increases also with the mean flow Reynolds number. Assuming a conservative estimate that for each grid cell we need $Re^{\frac{1}{2}}$ operations according to different time scales, the total number of numerical operations required is :

$$N_{op} \propto Re^{\frac{11}{4}}.$$

The DNS is therefore limited by computer resources at present to flows with relatively small Reynolds numbers and simple geometries. As mentioned the first attempt of a DNS was made by Orszag & Patterson Jr. (1972) in 1972 for homogeneous turbulence. Considerably later the DNS for a fully developed turbulent channel flow was performed by Kim, Moin & Moser (1987). In this paper the first DNS of a non-rotating turbulent channel flow was presented at a Reynolds number of $Re_{\tau_0} = 180$. Later, more elaborate DNS of a turbulent channel flow were conducted e.g. by Kuroda, Kasagi & Hirata (1989), Kasagi, Tomita & Kuroda (1992) and Moser, Kim & Mansour (1999) primarily to increase the Reynolds number ($Re_{\tau_0} = 640$). Recently the DNS of turbulent channel flow for higher Reynolds numbers was done by Abe, Kawamura & Matsuo (2001). Computations at higher Reynolds numbers were also under investigation in the group of Jiménez in Madrid, Spain. Studies were carried out to Reynolds numbers up to $Re_{\tau_0} = 2003$ (see Hoyas & Jiménez (2006)).

4.2 Numerical Method

There are many different methods to solve partial differential equations numerically, such as finite elements, finite difference and spectral methods. A spectral method has been used in the present work for the numerical simulation of turbulent rotating channel flow. Spectral methods are based on the idea that the solution$s(x)$ is expanded in a sum of basis functions,

$$s(x) \approx \sum_{n=0}^{N} a_n \psi_n(x).$$

This series is substituted into the equation

$$Bs = f(x),$$

where B is an operator describing the differential equation. A residual is defined as:

$$R(x, d_0, a_1, ..., a_n) = Bs_N - f.$$

The goal is to minimize the residual function by choosing suitable base function ψ_n and expansion coefficients a_n. One great advantage of spectral methods compared to the finite element and finite volume methods is their minimal phase error. From the error analysis for the spectral methods one can deduce that for an infinitely differentiable function, the approximation error is smaller than any power of $\frac{1}{N}$: the convergence is exponential. This behavior is commonly called spectral or infinite accuracy (for more information see (Peyret 2002)).

The Numerical code, which has been used for the present work, is based on a standard spectral method with Fourier decomposition in the streamwise and spanwise directions as well as Chebyshev decomposition in the wall-normal direction. Time integration is performed using a third order Runge-Kutta scheme for the advective and Crank-Nicolson for the viscous terms. The transformation between physical and spectral space is done by Fast Fourier Transforn (FFT). The original version of the code for non-rotating coordinate systems was developed at KTH in Stockholm (Lundbladh, Henningson & Johanson 1992). Additional features such as the streamwise rotation and statistics were added.

The code is parallelized by OpenMP. The OpenMP application programming interface (API) supports multi-platform shared memory multiprocessing programming. All calculations were conducted at the Hessian High Performance Computer (HHLR) at Technische Universität Darmstadt. The supercomputer is Shared Memory Computer (SMC), which is particularly well suitable for parallel computations with many of interprocess communication.

4.3 Computations at $\mathrm{Re}_{\tau_0} = 180$

In this section we present the results of DNS at $Re_{\tau_0} = 180$ and Ro_2 between $0 - 1.82$. In this range the flow exhibits a variety of features ranging from fully turbulent at small rotation rates, to strictly laminar at high rotation rates, crossing through a quasi-laminar state (in which smooth circulations exist and the Reynolds number is below the corresponding critical Reynolds number) with distinctly elongated structures.
Streamwise and spanwise two-point correlations of the velocity fluctuations i.e. R_{ii} have been calculated in the middle of the channel to ensure that the computational domain is large enough for the fully turbulent case,

$$R_{ii} = \overline{u_i'(x) u_i'(x+r)} \quad . \tag{4.1}$$

The two-point correlation for u_1' in the streamwise direction (R_{11x}), u_3' in both directions (R_{33x} and R_{33z}) and u_2' in the spanwise direction (R_{22z}) for different rotation rates have been illustrated in figures 4.1 and 4.2, confirming that the computational domain is large enough in the spanwise and the streamwise directions.

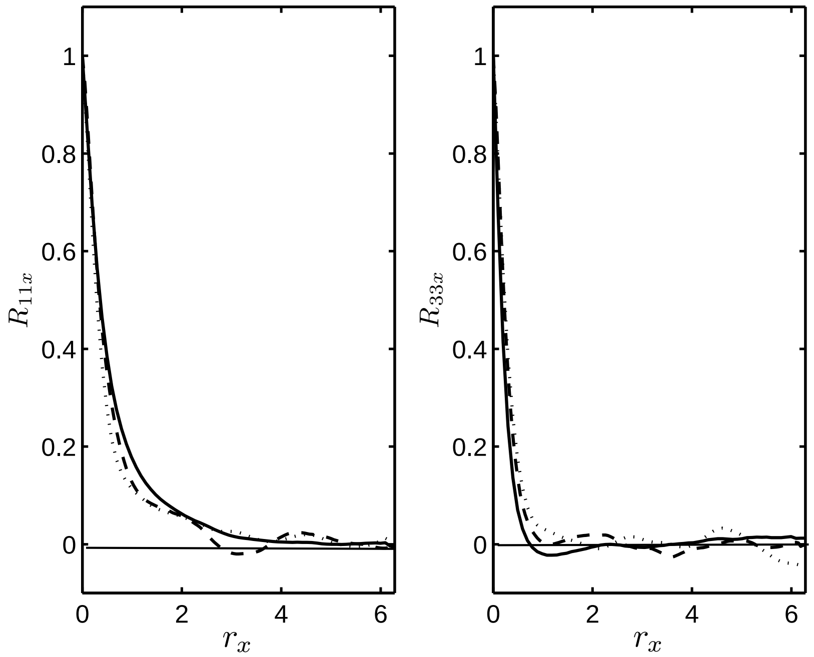

Figure 4.1: Two point correlation in the streamwise direction in the mid-plane ($x_2 = 0$) for two different rotation numbers : $Ro_2 = 0.018$ —— ; $Ro_2 = 0.054$ - - - ; $Ro_2 = 0.091$ ··· .

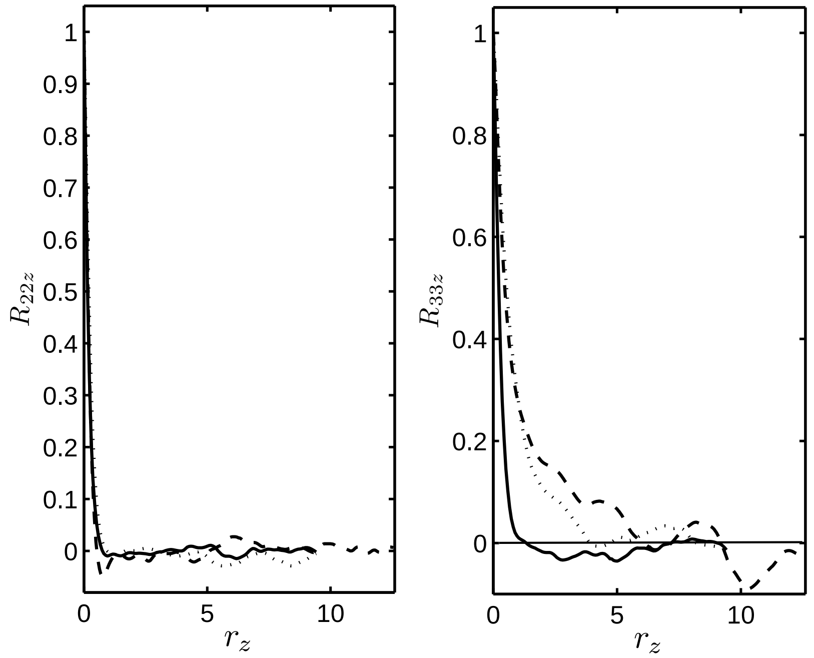

Figure 4.2: Two point correlation in the spanwise direction in the mid-plane ($x_2 = 0$) for two different rotation numbers : $Ro_2 = 0.018$ —— ; $Ro_2 = 0.054$ - - - ; $Ro_2 = 0.091$ ··· .

The performed simulations have been summarized in the following table.

Table 4.1: Performed DNS at $Re_{\tau_0} = 180$.

Ro_2	Computational Domain	Grid	Flow State
0	$4\pi \times 2 \times 2\pi$	$128 \times 129 \times 128$	Turbulent
0.018	$4\pi \times 2 \times 6\pi$	$128 \times 129 \times 384$	Turbulent
0.054	$4\pi \times 2 \times 8\pi$	$128 \times 129 \times 512$	Turbulent
0.091	$4\pi \times 2 \times 6\pi$	$128 \times 129 \times 384$	Turbulent
0.145	$4\pi \times 2 \times 2\pi$	$128 \times 129 \times 128$	Quasi-laminar
0.182	$4\pi \times 2 \times 2\pi$	$128 \times 129 \times 128$	Quasi-laminar
0.273	$4\pi \times 2 \times 2\pi$	$128 \times 129 \times 128$	Quasi-laminar
0.546	$4\pi \times 2 \times 2\pi$	$128 \times 129 \times 128$	Laminar
0.728	$4\pi \times 2 \times 2\pi$	$128 \times 129 \times 128$	Laminar
1.82	$4\pi \times 2 \times 2\pi$	$128 \times 129 \times 128$	Laminar

The uniform grid resolution in the streamwise and the spanwise directions used for all simulation is given as follows:

$$\Delta x_1^+ \approx 17.67 \quad \Delta x_3^+ \approx 8.84.$$

The resolution in the wall-normal (x_2) direction is fine near the walls and becomes coarser away from the wall due to the Chebyshev collocation point. The variation from the finest to the coarsest cells in this direction is as below:

$$\Delta x_2^+ \approx 0.054 - 4.417,$$

where Δx_i^+ is defined as follows:

$$\Delta x_i^+ = \frac{\Delta x_i u_{\tau_0}}{\nu}.$$

In order to examine the behavior of the flow in the fully turbulent region a variety of key parameters have been defined. They will be used subsequently to qualify and quantify the flow. The logarithmic law of the wall in the streamwise and the spanwise directions can be studied by defining Γ_i in both directions as follows:

$$\Gamma_i = x_2 \frac{\partial \bar{u}_i}{\partial x_2} \qquad \text{and} \quad i = 1, 3 \quad . \tag{4.2}$$

In order to investigate the effects of the wall-normal rotation on the Reynolds stress field and its deviation from the isotropic turbulence field, the flatness factor A is defined subsequently. For this, we need the Reynolds stress anisotropy tensor:

$$b_{ij} = \frac{\overline{u_i^{\prime} u_j^{\prime}}}{2k} - \frac{1}{3}\delta_{ij} \quad , \tag{4.3}$$

where $\overline{u'_i u'_j}$ are the Reynolds stresses and k is the turbulent kinetic energy. Second and third invariants of the anisotropy tensor i.e. II and III are defined as below:

$$II = -\frac{b_{ij}b_{ij}}{2} \quad , \tag{4.4}$$

$$III = \frac{b_{ij}b_{jk}b_{ki}}{3} \quad . \tag{4.5}$$

From this the flatness factor is defined in the following form:

$$A = 1 - \frac{9}{8}(-8II - 24III) \quad . \tag{4.6}$$

Note that $A = 1$ represents the isotropic stress field. The final parameter is the structure parameter (a_1), which is used to determine the degree of three-dimensionality of the flow. a_1 is defined as the ratio of the magnitude of the Reynolds stress to the trace of the Reynolds stress tensor i.e, twice of the turbulent kinetic energy.

$$a_1 = \frac{(\overline{u'_1 u'_2}^2 + \overline{u'_2 u'_3}^2)^{\frac{1}{2}}}{2k}. \tag{4.7}$$

4.3.1 Fully Turbulent Region

Four simulations for $Ro_2 = 0, 0.018, 0.054$ and 0.091 have been qualified as fully turbulent. The results obtained for the statistical quantities will be presented in the following.

4.3.1.1 Mean Velocities

The effects of the wall-normal rotation on the mean velocities can be well understood by investigation of the mean flow equations, the averaged Navier-Stokes equations. The mean flow equations in the streamwise and the spanwise directions are as below:

$$0 = -\frac{1}{\rho}\frac{\partial \bar{p}}{\partial x_1} - \frac{\partial \overline{u'_1 u'_2}}{\partial x_2} + \nu \frac{\partial^2 \bar{u}_1}{\partial x_2^2} - 2\,\Omega_2 \bar{u}_3 \quad , \tag{4.8}$$

$$0 = -\frac{\partial \overline{u'_2 u'_3}}{\partial x_2} + \nu \frac{\partial^2 \bar{u}_3}{\partial x_2^2} + 2\,\Omega_2 \bar{u}_1 \quad . \tag{4.9}$$

The equations indicate that in contrast to the turbulent channel flow rotating about the streamwise or the spanwise axis, in the case of the wall-normal rotation the Coriolis forces enter in the mean flow equations. So it can be concluded that the mean velocities are very sensitive to the wall-normal rotation and the effects of even very weak rotation rates on the mean velocities are visible. In figure 4.3 the mean velocity profiles in the streamwise and the spanwise directions are shown. As the wall-normal rotation is imposed, the streamwise mean velocity decreases with an increase of the rotation rate, indicating a reduction in the wall shear rate related to the streamwise mean flow. The spanwise mean velocity increases, as the rotation rate varies from 0 to 0.054, and then decreases due to the further increase in the rotation rate. As shown the wall-normal rotation strongly affects the mean flow in the streamwise and the spanwise since it enters explicitly in the mean flow equations.

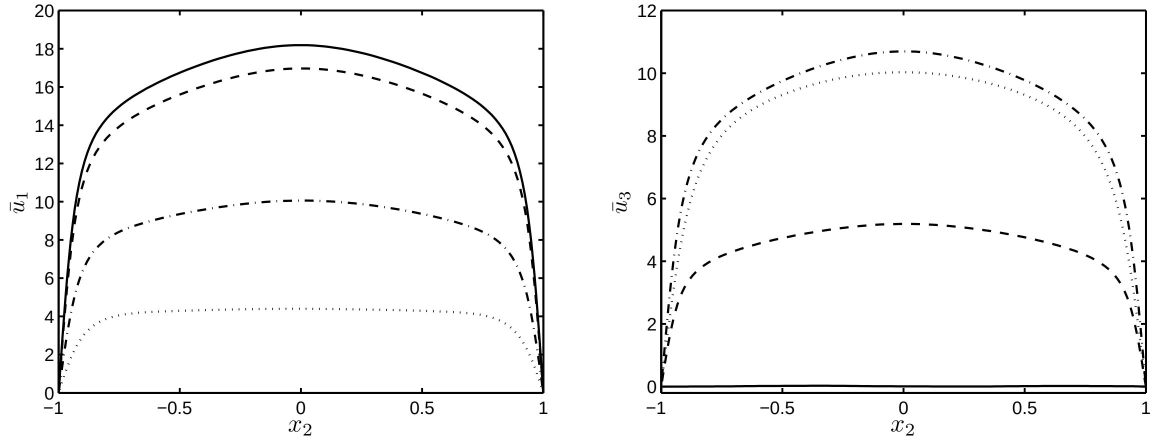

Figure 4.3: Mean velocities in the streamwise ($\bar{u}_1$) and in the spanwise ($\bar{u}_3$) directions at different rotation numbers: $Ro_2 = 0$ —— ; $Ro_2 = 0.018$ - - - ; $Ro_2 = 0.054$ —·— ; $Ro_2 = 0.091$ ··· .

It is also established that up to $Ro_2 = 0.054$, there is a region with a nearly constant log-law indicator function (i.e the logarithmic region exists) in both directions which disappears at higher rotation rates, showing that at the boarder between the fully turbulent and the quasi-laminar states (i.e. $Ro_2 = 0.091$), the logarithmic region is either very thin or non-existent (Figure 4.4).

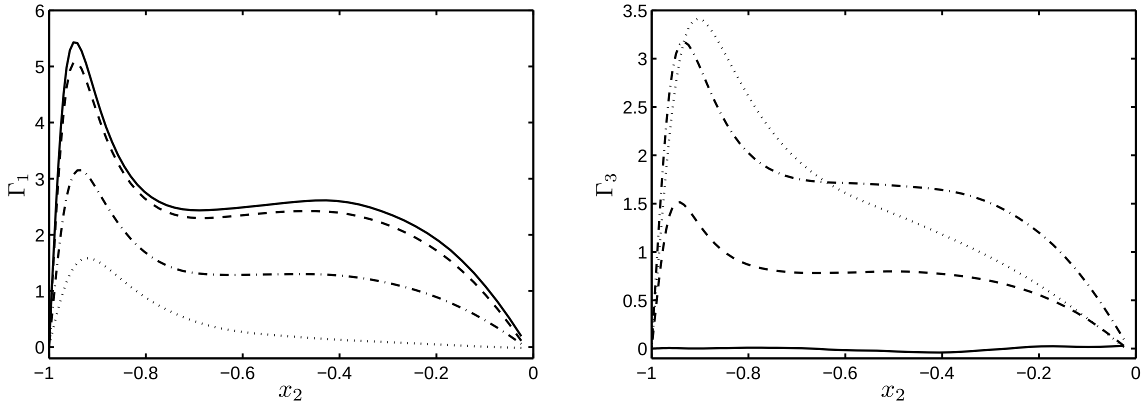

Figure 4.4: Log-law indicator functions (Γ_1 and Γ_3) at different rotation numbers: $Ro_2 = 0$ —— ; $Ro_2 = 0.018$ - - - ; $Ro_2 = 0.054$ —·— ; $Ro_2 = 0.091$ ··· .

4.3.1.2 Reynolds Stresses

Distributions of the turbulence intensities at different rotation rates are indicated in figure 4.5. In the non-rotating channel the streamwise velocity fluctuation is mainly generated by the shear process of the streamwise mean flow, while the mechanism of generating the spanwise velocity fluctuation is only the splattering effect induced by high-speed streaky structures rushing to the wall and low-speed ones lifting from the wall, (Moin & Kim 1982). However, in the wall-normal rotating channel flow the Coriolis force induces the spanwise mean velocity and therefore the shear process of the spanwise mean velocity takes a dominant responsibility to generate the spanwise velocity fluctuation. Therefore the spanwise and the streamwise velocity fluctuations indicate similar behaviors with the spanwise and the streamwise mean velocities when the rotation rate is varied. The wall-normal velocity fluctuation has the same feature compared to the streamwise velocity fluctuation and decreases monotonically as the rotation rate increases. Reynolds normal stresses and the turbulent kinetic energy are plotted in figure 4.6. Due to an increase in the rotation rate the turbulent kinetic energy k decreases, indicating that the increase in the rotation rate damps the turbulent intensity.

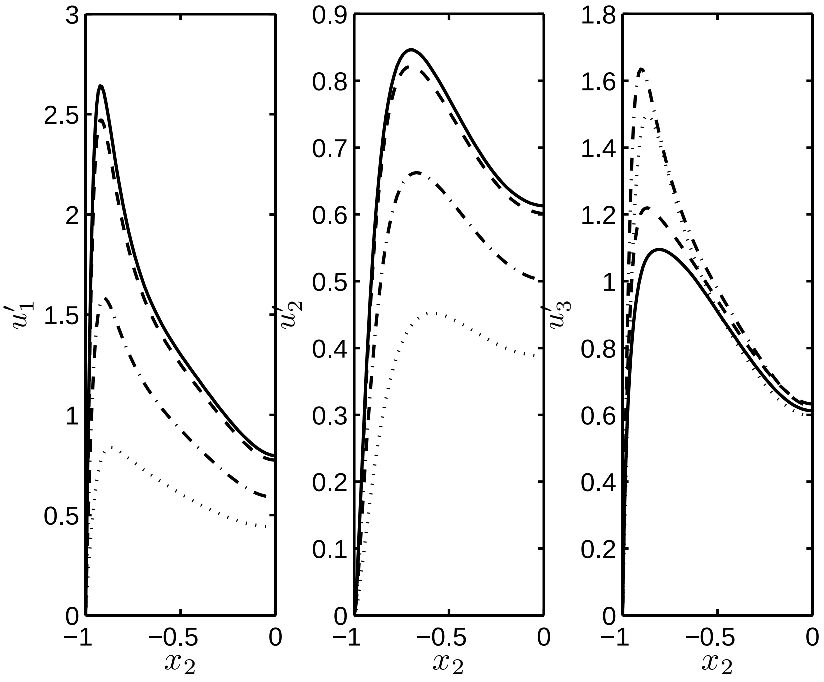

Figure 4.5: r.m.s distributions of the turbulence intensities at different rotation rates: $Ro_2 = 0$ —— ; $Ro_2 = 0.018$ - - - ; $Ro_2 = 0.054$ —·— ; $Ro_2 = 0.091$ ··· .

The shear stresses i.e. $\overline{u_1'u_2'}$ and $\overline{u_2'u_3'}$, are illustrated in figure 4.7. They are generated mainly due to the shear processes of the streamwise and the spanwise mean velocities and therefore show similar behaviors with $(\bar{u}_1)$ and $(\bar{u}_3)$ against the rotation rates.

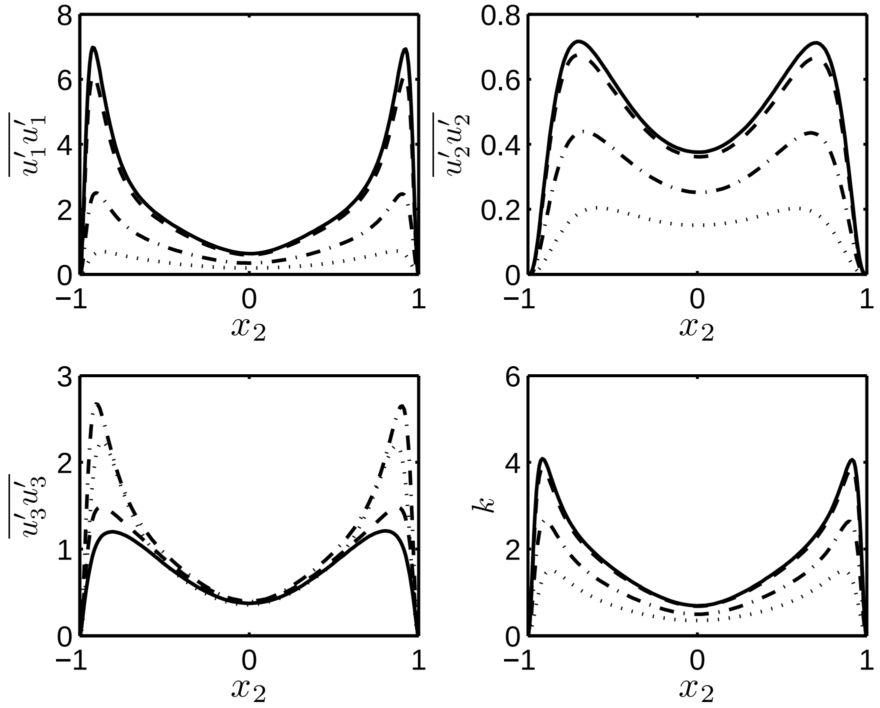

Figure 4.6: Turbulent normal stresses and the turbulent kinetic energy for different rotation rates: $Ro_2 = 0$ —— ; $Ro_2 = 0.018$ - - - ; $Ro_2 = 0.054$ —·— ; $Ro_2 = 0.091 \cdots$.

Existence of linear regions in the shear stresses in the core region of the channel, may imply that in the streamwise direction the Coriolis force and $\overline{u_1'u_2'}$ balance the mean pressure gradient and in the spanwise direction $\overline{u_2'u_3'}$ balances the Coriolis force. Obviously, the slope of the linear regions depends on the rotation rate and actually shows the strength of the Coriolis force. It should here be noted that the rotational productional term of $\overline{u_i'u_j'}$ i.e. $2\Omega_2(e_{2li}\overline{u_j'u_l'} + e_{2lj}\overline{u_i'u_l'})$ is negligible due to the weak imposed rotation rates. This can be understood by investigating of the transport equation for $\overline{u_i'u_j'}$:

$$\begin{aligned} 0 = &-\overline{u_i'u_2'}\frac{\partial \bar{u}_j}{\partial x_2} - \overline{u_j'u_2'}\frac{\partial \bar{u}_i}{\partial x_2} - 2\nu\overline{\frac{\partial u_i'}{\partial x_2}\frac{\partial u_j'}{\partial x_2}} + \overline{\frac{p'}{\rho}\Big(\frac{\partial u_i'}{\partial x_j} + \frac{\partial u_j'}{\partial x_i}\Big)} \\ &+\frac{\partial}{\partial x_2}\Big[-\overline{u_i'u_j'u_2'} + \nu\frac{\partial \overline{u_i'u_j'}}{\partial x_2} - \overline{\frac{p'}{p}(\delta_{2j}u_i' + \delta_{2i}u_j')}\Big] - 2\Omega_2(e_{2li}\overline{u_j'u_l'} + e_{2lj}\overline{u_i'u_l'}). \end{aligned} \tag{4.10}$$

Existence of $\overline{u_1'u_3'}$ indicates that in contrast to the non-rotating case in the present flow there is correlation between velocity fluctuations in the spanwise and the streamwise direction. Shear processes in the streamwise and the spanwise mean velocity contribute to the production of $\overline{u_1'u_3'}$ according to the analysis of its transport equation $((4-10))$. However, it does not enter the RANS equations due to the Homogeneity in the streamwise and the spanwise directions. $\overline{u_1'u_3'}$ for different rotation rates is shown in figure 4.8.

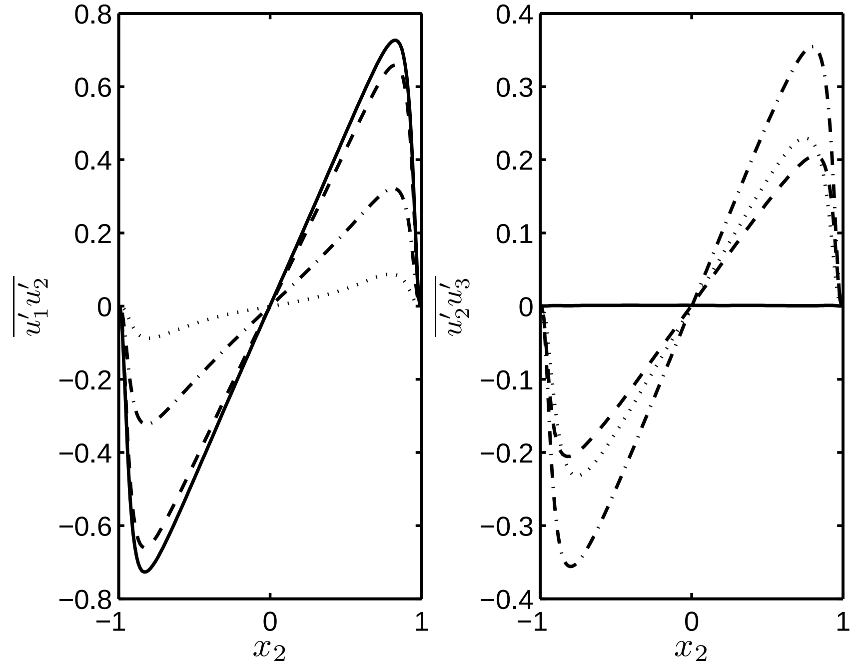

Figure 4.7: Turbulent shear stresses at different rotation rates: $Ro_2 = 0$ —— ; $Ro_2 = 0.018$ - - - ; $Ro_2 = 0.054$ —·— ; $Ro_2 = 0.091 \cdots$.

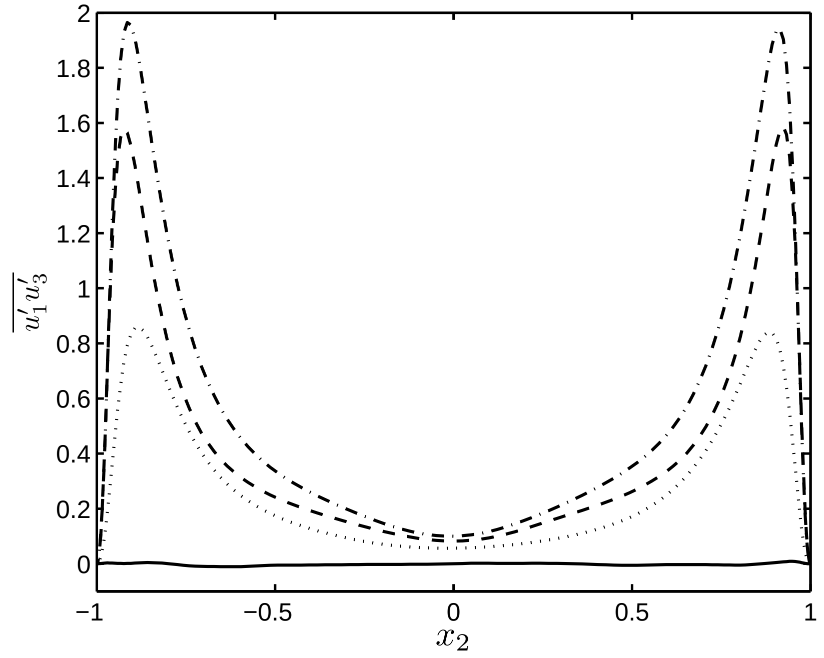

Figure 4.8: Distribution of $\overline{u_1'u_3'}$ at different rotation rates: $Ro_2 = 0$ —— ; $Ro_2 = 0.018$ - - - ; $Ro_2 = 0.054$ —·— ; $Ro_2 = 0.091 \cdots$.

In figure 4.9 the flatness factor A and the structure parameter a_1 for different rotation numbers are shown. Comparing flatness factor and the structure parameter for different rotation rates, indicates a clear deviation from the non-rotating case only when approaching the quasi-laminar region at about $Ro_2 = 0.091$. This indicates that the turbulent wall-normal rotating channel flow could also be regarded as a two-dimensional flow.

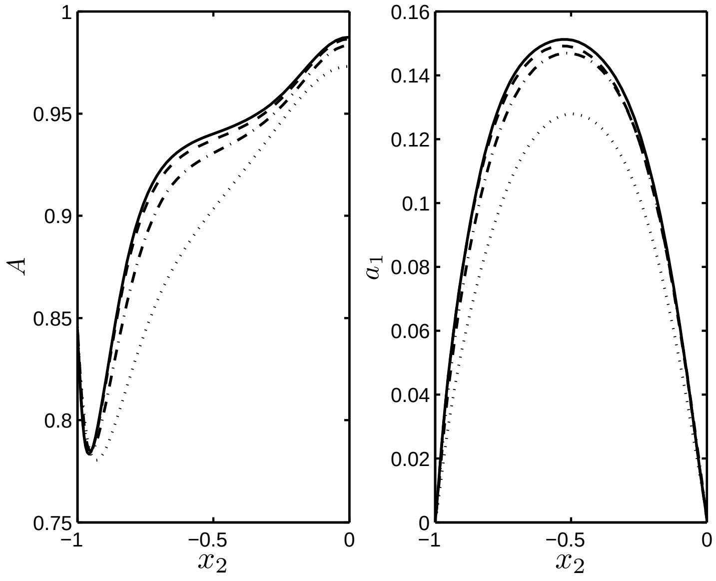

Figure 4.9: The flatness factor (left) and the Structure parameter (right) in the fully turbulent region for different rotation rates: $Ro_2 = 0$ —— ; $Ro_2 = 0.018$ - - - ; $Ro_2 = 0.054$ —·— ; $Ro_2 = 0.091$ · · · .

4.3.1.3 Vorticities

Non-dimensionalized root-mean-square (r.m.s) vorticity fluctuations obtained from the velocity field (not by solving the vorticity equation) for different rotation rates are shown in figure 4.10. As a result of the splatting effect the streamwise vorticity (ω_1^+) and the spanwise vorticity (ω_3^+) attain their maximum at the wall. Existence of local maxima and minima in the streamwise vorticity in the non-rotating case and in the spanwise vorticity at $Ro_2 = 0.091$ have been attributed to the vortices in the wall region, (Kim et al. 1987). It is also interesting to note that, in all cases (rotating and non-rotating cases), in spite of large differences between different components of ω^+ in the wall region, away from the wall they are virtually identical or in the other words they are almost isotrop. This is in contrast to the r.m.s velocity fluctuations (Figure 4.11). The difference between the two may be explained by noting that the relative contribution of small scales to vorticity fluctuations are significantly larger that their contribution to the velocity fluctuations, and away from the wall the small scales tend to be isotropic.

Worth noting here is that the behaviors of the velocity fluctuations and also the vorticity fluctuation are very similar to the observed results for the non-rotating case.

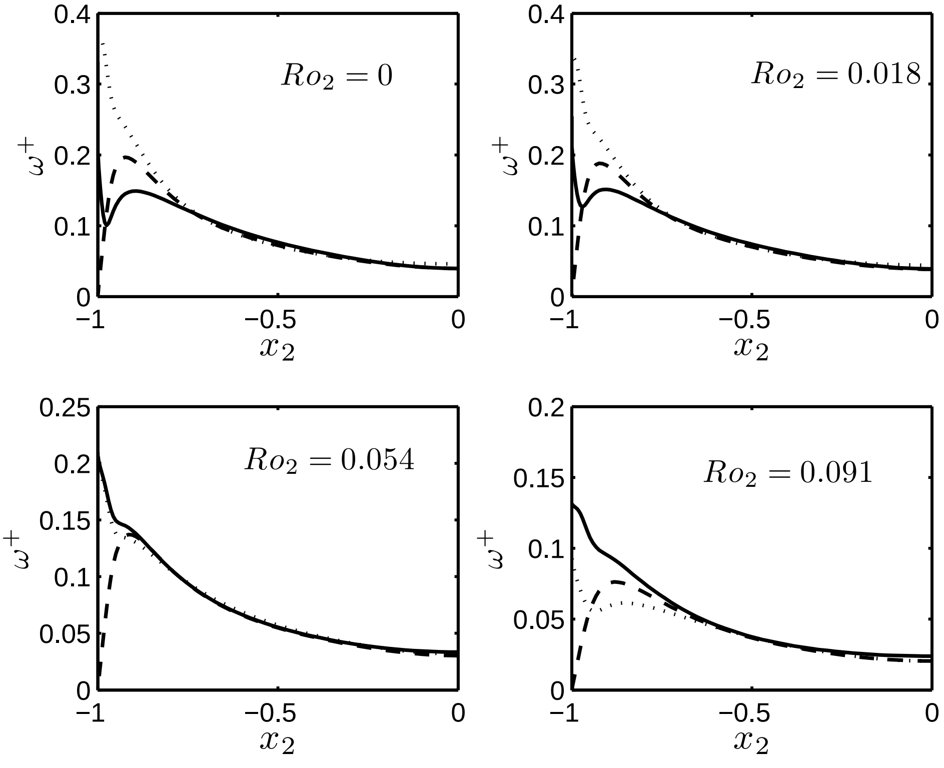

Figure 4.10: Normalized r.m.s vorticity fluctuations for different rotation rates: ω_1^+ —— ; ω_2^+ - - - ; ω_3^+ · · · .

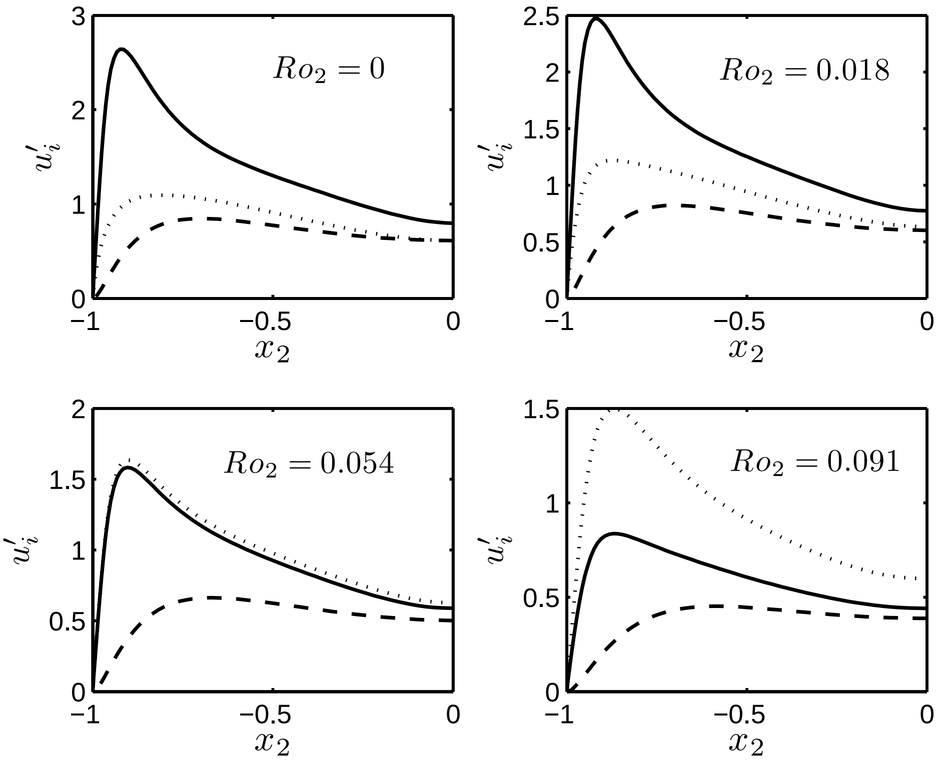

Figure 4.11: Normalized r.m.s velocity fluctuations for different rotation rates: u_1' —— ; u_2' - - - ; u_3' · · · ·.

4.3.2 Quasi-Laminar Region

Relaminarization is an important effect of rotation on turbulent flows and its main result, depending on the key parameter Ro_2, is the transition to the fully laminar state. The simulations for $Ro_2 = 0.145, 0.182$ and 0.273 have been qualified as quasi-laminar state. Based on the results obtained from the DNS, relaminarization starts at about $Ro_2 = 0.145$. Worth noting here is that the Reynolds number at $Ro_2 = 0.145$ is very close to the critical Reynolds number obtained by (Hoffmann & Busse 2001) using linear stability analysis of the flow. At higher rotation rates ($Ro_2 = 0.182, 0.273$) the Reynolds numbers are clearly smaller than the critical ones. Similar to the laminar case the increased Coriolis force is thought to be the reason of the appearance of the inflection points in the velocity profiles. However, the inflection points appear first in the streamwise mean velocity profile at $Ro_2 = 0.145$ and then due to the further increase in the rotation rate they are also visible in the spanwise mean velocity profile. Therefore the log-law indicator functions attain also negative values in this region. The mean velocity profiles and the log-law indicator functions have been illustrated in figure 4.12 and 4.13. Apart from the statistical quantities in this region, large-scale coherent structures (longitudinal or roll-like vortices) have been also observed. It should here be noted that we are treating in this study any kind of coherent structures larger than the small-scale turbulence. Although research on large-scale or coherent structures is quit popular at present in turbulent boundary layers, we shall restrict our investigation to the horizontal roll-like vortices extending throughout the whole channel. The roll vortices are also an observed planetary boundary layer (PBL) phenomenon with important consequence for transport and therefore modeling of the flow Le Mone (1973). However, the physics of their formation is uncertain. There is still a question as to whether the rolls are the result of only the inflectional instability associated with Ekman layer profile or also require the additional influence of buoyantly unstable motion. Deardorff (1972) found that only with an upward heat flux (represented by vertical velocity) eddies become if not rolls at least distinctly elongated. On the other hand, theories concerning PBL rolls based only upon the inflectional mechanism have been proposed by Faller (1965), Brown (1974) and Etling & Brown (1993). These theories have as their foundation the fact that, for certain Reynolds numbers, the Ekman layer contains longitudinal rolls in a quasi-laminar state. The PBL rolls have been suggested to be the atmospheric counterparts of the rolls observed under neutrally-stratified conditions in the laboratory in a quasi-laminar state, Faller (1963) and Caldwell & Van Atta (1970). The results obtained for the present flow strongly support the theories proposed by Faller and Brown. The appearance of the first inflection point in the streamwise mean velocity may be a symptom of the start of the relaminarization process and transition to the quasi-laminar state. In figures 4.14 and 4.15 the coherent structures in the transitional region are illustrated. Figure 4.16 nicely shows that an increase in the rotation rate causes the turbulence to be decreased and finally at about $Ro_2 = 0.546$ fluctuations are completely damped and the flow has reached a fully laminar state.

Figure 4.12: Mean velocities in the streamwise ($\bar{u}_1$) and in the spanwise ($\bar{u}_3$) directions and in the quasi-laminar region for different rotation numbers: $Ro_2 = 0.145$ —— ; $Ro_2 = 0.182$ - - - ; $Ro_2 = 0.273$ –·–· .

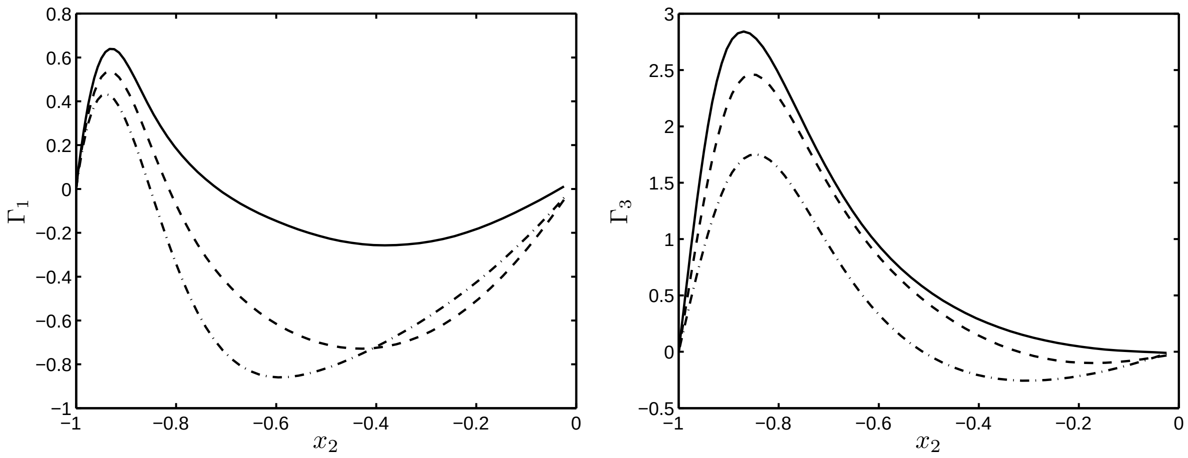

Figure 4.13: Log-law indicator functions (Γ_1 and Γ_3) in the quasi-laminar region at different rotation numbers: $Ro_2 = 0.145$ —— ; $Ro_2 = 0.182$ - - - ; $Ro_2 = 0.273$ —-— .

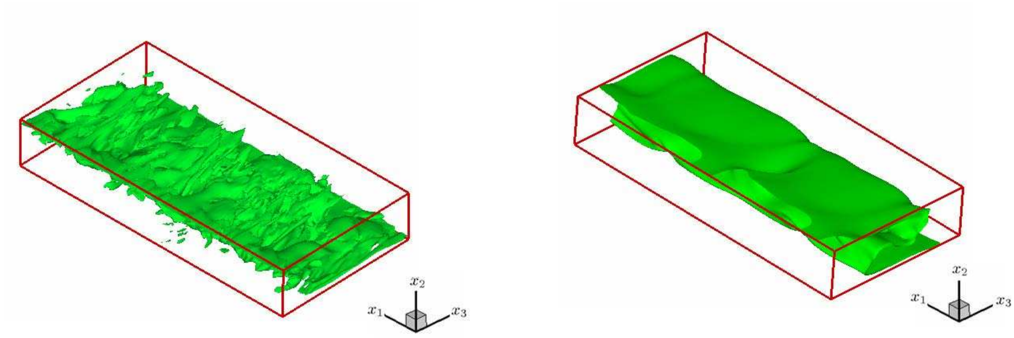

Figure 4.14: Elongated coherent structures in the quasi-laminar region for $Ro = 0.145$ at $\omega_3 = 0.02$ (left) and $Ro = 0.273$ at $\omega_1 = 0.005$ (right).

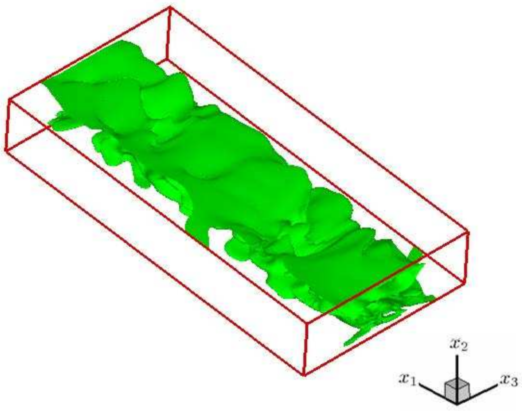

Figure 4.15: Elongated coherent structures in the quasi-laminar region for $Ro = 0.182$ at $\omega_1 = 0.007$.

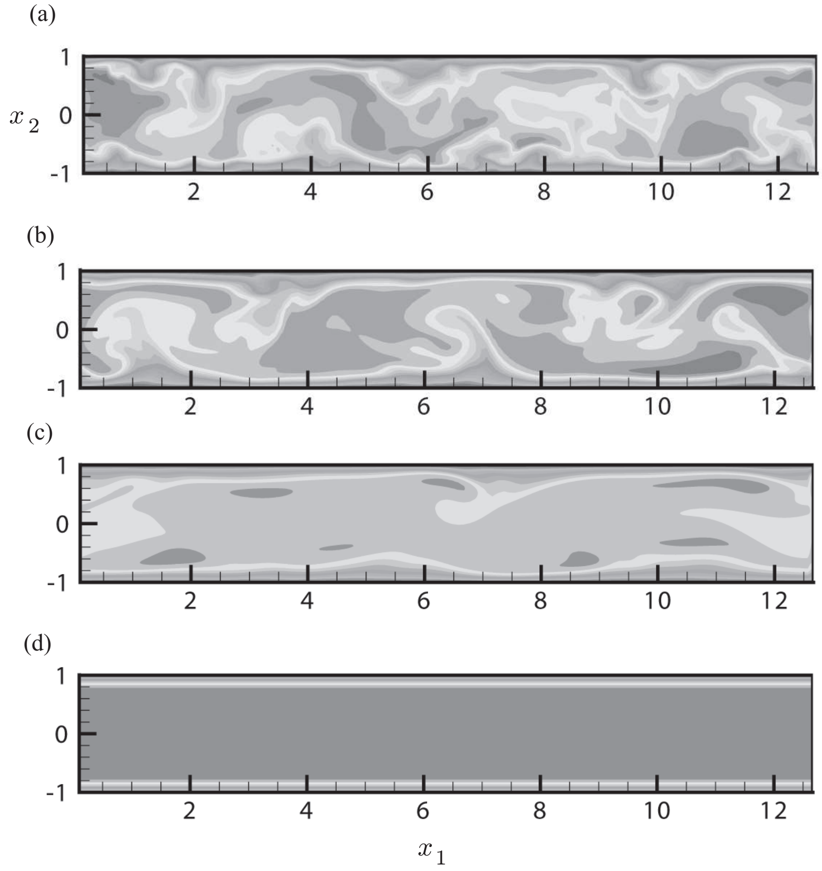

Figure 4.16: U_3 velocity contours in the range $0-10$ in the (x_1, x_2) plane for different rotation rates: $Ro_2 = 0.145$ (a) ; $Ro_2 = 0.182$ (b) ; $Ro_2 = 0.273$ (c) ; $Ro_2 = 0.546$ (d) .

4.3.3 Laminar Region

A result of further increasing the rotation rate ($Ro_2 > 0.273$) is a complete suppression of turbulence and hence a vanishing Reynolds stress tensor. As a result, a steady laminar flow is observed. For the present subsection three simulations at $Ro = 0.546, 0.728$ and 1.82 have been calculated. There is a very good agreement between the results obtained from the DNS and the analytical solution given by the equations (3.3) and (3.4). In all computations for $Ro_2 > 0.273$ the deviation of the DNS results from the analytical solution is less than 1 percent. The variations of Ro_2 and its effect on the bulk mean velocities, the friction velocities, the Rossby number and the Ekman number from the fully turbulent state to the fully laminar steady state are shown in the figures 4.17, 4.18 and 4.19. The solid lines are the analytical solutions for the laminar case. They have been plotted starting $Ro_2 = 0.1$, almost the border between the fully turbulent and the quasi-laminar region. It may also be noted that the bulk and the friction velocities in the quasi-laminar region are closer to the laminar state than to the fully turbulent state. Still rather similar qualitative behaviors for the bulk and the friction velocities have been observed for the fully laminar flow as may be taken from figures 3.6 and 3.8.

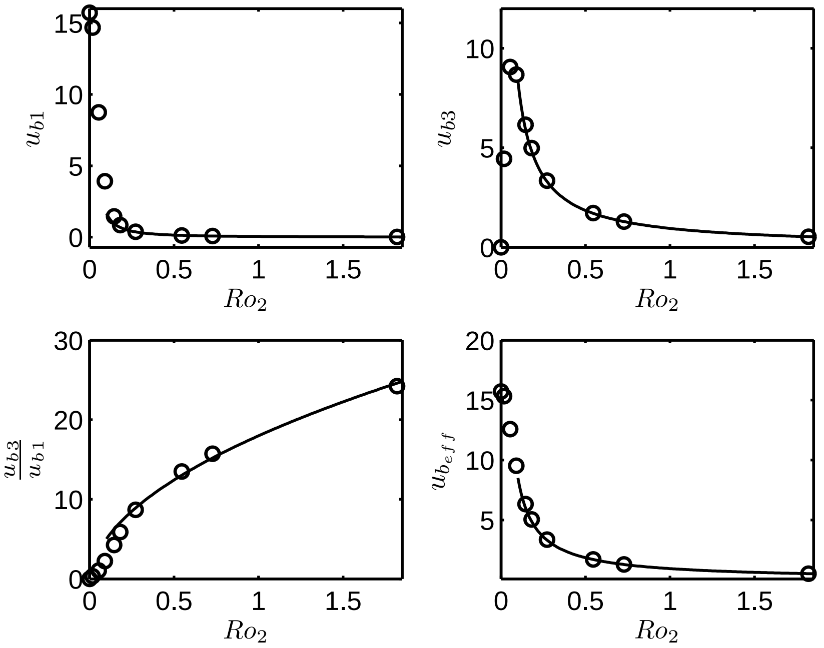

Figure 4.17: Variation of the mean bulk velocities in the streamwise and the spanwise directions, their ratio and the effective friction velocity from the fully turbulent to the laminar steady state, DNS ∘ ; analytical solution for the laminar case —— .

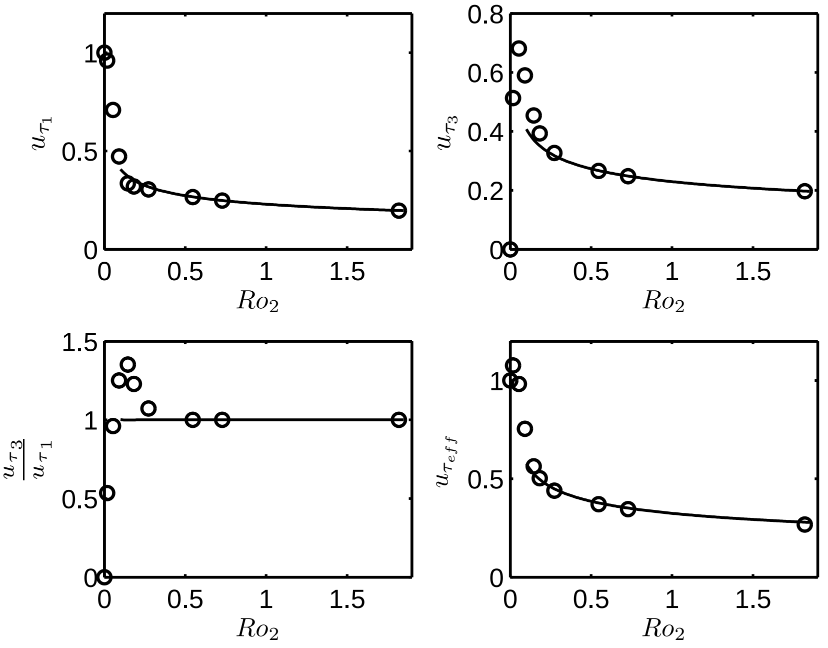

Figure 4.18: Variation of the friction velocities in the streamwise and the spanwise directions, their ratio and the effective friction velocity from the fully turbulent to the laminar steady state, DNS ∘ ; analytical solution for the laminar case —— .

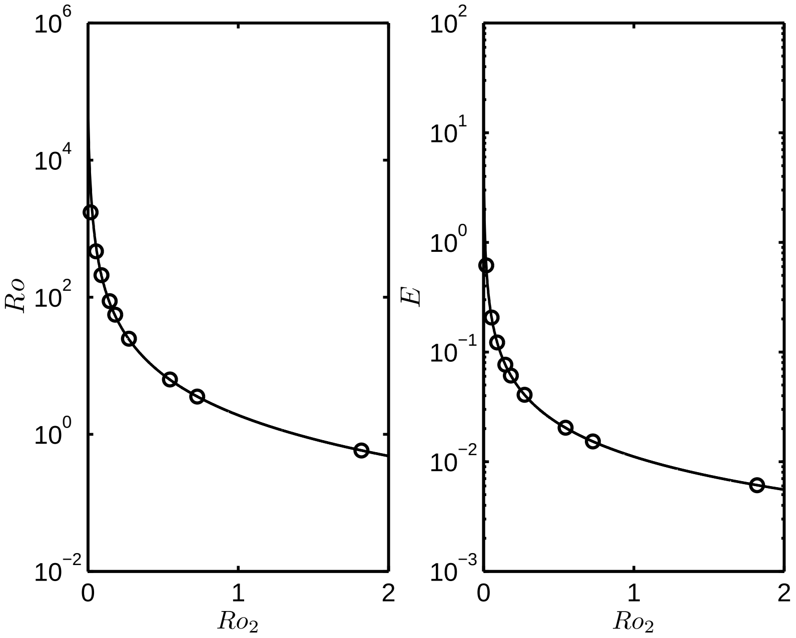

Figure 4.19: Variation of the Rossby number (left) and the Ekman number (right) from the fully turbulent to the laminar steady state, DNS ○ ; analytical solution for the laminar case —— .

4.4 Computations at $\mathrm{Re}_{\tau_0} = 360$

In the present section the DNS results obtained for a higher Re_{τ_0} at different rotation rates will be presented. It is well known that at relatively low Reynolds numbers the flow is still damped by viscous effects. So it is strongly anticipated that there is a Reynolds number dependence on the rotation rate for which the relaminarization of the flow starts. The main goal of this section is actually to study this dependency. Nine simulations have been performed for the rotation range $Ro_2 = 0 - 2.9$ at $Re_{\tau_0} = 360$. Similar to the computations at the lower Reynolds number ($Re_{\tau_0} = 180$) all three flow states have been observed for this range of rotation rates. The statistical and the flow structures in the different regions will be discussed and compared to the ones of the lower Reynolds number. The performed simulations have been summarized in the table 4.2.

The uniform grid resolution in the streamwise direction used for all simulation is given as follows:

$$\Delta x_1^+ \approx 8.67.$$

The resolution in the wall-normal (x_2) direction is fine near the walls and becomes coarser away from the wall due to the Chebyshev collocation points. The variation from the finest to the coarsest cells in this direction is as below:

$$\Delta x_2^+ \approx 0.026 - 4.32.$$

Table 4.2: Performed DNS at $Re_{\tau_0} = 360$.

Ro_2	Computational Domain	Grid	Flow State
0	$4\pi \times 2 \times 2\pi$	$512 \times 257 \times 256$	Turbulent
0.011	$4\pi \times 2 \times 6\pi$	$512 \times 257 \times 512$	Turbulent
0.028	$4\pi \times 2 \times 6\pi$	$512 \times 257 \times 512$	Turbulent
0.072	$4\pi \times 2 \times 8\pi$	$512 \times 257 \times 512$	Turbulent
0.18	$4\pi \times 2 \times 2\pi$	$512 \times 257 \times 256$	Quasi-laminar
0.36	$4\pi \times 2 \times 2\pi$	$512 \times 257 \times 256$	Quasi-laminar
1.08	$4\pi \times 2 \times 2\pi$	$512 \times 257 \times 256$	Laminar
1.8	$4\pi \times 2 \times 2\pi$	$512 \times 257 \times 256$	Laminar
2.9	$4\pi \times 2 \times 2\pi$	$512 \times 257 \times 256$	Laminar

In the spanwise direction a uniform grids at different resolutions have been used. They are summarized in table 4.3

Table 4.3: Grid resolutions in the spanwise direction at $Re_{\tau_0} = 360$.

Ro_2	Δx_3^+
0	8.67
0.011	13
0.028	13
0.072	17.34
0.18	8.67
0.36	8.67
1.08	8.67
1.8	8.67
2.9	8.67

4.4.1 Fully Turbulent Region

The simulations at $Ro_2 = 0, 0.011, 0.028$ and 0.072 have been qualified as fully turbulent. The results obtained for the statistical quantities will be presented in the following.

4.4.1.1 Mean Velocities

The mean velocity profiles in the streamwise and the spanwise directions are shown in figure 4.20. Similar to the simulation at lower Reynolds number ($Re_{\tau_0} = 180$) the flow at higher Reynolds number ($Re_{\tau_0} = 360$) is also very sensitive to the wall-normal rotation and indicates a similar behavior due to the increase in the rotation rate. A region with almost a constant value for log-law indicator function in the streamwise direction can only can be observed at $Ro_2 = 0.072$ (Figure 4.21). The absence of this region at lower rotation rates is obviously the effect of the higher-order terms usually included in the wake component of the velocity profile Hoyas & Jiménez (2006).

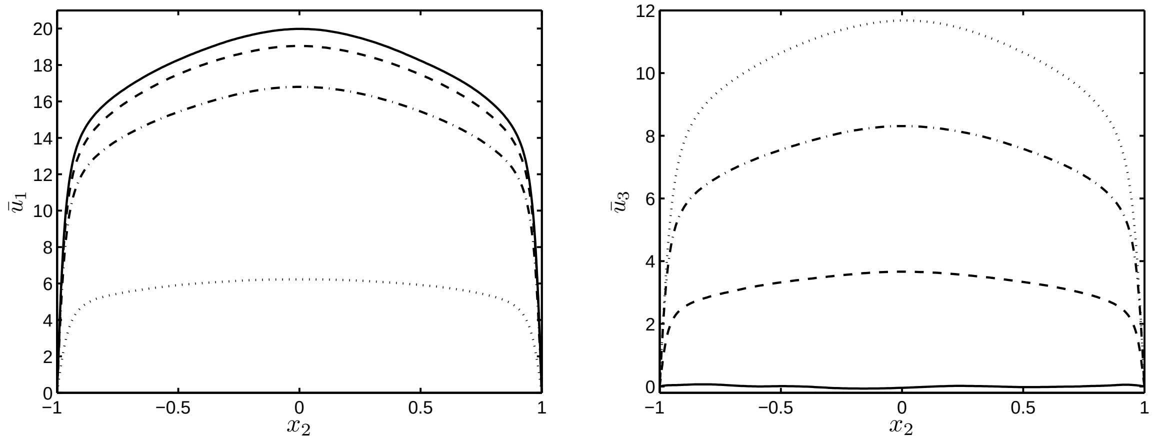

Figure 4.20: Mean velocities in the streamwise ($\bar{u}_1$) and in the spanwise ($\bar{u}_3$) directions at different rotation numbers: $Ro_2 = 0$ —— ; $Ro_2 = 0.011$ - - - ; $Ro_2 = 0.028$ —·— ; $Ro_2 = 0.072$ ··· .

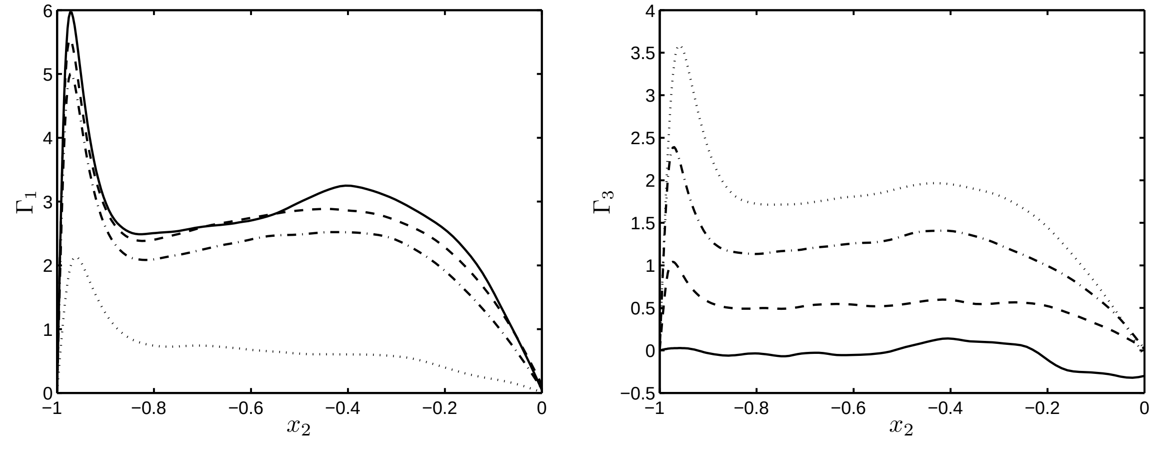

Figure 4.21: Log-law indicator functions (Γ_1 and Γ_3) at different rotation numbers: $Ro_2 = 0$ —— ; $Ro_2 = 0.011$ - - - ; $Ro_2 = 0.028$ —·— ; $Ro_2 = 0.072$ ··· .

4.4.1.2 Reynolds Stresses

The distribution of the Reynolds normal, turbulent kinetic energy and the shear stresses have been indicated in figures 4.22 and 4.23. A similar behavior for the normal stresses is observed compared to the simulations at $Re_{\tau_0} = 180$. The turbulent kinetic energy is also damped due to the increase in the rotation rate. The shear stresses, $\overline{u_1'u_2'}$ and $\overline{u_2'u_3'}$ have also linear distributions in the core region of the channel which is indicating that similar to the previous simulations, in the streamwise direction the Coriolis force and $\overline{u_1'u_2'}$ balance the pressure gradient and in the spanwise direction $\overline{u_3'u_2'}$ balances the Coriolis force. The slopes of the linear regions depend also on the rotation rate. However, comparison the slopes of the linear regions at the higher Reynolds number ($Re_{\tau_0} = 360$) to the ones of the lower Reynolds number ($Re_{\tau_0} = 180$), implies that the slops depend also on the Re_{τ_0}.
Similar to previous case the shear processes in the streamwise and the spanwise mean velocity contribute to the production of $\overline{u_1'u_3'}$. The distribution of $\overline{u_1'u_3'}$ is shown in figure 4.24 .

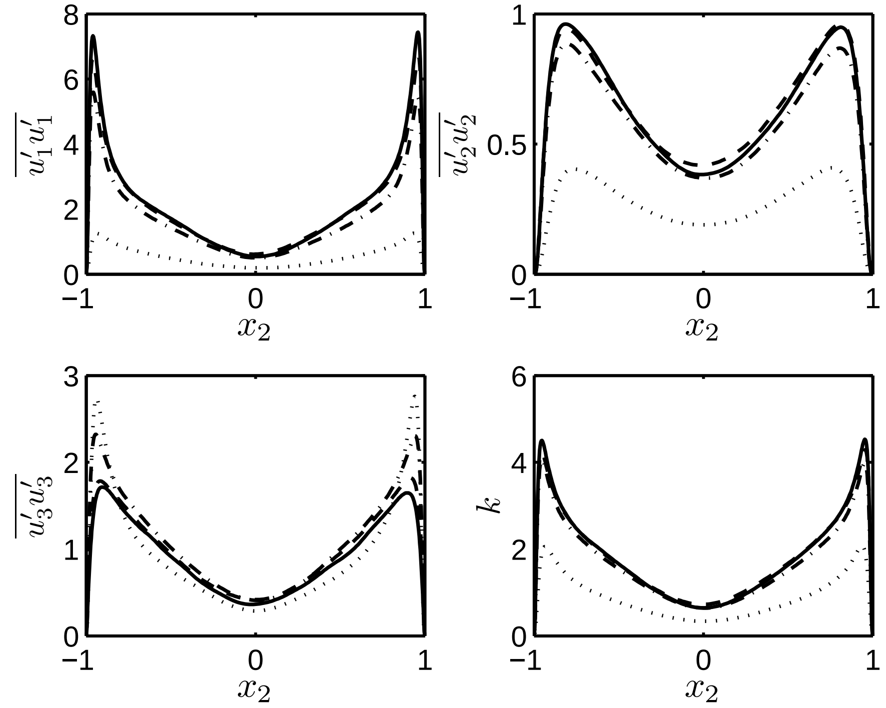

Figure 4.22: Turbulent normal stresses and the turbulent kinetic energy for different rates: $Ro_2 = 0$ —— ; $Ro_2 = 0.011$ - - - ; $Ro_2 = 0.028$ —·— ; $Ro_2 = 0.072$ $\cdots$.

In figure 4.25 the flatness factor A and the structure parameter a_1 for different rotation numbers is shown. Comparing flatness factor and the structure parameter for different rotation rates, indicates a negligible deviation from the non-rotating case. It has also been established that the deviation from the non-rotating case is decreased at the higher Reynolds number.

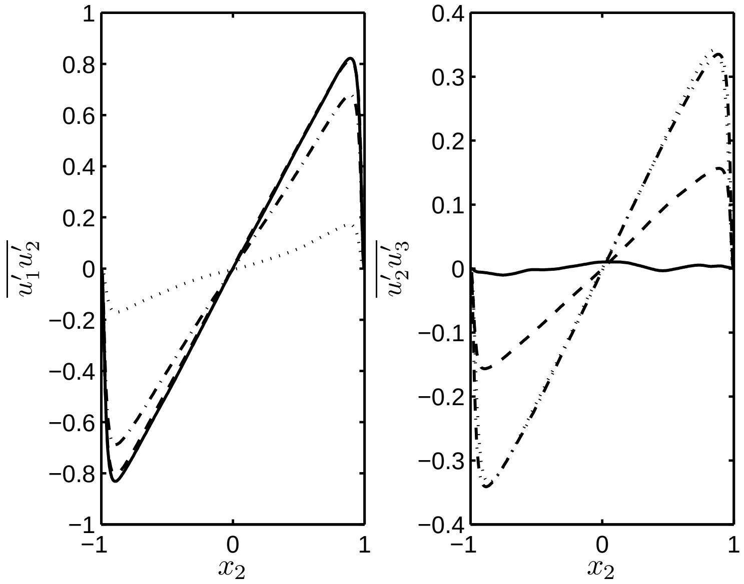

Figure 4.23: Turbulent shear stresses at different rotation rates: $Ro_2 = 0$ —— ; $Ro_2 = 0.011$ - - - ; $Ro_2 = 0.028$ —·— ; $Ro_2 = 0.072$ · · · .

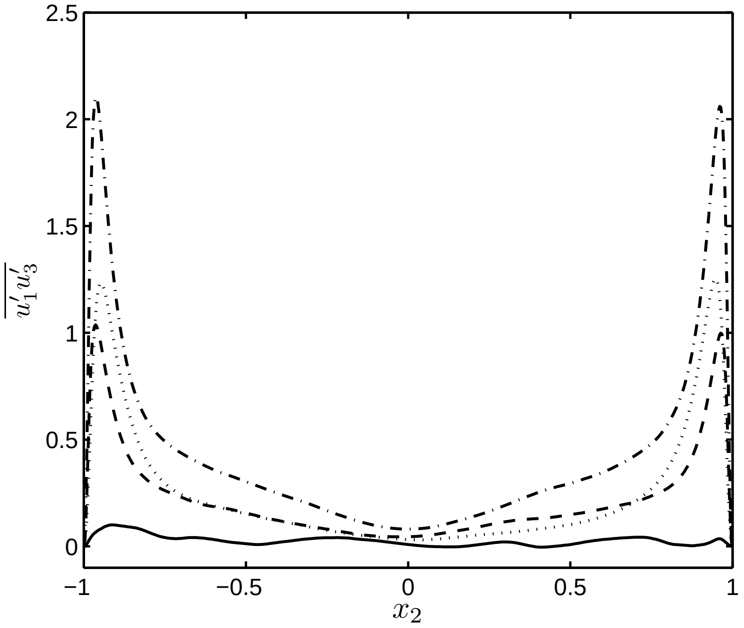

Figure 4.24: Distribution of $\overline{u_1'u_3'}$ at different rotation rates: $Ro_2 = 0$ —— ; $Ro_2 = 0.011$ - - - ; $Ro_2 = 0.028$ —·— ; $Ro_2 = 0.072$ · · · .

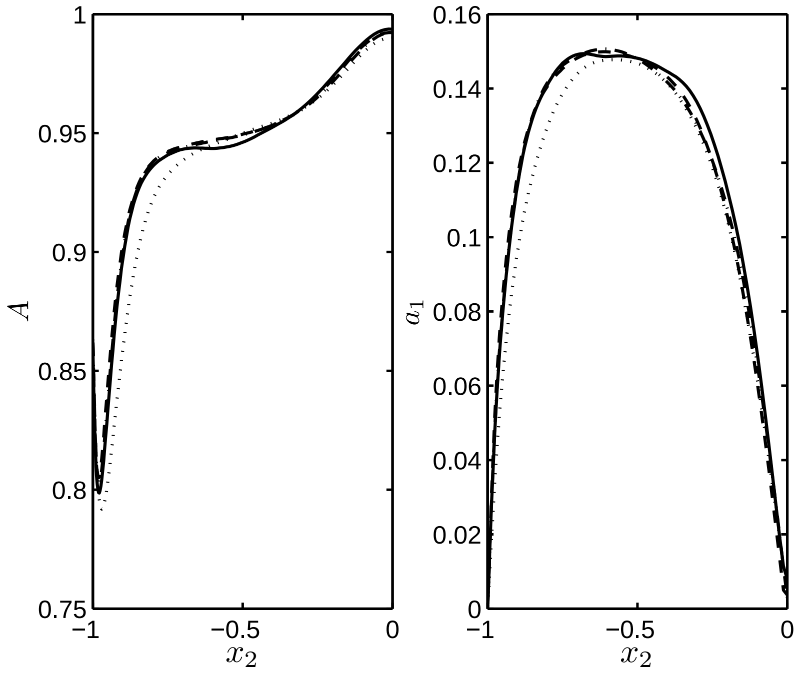

Figure 4.25: The flatness factor (left) and the Structure parameter (right) in the fully turbulent region for different rotation rates: $Ro_2 = 0$ —— ; $Ro_2 = 0.011$ - - - ; $Ro_2 = 0.028$ —·— ; $Ro_2 = 0.072$ · · · .

4.4.1.3 Vorticities

Non-dimensionalized rms vorticity fluctuations for different rotation rates have been shown in figure 4.26. They indicate very similar behavior compared to the ones at lower Reynolds number. However, the region in which they are almost isotrop is extended and it is to anticipate that at higher Reynolds numbers this region will be more extended.

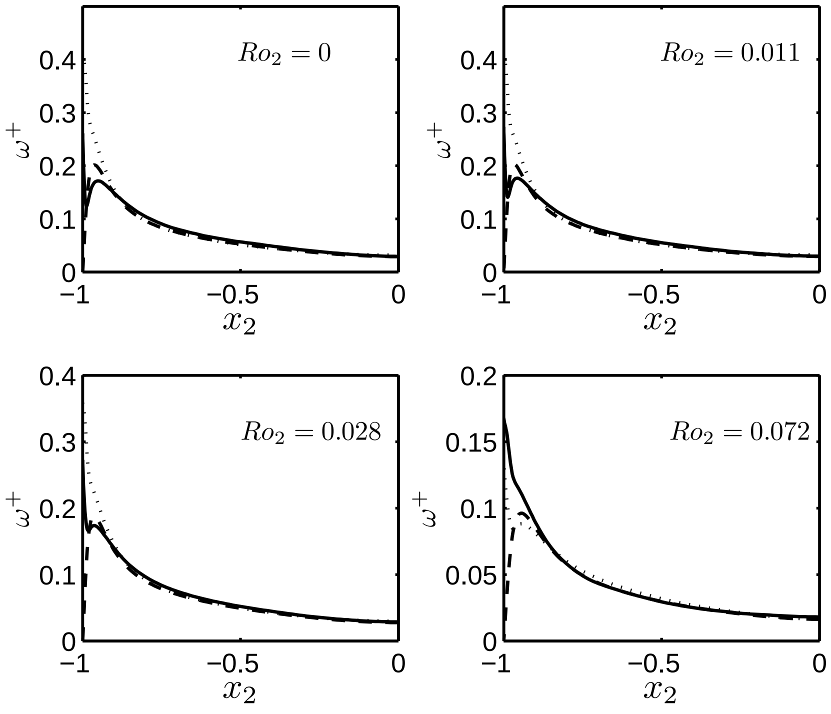

Figure 4.26: Normalized r.m.s vorticity fluctuations for different rotation rates: ω_1^+ —— ; ω_2^+ - - - ; ω_3^+ · · · .

4.4.2 Quasi-Laminar Region

A result of the further increasing the rotation rate bejond a certain threshold is the relaminarization of the flow, which was observed at the previous simulations for $Re_{\tau_0} = 180$. However, in the present case ($Re_{\tau_0} = 360$) a higher rotation rate is needed to start the relaminarization and lead the flow to the quasi-laminar state. The simulations for $Ro_2 = 0.18$ and $Ro_2 = 0.36$ have been qualified as quasi-laminar state. The Reynolds numbers in this region are below the corresponding critical ones based on the results obtained by Hoffmann & Busse (2001). Similar to the simulations for $Re_{\tau_0} = 180$ the inflection points first appear in the streamwise mean velocity profile and then at higher rotation rate they are also visible in the spanwise mean velocity profile. The mean velocity profiles and the log-law indicator functions are given in figures 4.27.and 4.28. The coherent structures can also be observed in this Ro_2 domain (Figure 4.29). Again the inflectional mechanism is thought to be the main reason of their appearance. Finally at about $Ro_2 = 1.08$ the flow is completely laminarized and reaches a fully laminar steady state.

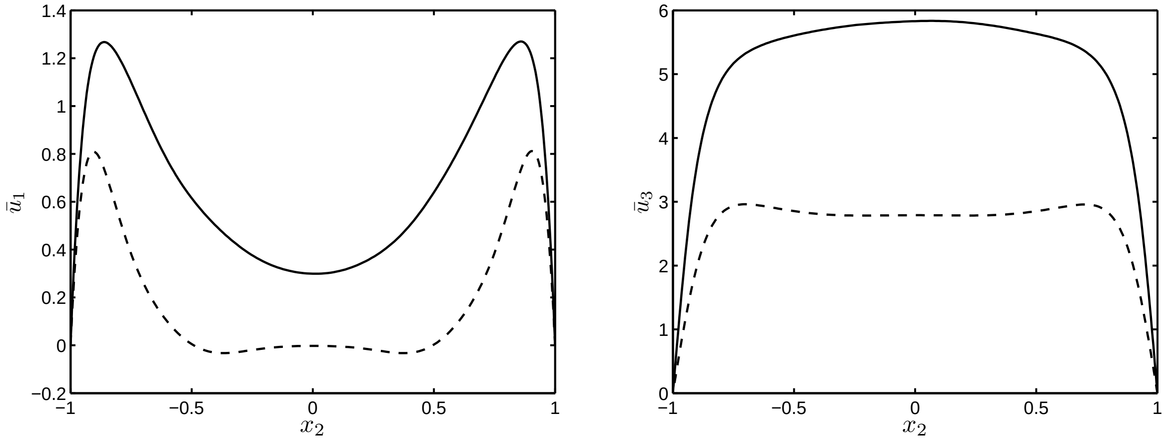

Figure 4.27: Mean velocities in the streamwise ($\bar{u}_1$) and in the spanwise ($\bar{u}_3$) directions and in the quasi-laminar region for different rotation numbers: $Ro_2 = 0.18$ —— ; $Ro_2 = 0.36$ - - - .

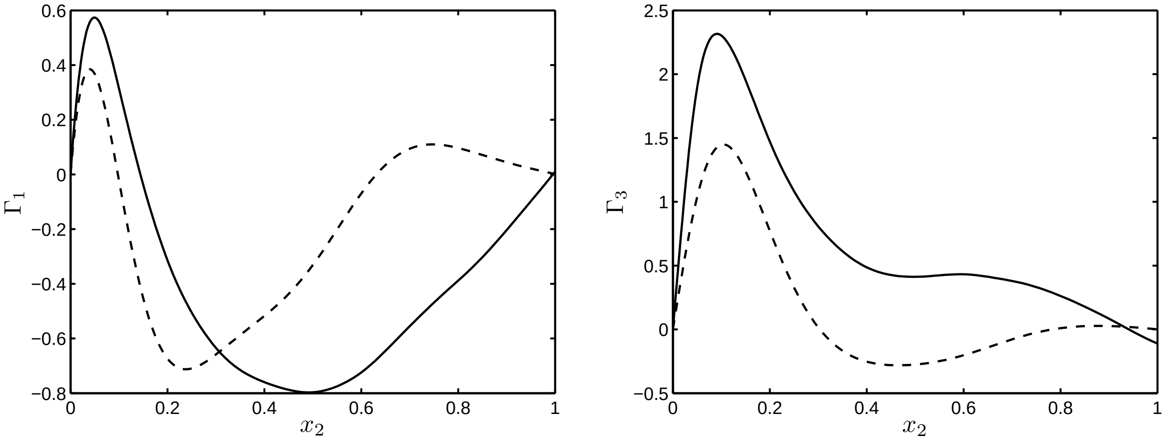

Figure 4.28: Log-law indicator functions (Γ_1 and Γ_3) in the quasi-laminar region at different rotation numbers: $Ro_2 = 0.18$ —— ; $Ro_2 = 0.36$ - - - .

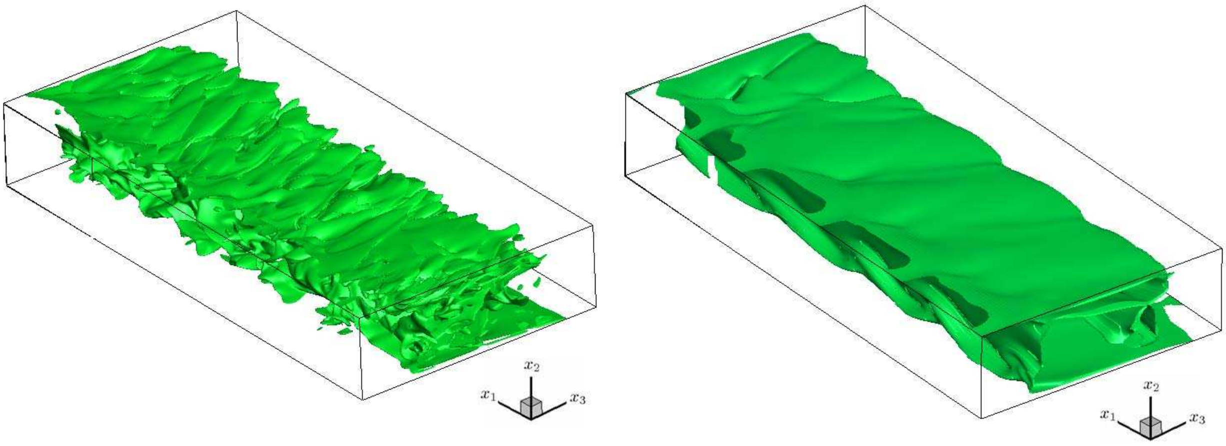

Figure 4.29: Elongated coherent structures in the quasi-laminar region for $Ro = 0.18$ at $\omega_3 = 0.015$ (left) and $Ro = 0.36$ at $\omega_1 = 0.0025$ (right).

4.4.3 Laminar Region

A result of further increasing the rotation rate ($Ro_2 > 1.08$) is a complete suppression of turbulence and hence a vanishing Reynolds stress tensor. As a result, a steady laminar flow is observed. For the present subsection three simulations at $Ro = 1.08, 1.8$ and 2.9 have been calculated. There is a very good agreement between the results obtained from the DNS and the analytical solutions. In all computations for $Ro_2 > 1.08$ the deviation of the DNS results from the analytical solution is very small. The variations of Ro_2 and its effect on the bulk mean velocities, the friction velocities, the Rossby number and the Ekman number from the fully turbulent state to the fully laminar steady state are shown in the figures 4.30, 4.31 and 4.32 . The solid lines are the analytical solutions for the laminar case. It is plotted starting with $Ro_2 = 0.072$, which is the border between the fully turbulent and the quasi-laminar regions. Similar to the previous simulations one may deduce that the quasi-laminar region has more in common with the fully laminar state than to the fully turbulent state.

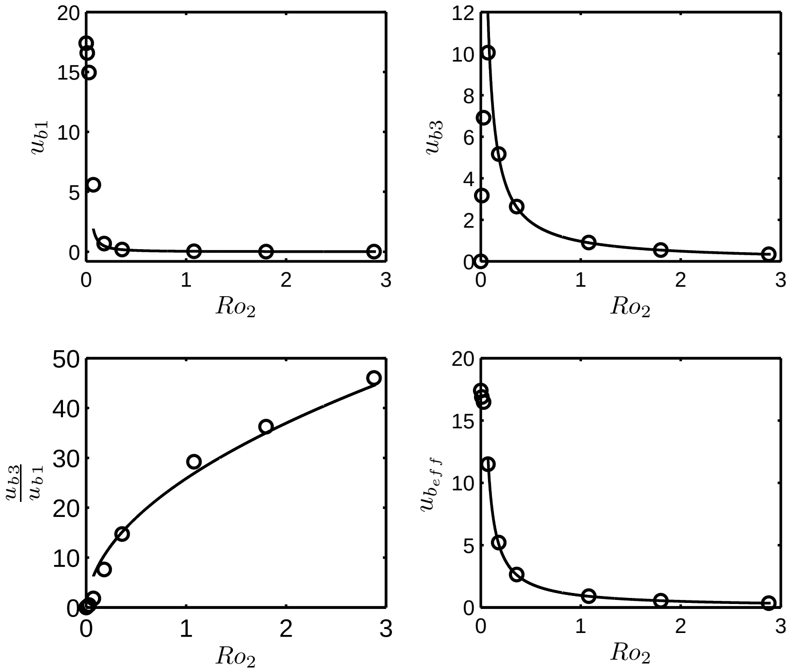

Figure 4.30: Variation of the mean bulk velocities in the streamwise and the spanwise directions, their ratio and the effective friction velocity from the fully turbulent to the laminar steady state, DNS ○ ; analytical solution for the laminar case —— .

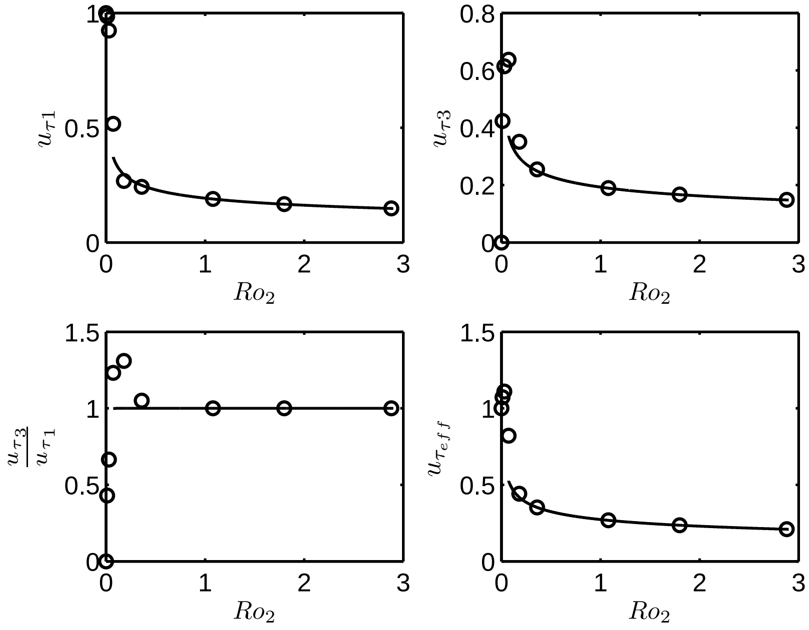

Figure 4.31: Variation of the friction velocities in the streamwise and the spanwise directions, their ratio and the effective friction velocity from the fully turbulent to the laminar steady state, DNS ○ ; analytical solution for the laminar case —— .

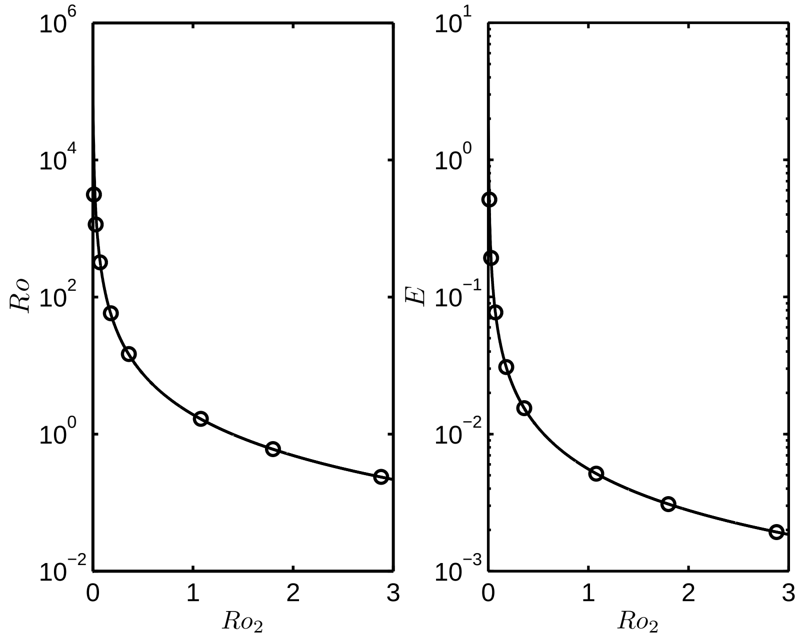

Figure 4.32: Variation of the Rossby number (left) and the Ekman number (right) from the fully turbulent to the laminar steady state, DNS ○ ; analytical solution for the laminar case —— .

4.5 Comparison with the turbulent Ekman layer

As mentioned in the last section there are some commonalities between the laminar wall-normal rotating channel flow and the laminar Ekman layer. Hence, it may also be reasonable to compare the turbulent wall-normal rotating channel flow with the turbulent Ekman layer. The turbulent Ekman layer is a model for engineering 3DBLs such as those found on swept-wing aircraft, as well as an idealization of the Earth's planetary boundary layer.

Coleman, Ferziger & Spalart (1990) and recently Spalart, Coleman & Johnstone (2008) have studied the turbulent Ekman layer using direct numerical simulation. In both investigations strong similarities with two-dimensional boundary layers was observed and therefore was concluded that the turbulent Ekman layer is as legitimate as a two dimensional channel or boundary layer as a case study of wall-bounded turbulence theory. Similar to the wall-normal rotating channel flow, a reduction of the turbulence intensity and an increase of the angle of the friction velocity with respect to the streamwise direction (geostrophic wind direction) have also been established by Coleman and Spalart due to the increase in the rotation rate. Shingai & Kawamura (2004) have also explored the turbulent Ekman layer by means of DNS at different rotation rates. The same behaviors for the turbulence intensity and the angle of the friction velocity against the rotation rate have been observed. They linked the increase of the angle of the friction velocity to the reduced momentum transfer in the vertical direction due to the increase in the rotation rate. The same is also true for turbulent wall-normal rotating channel flow. The rotation rates, the corresponding friction velocities in the streamwise and the spanwise directions and the angles of the friction velocities with respect to the streamwise direction (α) for the present flow for both Reynolds numbers (Re_{τ_0}) have been listed in the following tables.

Ro_2	$u_{\tau 1}$	$u_{\tau 3}$	α°
0	1	0	0
0.018	0.96	0.513	28.12
0.054	0.709	0.681	43.84
0.091	0.472	0.59	51.34

Table 4.4: Rotation rate dependence of friction velocity components and their angles with respect to the streamwise direction at $Re_{\tau_0} = 180$.

Ro_2	$u_{\tau 1}$	$u_{\tau 3}$	α°
0	1	0	0
0.011	0.985	0.423	23.24
0.028	0.9239	0.6141	33.61
0.072	0.517	0.6371	50.94

Table 4.5: Rotation rate dependence of friction velocity components and their angles with respect to the streamwise direction at $Re_{\tau_0} = 360$.

4.6 Summary and Conclusion

In this chapter turbulent channel flow with wall-normal rotation has been investigated using DNS. Similar to the laminar case it was found that the turbulent flow is also very sensitive to the wall-normal rotation and even a very small rotation rate is able to induce a strong secondary flow in the spanwise direction. However, the effects of the wall-normal rotation are first visible in the mean velocity profiles. It was also established that the Reynolds stress field is only slightly affected by the wall-normal rotation and therefore the flatness factor indicates only a weak deviation from the non-rotating turbulent channel flow. The structure parameter in the fully turbulent region shows hardly a difference compared to the non-rotating case. For these reasons one may deduce that the flow physics of turbulent wall-normal rotating channel flow could be regarded assimilar to the turbulent non-rotating channel flow with a tilting angle to the spanwise direction. Furthermore, it has been established that the turbulent wall-normal rotating channel flow has a lot in common with the turbulent Ekman layer. Due to the increase in the rotation rate the turbulence intensity is damped, the angle of the friction velocity with respect to the streamwise direction is increased up to the point where the flow reaches the quasi-laminar state. Obviously the rotation rate at which the flow is led to the quasi-laminar state depends on the Reynolds number (Re_{τ_0}). The higher the Reynolds number the higher the rotation rate is needed. In this region elongated (roll-like) structure can be observed whose existence is thought to be the inflectional mechanism. By further increasing the rotation rate turbulence is completely damped and the flow reaches the fully laminar steady state for which there is an analytical solution.

5 Lie Group Analysis

5.1 Introduction

Sophus Lie made major advances in the theory of continuous groups of transformations and differential equations. He largely created the theory of continuous symmetry, and applied it to the study of geometry and differential equations. Lie's principal tool, and one of his greatest achievements, was the discovery that continuous transformation groups (now called, after him, Lie groups) could be better understood by linearizing them and studying the corresponding generating vector fields (the so called infinitesimal generators). The generators are subject to a linearized version of the group law, now called the commutator bracket and have the structure of what is called a Lie algebra.

Sophus Lie, born in 1842 in Nordfjordeide, Norway, studied science at the University of Kristiania (now Oslo). His interest in geometry deepened in 1868 and resulted in his first mathematical paper being published in Crelle's Journal in 1869.

In 1871 Lie became an assistant tutor at Kristiania and submitted his doctoral dissertation on the theory of contact transformations. In 1872 he became professor in Kristiania and began his research continuous transformation groups in 1873. In 1986 he was appointed as a professor in Leipzig. In collaboration with Friedrich Engel, he published *Theory of Transformation Groups* (1888-1893), which contains his investigations of the general theory of continuous groups.

In 1898 Lie returned to Kristiania to accept a special professor post created for him, where he died soon after his arrival. Beside his development of transformation groups, he made contributions to differential geometry. His primary aim, however, was the advancement of the theory of differential equations.

5.2 Symmetries of Differential Equations

A symmetry of a system of differential equations is a transformation that maps any solution to another solution of the system, (see Bluman & Kumei (1996) and Oliver (1993)). These groups constitute an important tool in the development in many of mathematical and physical areas. The applications of these groups include algebraic topology, differential geometry, special functions, relativity, etc. Since the Lie symmetry methods are not widely known in engineering applications, a short introduction into the topic is given here. If a system of partial differential equations is given as follows:

$$\boldsymbol{F}(\boldsymbol{x}, \boldsymbol{y}, \boldsymbol{y}^{(1)}, \boldsymbol{y}^{(2)}, ...) = 0 \tag{5.1}$$

where $\boldsymbol{x}$ is the independent and $\boldsymbol{y}$ the dependent variables, then the variable transformation

$$\boldsymbol{x}^* = \boldsymbol{\Phi}(\boldsymbol{x}, \boldsymbol{y}) \qquad \boldsymbol{y}^* = \boldsymbol{\Psi}(\boldsymbol{x}, \boldsymbol{y}) \tag{5.2}$$

is called a symmetry transformation of equation (5.1) if

$$\boldsymbol{F}(\boldsymbol{x}, \boldsymbol{y}, \boldsymbol{y}^{(1)}, \boldsymbol{y}^{(2)}, ...) = 0 \Longleftrightarrow \boldsymbol{F}(\boldsymbol{x}^*, \boldsymbol{y}^*, \boldsymbol{y}^{*(1)}, \boldsymbol{y}^{*(2)}, ...) = 0 \tag{5.3}$$

holds. $\boldsymbol{y}^{(n)}$ refers to the set of all n^{th} order derivatives of $\boldsymbol{y}$ with respect to $\boldsymbol{x}$.

The intention of the symmetry analysis is to find all Lie symmetries

$$\boldsymbol{x}^* = \boldsymbol{\Phi}(\boldsymbol{x}, \boldsymbol{y}; \varepsilon), \qquad \boldsymbol{y}^* = \boldsymbol{\Psi}(\boldsymbol{x}, \boldsymbol{y}; \varepsilon), \tag{5.4}$$

where ε is called the group parameter. Since ε may take any value $\varepsilon \in \mathrm{Re}$, equation (5.4) is also called continuous group.

Lie's first theorem shows, that if a transformation has group properties it can be represented by its infinitesimal form, which still contains the essential information. This means, that the transformation can be expanded for the group parameter of the transformation:

$$\boldsymbol{x}^* = \boldsymbol{x} + \varepsilon \boldsymbol{\xi}(\boldsymbol{x}, \boldsymbol{y}) + \mathcal{O}(\varepsilon^2), \tag{5.5}$$

$$\boldsymbol{y}^* = \boldsymbol{y} + \varepsilon \boldsymbol{\eta}(\boldsymbol{x}, \boldsymbol{y}) + \mathcal{O}(\varepsilon^2), \tag{5.6}$$

where

$$\boldsymbol{\xi}(\boldsymbol{x}, \boldsymbol{y}) = \left.\frac{\partial \boldsymbol{\Phi}}{\partial \varepsilon}\right|_{\varepsilon=0}, \quad \boldsymbol{\eta}(\boldsymbol{x}, \boldsymbol{y}) = \left.\frac{\partial \boldsymbol{\Psi}}{\partial \varepsilon}\right|_{\varepsilon=0}. \tag{5.7}$$

If the infinitesimal of a transformation is given, their global form can be determined by integrating the first order system using Lie's first theorem (Bluman & Anco 2002):

$$\frac{d\boldsymbol{x}^*(\varepsilon)}{d\varepsilon} = \boldsymbol{\xi}(\boldsymbol{x}^*(\varepsilon), \boldsymbol{y}^*(\varepsilon)), \qquad \frac{d\boldsymbol{y}^*(\varepsilon)}{d\varepsilon} = \boldsymbol{\eta}(\boldsymbol{x}^*(\varepsilon), \boldsymbol{y}^*(\varepsilon)) \tag{5.8}$$

with the initial conditions:

$$\varepsilon = 0 : \boldsymbol{x}^* = \boldsymbol{x} \text{ and } \boldsymbol{y}^* = \boldsymbol{y}.$$

The advantage of symmetry groups is their algorithmic nature. Thus, a variety of software packages are available to find continuous symmetry groups for essentially every differential equation. In the present work the software package "GEM" developed by Cheviakov (2007), has been used to perform the symmetry analysis. GEM is a Maple-based module and is capable of finding all local symmetries (up to a prescribed derivative order), approximate symmetries (Fushchich and Shtelen type) and conservation laws for any ODE/PDE system, generally without limitation in derivative order and number of variable.

5.3 Invariant Solutions

Invariant solution can be derived from the symmetries of a differential equation. $\boldsymbol{y} = \boldsymbol{\Theta}(\boldsymbol{x})$ is an invariant solution of a differential equation if $[\boldsymbol{y} - \boldsymbol{\Theta}(\boldsymbol{x})]$ is an invariant function with respect to the operator X, which is given by

$$X = \xi_i \frac{\partial}{\partial x_i} + \eta_j \frac{\partial}{\partial y_j}, \tag{5.9}$$

and if $\boldsymbol{y} = \boldsymbol{\Theta}(\boldsymbol{x})$ is a solution of differential equation. Therewith we obtain

$$X[\boldsymbol{y} - \boldsymbol{\Theta}(x)] = 0 \quad \text{with} \quad \boldsymbol{y} = \boldsymbol{\Theta}(x). \tag{5.10}$$

Expanding the derivatives in (5.10) by using X according to (5.9), we obtain the hyperbolic system

$$\xi_k(\boldsymbol{x}, \boldsymbol{\Theta}) \frac{\partial \theta_l}{\partial x_k} = \eta_l(\boldsymbol{x}, \boldsymbol{\Theta}) \tag{5.11}$$

and the corresponding characteristic equation

$$\frac{dx_1}{\xi_1(\boldsymbol{x}, \boldsymbol{\Theta})} = \frac{dx_2}{\xi_2(\boldsymbol{x}, \boldsymbol{\Theta})} = \cdots = \frac{dx_m}{\xi_m(\boldsymbol{x}, \boldsymbol{\Theta})} = \frac{dy_1}{\eta_1(\boldsymbol{x}, \boldsymbol{\Theta})} = \frac{dy_2}{\eta_2(\boldsymbol{x}, \boldsymbol{\Theta})} = \cdots = \frac{dy_n}{\eta_n(\boldsymbol{x}, \boldsymbol{\Theta})}. \tag{5.12}$$

After solving the characteristic equation one obtains the new variables. For this reason it is suggestive to take the $m-1$ solutions of the m equations on the left hand side as new independent variables. Each term of the n terms of the right hand side can set equal to one of the m terms on the left hand side. Due to this procedure the set of independent variables in the original partial differential equation (PDE) reduces at least by one. By generating invariant solutions, symmetries are partly or completely broken due to external (boundary) conditions.

5.4 Application to the Present Turbulent Rotating Channel Flow

The general purpose of the Lie group analysis, also called symmetry analysis, can be divided into two categories:

Category 1: using symmetry analysis as a mathematical tool to guide the development of dynamical equations. For instance, the symmetries of Navier-Stokes equations can be used to keep the consistency of a turbulence model as much as possible.
Category 2: using symmetry analysis to find self-similar (invariant) solution or some scaling laws of a given system of differential equation.
In the present work , the Lie procedure has been applied to the RANS equations up to the second moment level, written for a steady, incompressible turbulent channel flow with wall-normal rotation to find some invariant solution or some scaling laws. Assuming all statistics depending only on x_2 (i.e. homogeneity condition in the x_1 and the x_3) we obtain :

$$0 = -\frac{1}{\rho}\frac{\partial \bar{p}}{\partial x_1} - \frac{\partial \overline{u_1'u_2'}}{\partial x_2} + \nu\frac{\partial^2 \bar{u}_1}{\partial x_2^2} - 2\,\Omega_2 \bar{u}_3, \tag{5.13}$$

$$0 = -\frac{1}{\rho}\frac{\partial \bar{p}}{\partial x_2} - \frac{\partial \overline{u_2'u_2'}}{\partial x_2}, \tag{5.14}$$

$$0 = -\frac{\partial \overline{u_2'u_3'}}{\partial x_2} + \nu\frac{\partial^2 \bar{u}_3}{\partial x_2^2} + 2\,\Omega_2 \bar{u}_1, \tag{5.15}$$

$$\begin{aligned} 0 = &-\overline{u_i'u_2'}\frac{\partial \bar{u}_j}{\partial x_2} - \overline{u_j'u_2'}\frac{\partial \bar{u}_i}{\partial x_2} - 2\nu\overline{\frac{\partial u_i'}{\partial x_2}\frac{\partial u_j'}{\partial x_2}} + \overline{\frac{p'}{\rho}\Big(\frac{\partial u_i'}{\partial x_j} + \frac{\partial u_j'}{\partial x_i}\Big)} \\ &+\frac{\partial}{\partial x_2}\Big[-\overline{u_i'u_j'u_2'} + \nu\frac{\partial \overline{u_i'u_j'}}{\partial x_2} - \overline{\frac{p'}{p}(\delta_{2j}u_i' + \delta_{2i}u_j')}\Big] - 2\Omega_2\left[e_{2li}\overline{u_j'u_l'} + e_{2lj}\overline{u_i'u_l'}\right]. \end{aligned} \tag{5.16}$$

Since the symmetries are mostly broken by applying the boundary conditions, the analysis has been performed for the core region of the channel. For simplicity it will be assumed for the analysis that the Reynolds number tends to infinity, so that the viscous terms in the RANS equations can be neglected. The basis for this assumption is the fact that, viscosity has almost no effect as $Re \to \infty$. Without the simplification the equations are so complicate that the package fails to work properly and can not deliver any result. Finally the system of differential equation (simplified RANS equations by setting $\nu = 0$) used for Lie group analysis are as follows:

$$0 = G - \frac{\partial \overline{u_1'u_2'}}{\partial x_2} - 2\,\Omega_2 \bar{u}_3 \tag{5.17a}$$

$$0 = -\frac{1}{\rho}\frac{\partial \bar{p}}{\partial x_2} - \frac{\partial \overline{u_2'u_2'}}{\partial x_2} \tag{5.17b}$$

$$0 = -\frac{\overline{u_2'u_3'}}{\partial x_2} + 2\,\Omega_2 \bar{u}_1 \tag{5.17c}$$

$$0 = -\overline{u'_i u'_2}\frac{\partial \bar{u}_j}{\partial x_2} - \overline{u'_j u'_2}\frac{\partial \bar{u}_i}{\partial x_2} + g_{ij} - 2\Omega_2\left[e_{2li}\overline{u'_j u'_l} + e_{2lj}\overline{u'_i u'_l}\right] \tag{5.17d}$$

where $G = -\frac{1}{\rho}\frac{\partial \bar{p}}{\partial x_1}$ and g_{ij} includes the unclosed terms in the transport equation for Reynolds stress tensor. Note that for the Lie group analysis the g_{ij} has been taken as a dependent variable like mean velocities and the Reynolds stresses. x_2 is the only independent variable and Ω_2 is the only free constant.

5.5 Results and Discussion

Applying the GEM software package to the RANS equations ((5.17)), the following infinitesimals for x_2, mean velocity profiles in the streamwise and the spanwise directions ($\bar{u}_1$, $\bar{u}_3$) and for shear stresses have been obtained :

$$\xi_{x_2} = C_1{x_2}^2 + C_2\, x_2 + C_3, \tag{5.18}$$

$$\eta_{\bar{u}_1} = \frac{(-2\,\Omega_2\,\bar{u}_1 x_2 + \tau_{23},)\, C_1 + 2\,\Omega_2\,\bar{u}_1 C_4 + C_5 - 2\,\Omega_2\,\bar{u}_1 C_2}{2\Omega_2} \tag{5.19}$$

$$\eta_{\bar{u}_3} = \frac{(-2\,\bar{u}_3 x_2 \Omega_2 - \tau_{12} + x_2 G C_1 + (G - 2\,\Omega_2\,\bar{u}_3)\, C_2 + (2\,\Omega_2\,\bar{u}_3 - G)\, C_4) - C_6}{2\Omega_2}, \tag{5.20}$$

$$\eta_{\tau_{23}} = C_1\,\tau_{23} x_2 + x_2 C_5 + C_4\,\tau_{23} + C_8, \tag{5.21}$$

$$\eta_{\tau_{12}} = \tau_{12} x_2 C_1 + \tau_{12} C_4 + C_6\, x_2 + C_7, \tag{5.22}$$

where $\tau_{12} = \overline{u_1^{'} u_2^{'}}$, $\tau_{23} = \overline{u_2^{'} u_3^{'}}$.

Note that only the above infinitesimals are needed to construct a self similar solution for the shear stresses and mean velocities. The full set of infinitesimals is given in appendix A.

Based on the invariant surface condition (5.12), we have the following relations:

$$\frac{d\eta_{\tau_{12}}}{\eta_{\tau_{12}}} = \frac{dx_2}{\xi_{x_2}}, \tag{5.23}$$

$$\frac{d\eta_{\tau_{23}}}{\eta_{\tau_{23}}} = \frac{dx_2}{\xi_{x_2}}, \tag{5.24}$$

which lead to the following differential equations:

$$\eta_{\tau_{12}} - \xi_{x_2}\frac{d\tau_{12}}{dx_2} = 0, \tag{5.25}$$

$$\eta_{\tau_{23}} - \xi_{x_2}\frac{d\tau_{23}}{dx_2} = 0. \tag{5.26}$$

Since the ξ_{x_2} has a quadratic form, we have to study the following three different cases:

$$\xi_{x_2} = C_1{x_2}^2 + C_2\, x_2 + C_3 \quad , \qquad \Delta = -4C_1C_3 + (C_2)^2 = 0, \tag{5.27}$$

$$\xi_{x_2} = C_1{x_2}^2 + C_2\, x_2 + C_3 \quad , \qquad \Delta = -4C_1C_3 + (C_2)^2 > 0, \tag{5.28}$$

$$\xi_{x_2} = C_1 {x_2}^2 + C_2\, x_2 + C_3 \quad , \qquad \Delta = -4C_1C_3 + (C_2)^2 < 0. \tag{5.29}$$

By solving the equations (5.25) and (5.26) for the cases $\Delta < 0$ and $\Delta > 0$, a linear profile for τ_{12} and τ_{23} has been directly obtained:

$$\tau_{12} = \frac{-C_7C_4 + C_7C_2 - C_6C_3 - (C_6C_4 - C_7C_1)x_2}{C_4^2 - C_4C_2 + C_1C_3}, \tag{5.30}$$

$$\tau_{23} = \frac{-C_8C_4 + C_8C_2 - C_5C_3 - (C_5C_4 - C_8C_1)x_2}{C_4^2 - C_4C_2 + C_1C_3}. \tag{5.31}$$

In the case of $\Delta = 0$, there is a larger solution space for τ_{12} and τ_{23} , which includes a linear profile as below:

$$\tau_{12} = \sqrt{C_1x_2^2 + C_2x_2 + C_3} \cdot e^{\frac{C_2-2C_4}{2C_1x_2+C_2}} \int \frac{(C_6x_2 + C_7)e^{-\frac{1}{2}\ln(C_1x_2^2+C_2x_2+C_3)+\frac{-C_2+2C_4}{2C_1x_2+C_2}}}{C_1{x_2}^2 + C_2\, x_2 + C_3} dx_2, \tag{5.32}$$

$$\tau_{23} = \sqrt{C_1x_2^2 + C_2x_2 + C_3} \cdot e^{\frac{C_2-2C_4}{2C_1x_2+C_2}} \int \frac{(C_5x_2 + C_8)e^{-\frac{1}{2}\ln(C_1x_2^2+C_2x_2+C_3)+\frac{-C_2+2C_4}{2C_1x_2+C_2}}}{C_1{x_2}^2 + C_2\, x_2 + C_3} dx_2. \tag{5.33}$$

Although the above integrals can not be solved analytically, by setting $C_2 = 2C_4$ they reduce to linear forms for τ_{12} and τ_{23} as follows:

$$\tau_{12} = \frac{-C_6C_3 + C_7C_4 - (C_6C_4 - C_7C_1)x_2}{-C_4^2 + C_1C_3}, \tag{5.34}$$

$$\tau_{23} = \frac{-C_5C_3 + C_8C_4 - (C_5C_4 - C_8C_1)x_2}{-C_4^2 + C_1C_3}. \tag{5.35}$$

Based on the results obtained for the three cases, one may deduce that only the commonality of the three cases (linear profile) could be the solution for the shear stresses in the core region, which is also the case in the results obtained from DNS. The coefficients (C_i with i=1 to 8) are arbitrary functions of the rotation rate (Ω_2), which can be chosen also as arbitrary constants. As an example, by setting $C_4 = C_5 = C_6 = 0$, $\frac{C_7}{C_3} = f(\Omega_2)$ and $\frac{C_8}{C_3} = g(\Omega_2)$, the equations (3.34) and (3.35) can be written in the following forms:

$$\tau_{12}(x_2, \Omega_2) = f(\Omega_2)x_2, \tag{5.36}$$

$$\tau_{23}(x_2, \Omega_2) = g(\Omega_2)x_2. \tag{5.37}$$

Note that exactly the same results can also be obtained using equations (5.30) and (5.31).

Inserting (5.36) and (5.37) in the mean flow equations ($(5.17a)$, $(5.17c)$) leads to a constant distribution depending on the rotation rate for the mean velocities in the spanwise and the streamwise directions in the core region of the channel. Although the above analysis has been performed for turbulent channel flow with wall-normal rotation at very high Reynolds number ($Re \rightarrow \infty$), some of the obtained results such as a linear distribution for shear stresses and constant angle of the bulk flow (γ) with respect to the streamwise direction (i.e. constant value for $\gamma = tan^{-1}(\bar{u}_3/\bar{u}_1)$) in the core region can also be observed at lower Reynolds numbers. They have been shown in Figures $5.1-5.3$. A small deviation from a constant distribution for γ can be seen by approaching the quasi-laminar region around $Ro = 0.091$ for $Re_{\tau 0} = 180$ and $Ro = 0.072$ for $Re_{\tau 0} = 360$. The absence of constant distributions for the mean velocities at relatively low Reynold numbers implies that neglecting the viscous effects except at very high Reynolds numbers ($Re \to \infty$) even in the core region, might be a too strong approximation. In other words, the mean velocities are more sensitive to the viscous effects compared to the shear stresses and the angle of the flow and the effects can be first observed in the mean velocity profiles in this region when the Reynolds number is not sufficiently high.

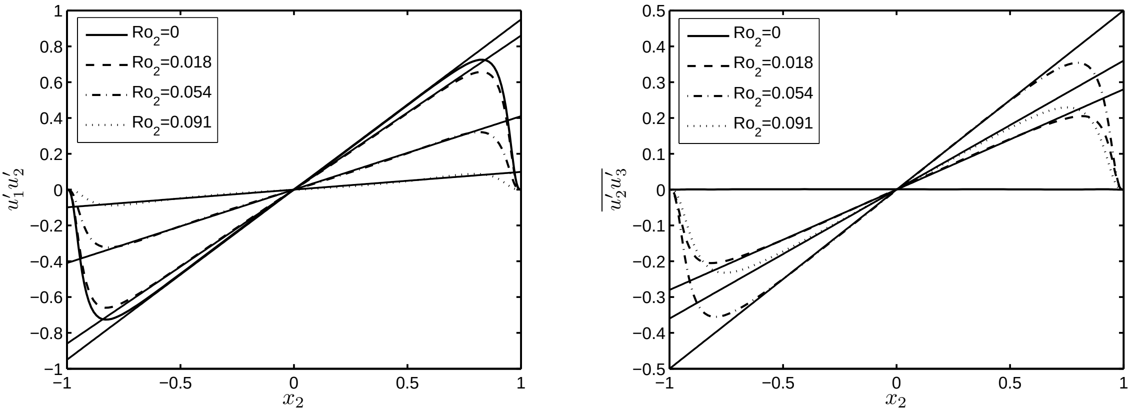

Figure 5.1: Distribution of the shear stresses in the channel and the linear approximation of them in the core region at $Re_{\tau 0} = 180$ for different rotation rates.

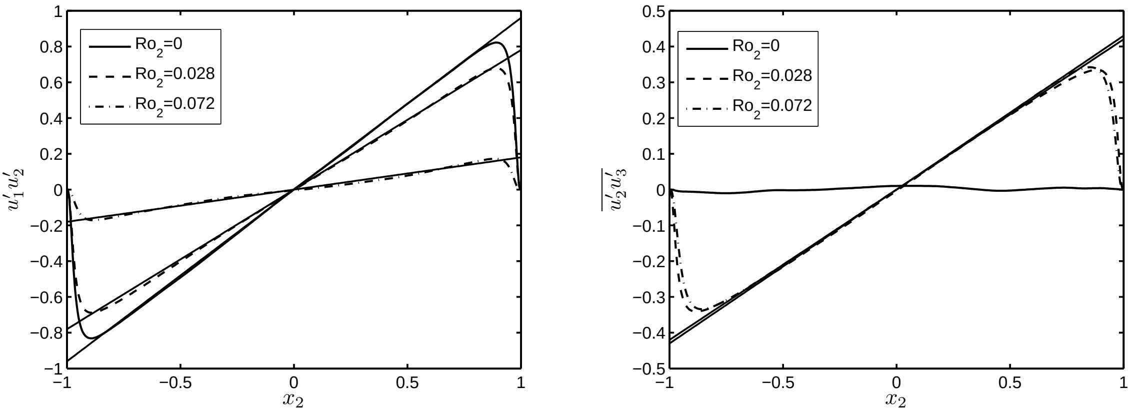

Figure 5.2: Distribution of the shear stresses in the channel and the linear approximation of them in the core region at $Re_{\tau 0} = 360$ for different rotation rates.

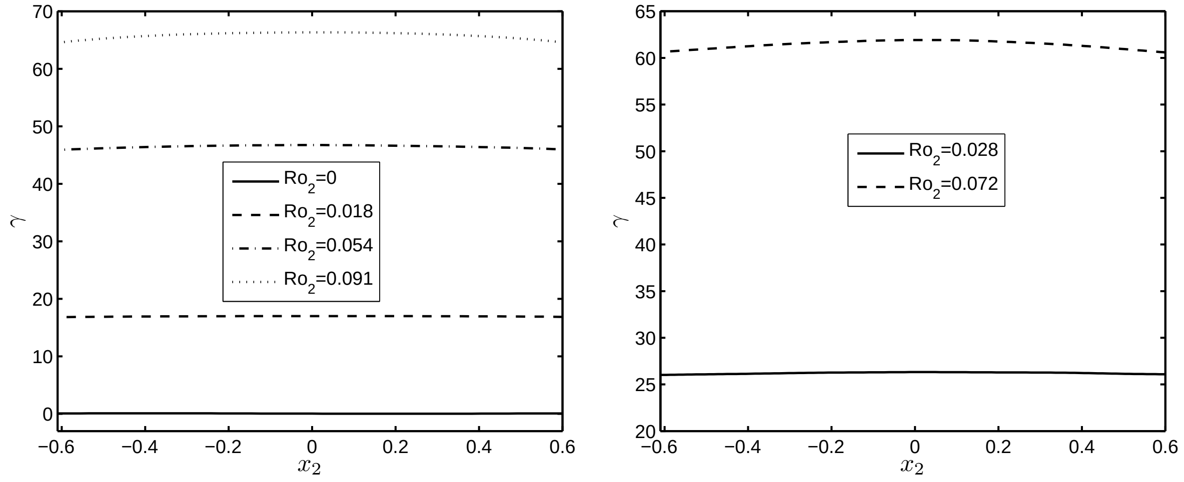

Figure 5.3: Direction of the bulk flow in the core region with respect to the streamwise direction for $Re_{\tau 0} = 180$ (left) and $Re_{\tau 0} = 360$ (right) .

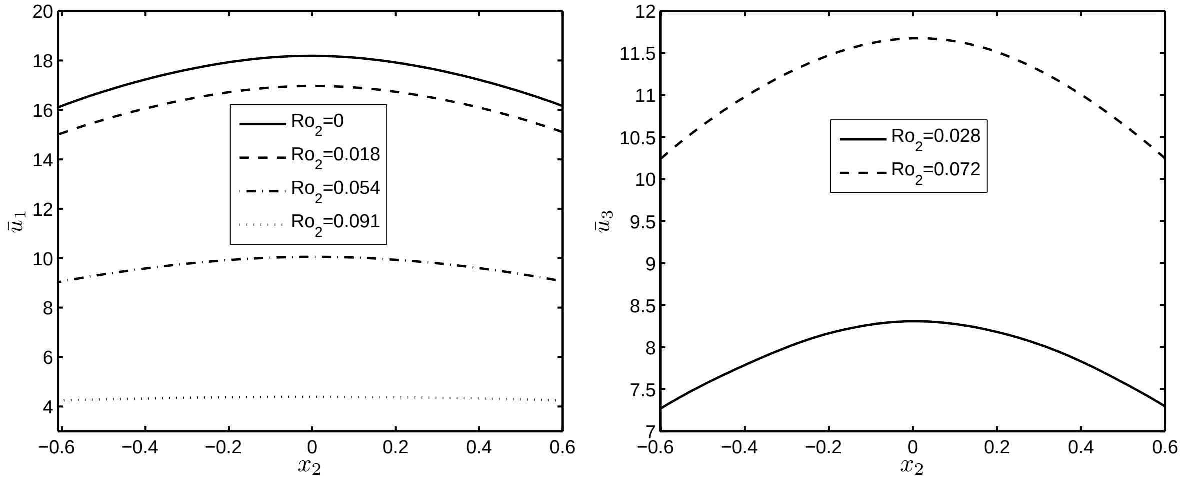

Figure 5.4: Mean velocity distribution in the core region in the streamwise at $Re_{\tau 0} = 180$ (left) and in the spanwise at $Re_{\tau 0} = 360$ (right) .

5.6 Summary and Conclusion

In this chapter the Lie symmetry approach has been applied to the reduced RANS equations (equations 5.17), which describe a turbulent channel flow at very high Reynolds number ($Re \to \infty$) rotating about wall-normal axes. Although generally (except for $Re \to \infty$) the viscous effects can not be neglected even in the core region of the channel, the same solution structures (linear distribution the shear stresses and a constant distribution for the angle of the bulk flow in the core region of the channel) can be observed also at relatively low Reynolds numbers. It may be deduced that contrary to the mean velocities in the streamwise and the spanwise directions, the shear stresses and the angle of the bulk flow are not so sensitive to the viscous effects in the core region of the channel. The main goal of applying the current Lie group analysis was to find self similar (invariant) solutions for the the given system of differential equations and use them to fix the unclosed terms. However a very large solution space with an arbitrariness in the symmetry structures has been obtained from the Lie symmetry analysis. Therefore a unique solution for the system can not be constructed and consequently the consistency check of the solution can not be done. Only the structure of the solutions for the shear stresses and the mean velocities (linear profiles for the stresses and constant distributions for the mean velocities) have been achieved, which are trivial at very high Reynolds numbers ($Re \to \infty$). It may be more reasonable to apply the Lie symmetry method to a system of differential equations that at least has fewer unclosed terms. The two-point correlation (or in general multi-point correlation) equation could be a good alternative, because they include fewer unclosed terms. However, they are considerably more complicated compared to the one-point correlation equation (RANS equations) and this will be the topic of futur research

6 RANS Modeling

6.1 Introduction

As mentioned in the first chapter the DNS of the turbulent flows is still limited to the relatively low Reynolds numbers and simple geometries. Since most of the turbulent flows encountered in practical configurations, and particularly in aerospace applications are characterized by very high values of the Reynolds number, the direct numerical simulation of turbulent flow remains out of reach from the capabilities of actual supercomputers. So it has clearly appeared necessary to develop some specific methods to decrease the costs associated with the simulation of turbulent flows. One approach is to rely on a statistical description of the turbulent flow. In this case, the involved scale separation operator thus relies on an averaging procedure. In practice, all the turbulent motion of the flow is then unresolved and has to be described by a mathematical model. Due to this definition, the cost of the simulations is significantly reduced in comparison with DNS, thus leading to some simulations which can be easily performed on usual computers. However, since the resolved fields is limited to a statistical description of the flow, the intermittency of the turbulent phenomenon can not be captured by such simulations, and highly unsteady flow phenomena can not be accurately described. On the other hand, and because of their affordable computational cost, RANS approaches are still the most commonly used for industrial applications. The main aim of this chapter is to study in what extent a relatively simple two-equation RANS model is able to predict the turbulent channel flow with wall-normal rotation.

6.2 The Closure Problem

As shown in chapter 2 for a general statistically three-dimensional flow, there are four independent equations governing the mean velocity field; namely three components of the Reynolds equations together with the mean continuity equation. However these four equations contain more than four unknowns. In addition to $\overline{u}$ and $\overline{p}$, there are also the Reynolds stresses to be determined. This is a manifestation of the closure problem. In general, the evolution equations (obtained from the Navier-stokes equations) for a set of statistics contain additional statistics to those in the set considered. As a consequence, in the absence of separate information to determine the additional statistics, the set of equations is under-determined and therefore cannot be solved. Such a set of equations with more unknowns than equations is said to be unclosed. The Reynolds equations are unclosed: they cannot be solved unless the Reynolds stresses are somehow determined.

6.3 Eddy Viscosity Concept

We now introduce some closure relation of the averaged equations at the level of the mean-flow equations: the Reynolds stresses are expressed linearly in terms of the mean velocity gradient and an eddy viscosity. If it is supposed that turbulence is created by a transfer of kinetic energy from the mean flow to turbulent scales, it is reasonable to assume that the Reynolds stresses will depend only on the mean velocity gradient. Also, with respect to the mean flow, they play a role similar to viscous stresses in the laminar case. If a mean strain is present, the eddy-viscosity concept retains a proportionality of the anisotropic part of Reynolds stress with the anisotropic part of the mean rate of strain:

$$\overline{u_i'u_j'} = \frac{2}{3}k\delta_{ij} - \nu_T\left(\frac{\partial \overline{u_i}}{\partial x_j} + \frac{\partial \overline{u_j}}{\partial x_i}\right), \tag{6.1}$$

where ν_T is the turbulent viscosity. The turbulent viscosity assumption provides a convenient closure to the Reynolds equation, which then have the same form as the Navier-Stokes equations. Unfortunately for many flows the accuracy of the hypothesis is not convincing. If the turbulent-viscosity hypotheses is accepted as an equitable approximation, all that remains is to determine an appropriate specification of the turbulent viscosity. This can be written as the product of a velocity scale a length scale:

$$\nu_T = u^* l^* \tag{6.2}$$

and the task of specifying ν_T is generally approached through specifications of u^* and l^*. In two-equation models, the $k-\epsilon$ model u^* and l^* are related to k and ϵ, for which modeled transport equations are solved.

6.4 The $k-\epsilon$ Model

It is well known that most the popular two-equation model is the $k-\epsilon$ model. The first developments based on this model were those of Chou (1945), Davidov (1961) and Harlaw & Nakayama (1968). The central paper however, is that by Jones & Launder (1972) that, in the turbulence modeling community, has nearly reached the status of the Boussineq and Reynolds paper. That is, the model is so well known as standard $k-\epsilon$ model. The standard $k-\epsilon$ belongs to the class of two-equation models, in which model transport equations are solved for two turbulence quantities. From these two quantities can be formed a length scale ($l^* = k^{3/2}/\epsilon$) and a timescale ($\tau = k/\epsilon$) which are needed to determine the eddy viscosity. The standard $k-\epsilon$ is as follows.

Kinematic Eddy Viscosity:

$$\nu_T = C_\mu \frac{k^2}{\epsilon} \quad , \tag{6.3}$$

Turbulent Kinematic Energy:

$$\frac{\partial k}{\partial t}+\bar{u}_j\frac{\partial k}{\partial x_j}=\frac{\partial}{\partial x_j}\left[\left(\nu+\frac{\nu_T}{\sigma_k}\right)\frac{\partial k}{\partial x_j}\right]+\nu_T\left(\frac{\partial\overline{u}_i}{\partial x_j}+\frac{\partial\overline{u}_j}{\partial x_i}\right)\frac{\partial\overline{u}_i}{\partial x_j}-\epsilon \quad , \tag{6.4}$$

Dissipation Rate:

$$\frac{\partial \epsilon}{\partial t}+\bar{u}_j\frac{\partial \epsilon}{\partial x_j}=\frac{\partial}{\partial x_j}\left[\left(\nu+\frac{\nu_T}{\sigma_\epsilon}\right)\frac{\partial \epsilon}{\partial x_j}\right]+C_{\epsilon_1}\frac{\epsilon}{k}\nu_T\left(\frac{\partial\overline{u}_i}{\partial x_j}+\frac{\partial\overline{u}_j}{\partial x_i}\right)\frac{\partial\overline{u}_i}{\partial x_j}-C_{\epsilon_2}\frac{\epsilon^2}{k} \quad , \tag{6.5}$$

Closure Coefficients :

$$C_{\epsilon_1}=1.44, \qquad C_{\epsilon_2}=1.92, \qquad C_\mu=0.09, \qquad \sigma_k=1.0, \qquad \sigma_\epsilon=1.3 \quad . \tag{6.6}$$

6.4.1 Low-Reynolds-Number Effects

The standard $k-\epsilon$ model and generally two-equations turbulence models without damping functions are restricted to high Reynolds number flows. In these models there is no term which concerns the low-Reynolds-number effects. Therefore most of them fail to predict the sharp peak in turbulence kinetic energy close to the surface for pipe and channel flow as an example for wall bounded shear flows. Furthermore they are mostly not able to predict a realistic value of the additive constant in the law of the wall and require modifications in order to do so. It should here be noted that there are applications for which viscous effects must be accurately represented.
Many researchers have tried to improve the standard $k-\epsilon$ model or other two equation models by implementing the viscous effects in the model. All have achieved some degree of asymptotic consistency. Jones & Launder (1972) were the first to propose viscous modifications for the $k-\epsilon$ model. Other proposals have been made by Launder & Sharma (1974), Chien (1982) and Durbin (1995) to name only a few. For steady, incompressible boundary layers, all of these models can be written compactly as follows:

$$\bar{u}_j\frac{\partial k}{\partial x_j}=\frac{\partial}{\partial x_j}\left[\left(\nu+\frac{\nu_T}{\sigma_k}\right)\frac{\partial k}{\partial x_j}\right]+\nu_T\left(\frac{\partial\overline{u}_i}{\partial x_j}+\frac{\partial\overline{u}_j}{\partial x_i}\right)\frac{\partial\overline{u}_i}{\partial x_j}-\epsilon, \tag{6.7}$$

$$\bar{u}_j\frac{\partial \tilde{\epsilon}}{\partial x_j}=\frac{\partial}{\partial x_j}\left[\left(\nu+\frac{\nu_T}{\sigma_\epsilon}\right)\frac{\partial \tilde{\epsilon}}{\partial x_j}\right]+C_{\epsilon_1}f_1\frac{\tilde{\epsilon}}{k}\nu_T\left(\frac{\partial\overline{u}_i}{\partial x_j}+\frac{\partial\overline{u}_j}{\partial x_i}\right)\frac{\partial\overline{u}_i}{\partial x_j}-C_{\epsilon_2}f_2\frac{\tilde{\epsilon}^2}{k}+E, \tag{6.8}$$

where the dissipation, ϵ, is related to the quantity $\tilde{\epsilon}$ by

$$\epsilon=\epsilon_0+\tilde{\epsilon}. \tag{6.9}$$

The quantity ϵ_0 is the value of ϵ at the wall ($x_2 = 0$), and is defined differently for each model. The eddy viscosity is now defined as below:

$$\nu_T = C_\mu f_\mu \frac{k^2}{\tilde{\epsilon}}. \tag{6.10}$$

The equations above contain five empirical damping functions, f_1, f_2, f_μ, ϵ_0 and E which are different for each model.
The model which is used for the present study is the model proposed by (Chien 1982). The damping function and modified coefficient in the model are as below:

$$f_\mu = 1 - e^{-0.0115 x_2^+}, \qquad f_1 = 1, \qquad f_2 = 1 - 0.22 e^{-\frac{Re_T^2}{36}}, \tag{6.11}$$

$$\epsilon_0 = 2\nu \frac{k}{x_2^2}, \qquad E = -2\nu \frac{\tilde{\epsilon}}{x_2^2} e^{-x_2^+/2}, \tag{6.12}$$

$$C_{\epsilon 1} = 1.35, \qquad C_{\epsilon_2} = 1.8, \qquad C_\mu = 0.09, \qquad \sigma_k = 1.0, \qquad \sigma_\epsilon = 1.3, \tag{6.13}$$

where Re_T and x_2^+ are defined as below:

$$Re_T = \frac{k^2}{\tilde{\epsilon}\nu}, \quad x_2^+ = \frac{u_\tau x_2}{\nu}.$$

6.4.2 Rotation Effects

As mentioned before (chapter 2) the result of the system rotation is the appearance of the Coriolis and centrifugal forces in the Navier-Stokes and also in the RANS equations. However, the centrifugal force can be absorbed into the pressure term. Further, in the rotating cases the Reynolds stress transport equation contains the exact rotational redistribution term (Equation $(4 - 10)$). This term disappears in the transport equation for the turbulent kinetic energy and therefore there is no term which concerns the rotation in the standard $k - \epsilon$ turbulence model. This leads to a problem in predicting of rotating flows, (Speziale 1991). The Coriolis force however acts perpendicular to the velocity vector and probably has no direct effect on the turbulent kinetic energy budget, but redistributes the stresses among components and modifies the turbulence production, implying that in principle the ϵ equation should be modified to account for rotation effects. Bardina & Rogallo (1985) and Shimomura (1993) have proposed such modifications.

6.5 Numerical Method

Partial differential equations occur in almost any branch of science and engineering. Exact analytical solutions could be obtained only for very few simple cases. In most cases one has to employ some numerical methods, the finite difference, finite volume and finite element methods are the most popular. They are applicable to linear as well as nonlinear partial differential equations and the methods can produce results of arbitrary high accuracy, by refining the grid size. Further, the methods are also applicable to higher dimensions.
Computational methods like finite difference, finite volume, finite element or their variants that are most frequently used in CFD all begin with subdividing the domain of integration into a large but finite number of small elements. The elements are so small that the flow quantities like pressure, velocity or density and other may be assumed to be constant over the element, equal to the value at the center of the element. Thus a finite set of points is associated with a given domain. Instead of the centroid, for example, the vertices of the elements may also be considered. The concept of approximating the flow quantities by a discrete model that is composed of a set of piecewise continuous which are defined over a finite number of elements is the basis of the finite element (volume) method.

6.5.1 Properties of Numerical Solution Methods

The numerical methods should have certain mathematical properties. Mostly it is not possible to investigate all of them. In the following most important properties will be discussed very briefly. For further information seeFerziger & Peric (2002) andSchaefer (1999).

6.5.1.1 Consistency

The difference between the discretized equation and the exact one is called truncation error. The numerical solution method is consistent if the truncation error should tend to zero as the mesh size tends to zero.

6.5.1.2 Stability

A numerical solution method is called stable if it does not increase the errors that appear during the numerical solution process. For time dependent problems, stability guarantees that the method produces a bounded solution whenever the solution of the exact equation is bounded. For iterative methods, a stable method is one which does not diverge.The stability of numerical methods is however difficult to investigate, especially in presence of boundaries and non-linear terms. Therefor normally one investigates the stability of linear problem without boundary and then applies the results to the more complex cases. However, in complicated non-linear cases there are only a few stability results and hence one has to rely only on the experience.

6.5.1.3 Convergence

A numerical method is convergent if the solution of the discretized equations tends to the exact solution of the differential equation as the grid spacing tends to zero. The convergence of a numerical method is mostly checked by repeating the simulation on a series of successively refined grids. If the method is stable and consistent, we usually find that the solution converges to a grid-independent solution. For sufficiently small grid sizes, the rate of convergence is governed by the order of principal truncation error component. This allows us to estimate the error in the solution.

6.5.1.4 Conservation

Numerical scheme is conservative if it on both local and global basis respects the conservation laws. Non-conservative methods can also made conservative by taking care of the choice of approximation.

Non-conservative schemes can produce artificial sources and sinks, changing the balance both locally and globally. However, non-conservative schemes could also be consistent and stable and therefore lead to proper solutions at very fine grids. The errors due to non-conservation are in most cases appreciable only on relatively coarse grids. The problem is that it is difficult to know on which grid are these errors small enough. Conservative schemes are therefore preferred.

6.6 Finite Volume Methods

In the finite volume method the generic conservation equation for a quantity ϕ is considered and is also assumed that the velocity field and all fluid properties are known. The finite volume method has been applied to the integral form of the conservation equation in a stationary form as the starting point:

$$\int_s \rho\phi v.nds = \int_s \Gamma grad\phi.nds + \int_\Omega q_\phi d\Omega, \tag{6.14}$$

where Ω is the computational domain and s is the boundary of the domain.
The computational domain is divided into a finite number of non-overlapping control volumes (CV) such that there is one control volume surrounding each grid point. There are two approaches to define the CVs. The first one is to define the control volumes by a suitable grid and put the computational nodes to the center of control volumes. The second one is to define the nodal locations first and construct CVs around them, so that the CV faces are midway between nodes. It should be noted that for uniform grids (uniform control volume size) both approaches are identical.

The integral conservation equation (6.14) applies to each CV, as well as to the solution domain entirely. If we sum equations for all CVs, we obtain the global conservation equation, since surface integrals over inner CV faces cancel out. Thus global conservation laws are satisfied in the method and this provides one of its principal advantages. To obtain an algebraic equation for a particular CV, the surface and volume integrals need be approximated.

6.6.1 Approximation of Surface Integrals

In figures 6.1 a typical 2D Cartesian control volumes is indicated together with the notation we will use. The control volume surface consists of four plane faces, denoted by lower-case letters corresponding to their direction (e, w, n, s, t, and b) with respect to the central node (P). The 2D case can be regarded as a special case of the 3D one in which the dependent variables are independent of z. So the extension to 3D problems is straightforward. The net flux through the CV boundary is the sum of integrals over the four faces:

$$\int_s f ds = \sum_s \int_{s_k} f ds, \tag{6.15}$$

where f is the component of the convective $(\rho\phi v.n)$ or diffusive $(\Gamma grad\phi.n)$ flux vector in the direction normal to CV face. Since the velocity field and the fluid properties are assumed known, the only unknown variable is ϕ. If the velocity field is not known, we have a more complex problem due to the existence of non-linear coupled equations.

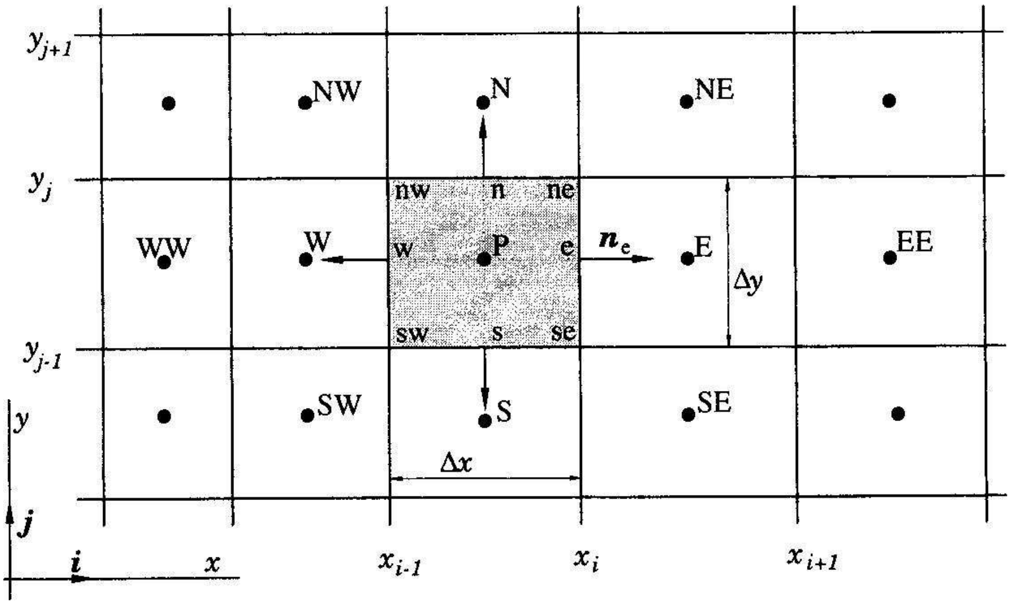

Figure 6.1: A typical CV and the notation used for a Cartesian 2D grid

In the following, only a typical CV face, the one labeled 'e' in figure 6.1 will be considered; analogous expressions can be derived for all faces.

To calculate the surface integral in (6.15) exactly, the integrand has to be approximated on the surface S_e using the nodal value of ϕ which is known. This can be done easily by using two levels of approximation:

- the integral is approximated in terms of the variable values at one or more positions on the cell face,
- the cell-face values are approximated in terms of the nodal values.

The simplest approximation to the integral is the midpoint rule: the integral is approximated as a product of the integrand at the cell-face center and the cell-face area:

$$F_e = \int_s f ds = \overline{f_e} S_e \approx f_e S_e. \tag{6.16}$$

This approximation of the integral - provided the value of f at location 'e' is known - is of second-order accuracy. Since the value of f is not available at the cell face center 'e', it has to be obtained by interpolation. In order to keep the second-order accuracy of the midpoint rule approximation of the surface integral, the value off_e has to be computed with at least second-order accuracy. There are another second-order approximation of the surface integral in 2D and also higher-order approximations of the surface integrals which are not described here. Further information can be obtained from Ferziger & Peric (2002) and Schaefer (1999).

6.6.2 Approximation of Volume Integrals

Some terms in the transport equations need to be integrated over the volume of a CV. The simplest second-order accurate approximation is to replace the volume integral by the product of the mean value of the integrand and the CV volume and approximate the former as the value at the CV center:

$$Q_p = \int_\Omega q d\Omega = \overline{q} \Delta\Omega \approx q_p \Delta\Omega \tag{6.17}$$

where q_P stands for the value of q at the CV center. This quantity is easily calculated; since all variables are available at node P, no interpolation is necessary. The above approximation becomes exact if q is either constant or varies linearly within the CV; otherwise, it contains a second-order error. For further information about the approximations of higher orders see Ferziger & Peric (2002) and Schaefer (1999).

6.6.3 Interpolation and Differentiation Practices

For approximations of the integrals the values of variables at locations other than computational nodes (CV centers) are needed. The integrand, denoted in the previous sections by f, involves the $(f^c = \rho\phi v.n)$ for the convective flux and $f^d = \Gamma grad\phi.\boldsymbol{n}$ for the diffusive flux. We assume that the velocity field and the fluid properties ρ

and $\Gamma$are known at all locations. To calculate the convective and diffusive fluxes, the value of ϕ and its gradient normal to the cell face at one or more locations on the CV surface are needed. They have to be expressed in terms of the nodal values by interpolation. Numerous possibilities are available. In the following we mention a few that are most commonly used. For more informations see Ferziger & Peric (2002) and Schaefer (1999).

6.6.3.1 Upwind Interpolation (UDS)

The easiest Upwind method is to approximating ϕ_e by its value at the node upstream of 'e' which is equivalent to using a backward- or forward-difference approximation for the first derivative (depending on the flow direction), hence the name upwind differencing scheme (UDS) for this approximation. In UDS, ϕ_e is approximated as:

$$\phi_e = \begin{cases} \phi_P & (v.n)_e > 0, \\ \phi_E & (v.n)_e < 0. \end{cases} \tag{6.18}$$

This is the only approximation that unconditionally satisfies the boundedness criterion i.e. it is always stable. However, it achieves this by being numerically diffusive. This will be shown again below. Taylor series expansion about P gives (for Cartesian grid and $(v.n)_e > 0$)

$$\phi_e = \phi_p + (x_e - x_p)\left(\frac{\partial \phi}{\partial x}\right)_p + \frac{(x_e - x_p)^2}{2}\left(\frac{\partial^2 \phi}{\partial x^2}\right)_p + H, \tag{6.19}$$

where H denotes higher-order terms. The UDS approximation retains only the first term on the right-hand side, so it is a first-order scheme. Its leading truncation error term is diffusive i.e. it resembles a diffusive flux:

$$f_e^d = \Gamma_e\left(\frac{\partial \phi}{\partial x}\right)_p . \tag{6.20}$$

The coefficient of numerical, artificial, or false diffusion is $\Gamma_e^{num} = (\rho u)_e \Delta x/2$. This numerical diffusion is increased in multidimensional problems. If the flow is oblique to the grid; the truncation error then produces diffusion in the direction normal to the flow as well as in the streamwise direction, a particularly serious type of error. Peaks or rapid variations in the variables could be the case. Since the rate of error reduction is only first order, very fine grids are required to obtain accurate solutions.

6.6.3.2 Linear Interpolation (CDS)

Another approximation method for the value at CV-face center is linear interpolation between the two nearest nodes. At location 'e' on a Cartesian grid we have :

$$\phi_e = \phi_E \lambda_e + \phi(1 - \lambda_e), \tag{6.21}$$

where the linear interpolation factor λ_e is defined as:

$$\lambda_e = \frac{x_e - x_P}{x_E - x_P}. \tag{6.22}$$

Equation (6.23) is second-order accurate as can be shown by using the Taylor series expansion of $\phi_E$about the point $x_P$to eliminate the first derivative in (6.21). The result is:

$$\phi_e = \phi_E \lambda_e + \phi_P(1 - \lambda_e) - \frac{(x_e - x_P)(x_E - x_e)}{2} \left(\frac{\partial^2 \phi}{\partial x^2} \right)_p + H \quad . \tag{6.23}$$

The leading truncation error term is proportional to the square of the grid spacing, on uniform or non-uniform grids. As with all approximations of order higher than one, this scheme may produce oscillatory solutions and leads to an instability. This is the simplest second-order scheme and is the one most widely used.

6.6.4 Implementation of Boundary Conditions

For each control volume (CV), one algebraic equation can be written according to the approximations of integrals of equation (6.14) at the cell surfaces . Volume integrals can be treated in the same way for every control volume, however, fluxes through CV faces coinciding with the domain boundary require special treatment. These boundary fluxes must either be known, or be expressed as a combination of interior values and boundary data which are already known. They do not provide additional equations, therefore they should not introduce additional unknowns. Since there are no nodes outside the boundary, these approximations must be based on one-sided differences or extrapolations. Normally, convective fluxes are defined at the inflow boundary. Convective fluxes are zero at impermeable walls and symmetry planes and are mostly assumed to be independent of the coordinate normal to an outflow boundary. In this case, upwind approximations can be used. Diffusive fluxes are sometimes specified at a wall or boundary values of variables are prescribed. In such a case the diffusive fluxes are calculated using one-sided approximations for normal gradients .

6.7 Simulations

The simulations have been performed for Reynolds numbers ($\mathrm{Re}_{\tau_0} = 180$ and 360) based on the friction velocity in the non-rotating channel flow at different rotation rates. It should also be noted that the simulations have performed for small rotation rates, at which the flow is fully turbulent. The box size (computation domain) used for all simulations is $4\pi \times 2 \times 2\pi$ with $25 \times 128 \times 15$ grid points in the x_1, x_2 and x_3 directions respectively. Similar to the DNS, non-slip condition at the walls has been used and periodic boundary conditions in the streamwise and the spanwise directions have been employed. The residuals were set to 10^{-5} for all simulations and the linear interpolation (CDS) method was used. The following grid resolutions were used:

$\mathbf{Re}_{\tau_0} = \mathbf{180}$

The uniform grid resolution in the streamwise and the spanwise directions used for all simulation is given as follows:

$$\Delta x_1^+ \approx 94 \quad \Delta x_3^+ \approx 78.$$

The resolution in the wall-normal (x_2) direction is fine near the walls and becomes coarser away from the wall. The variation from the finest to the coarsest cells using linear distributation in this direction is as below:

$$\Delta x_2^+ \approx 1.5 - 3.$$

$\mathbf{Re}_{\tau_0} = \mathbf{360}$

The uniform grid resolution in the streamwise and the spanwise directions used for all simulation is given as follows:

$$\Delta x_1^+ \approx 188 \quad \Delta x_3^+ \approx 156.$$

The variation of the grid resolution in x_2 direction is as below:

$$\Delta x_2^+ \approx 2.8 - 5.7.$$

It should be mentioned that fully turbulent field in non-rotating case has been used as initial condition for the rotating cases. All computations have been conducted with in-house computer code FASTEST based on a finite volume numerical method for solving RANS equations on block-structured meshes.

6.8 Results

The results obtained from the Chien model have been compared to the DNS data (Figures 6.2-6.4). The good agreement between them indicates that the model is capable of predicting the turbulent channel flow with wall-normal rotation.
It should also be noted that the results coming in the following have been presented in Mehdizadeh, Oberlack & Hosseinzadeh (2009)

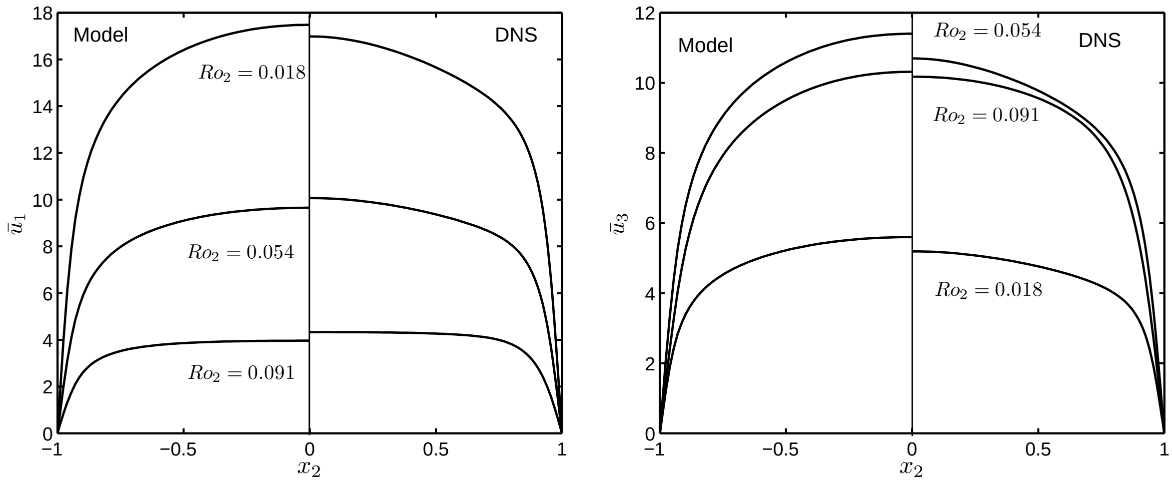

Figure 6.2: Comparison of the results obtained from the Chien model for the streamwise (left) and the spanwise (right) mean velocities with DNS at different rotation rates for $Re_{\tau_0} = 180$.

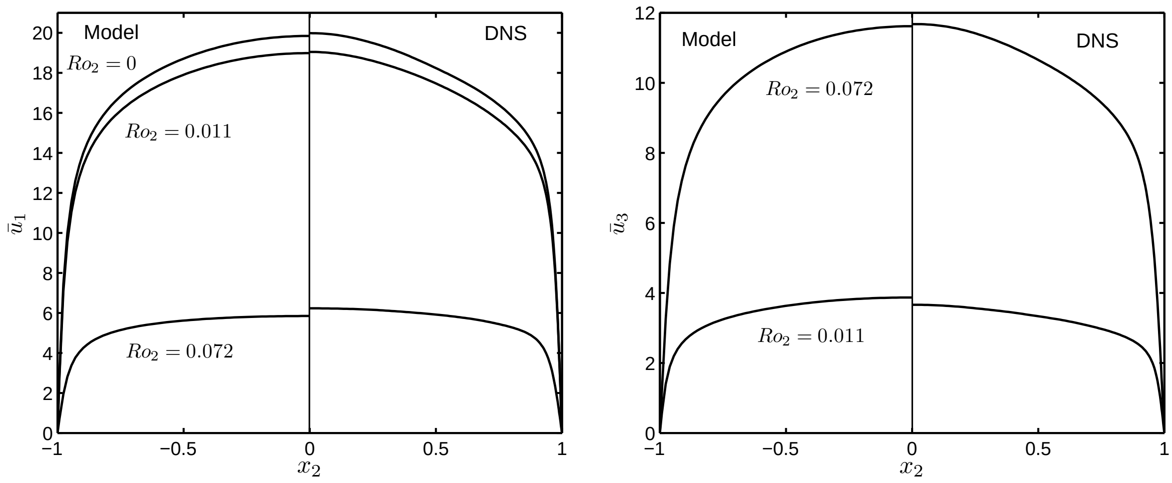

Figure 6.3: Comparison of the results obtained from the Chien model for the streamwise (left) and the spanwise (right) mean velocities with DNS at different rotation rates for $Re_{\tau_0} = 360$.

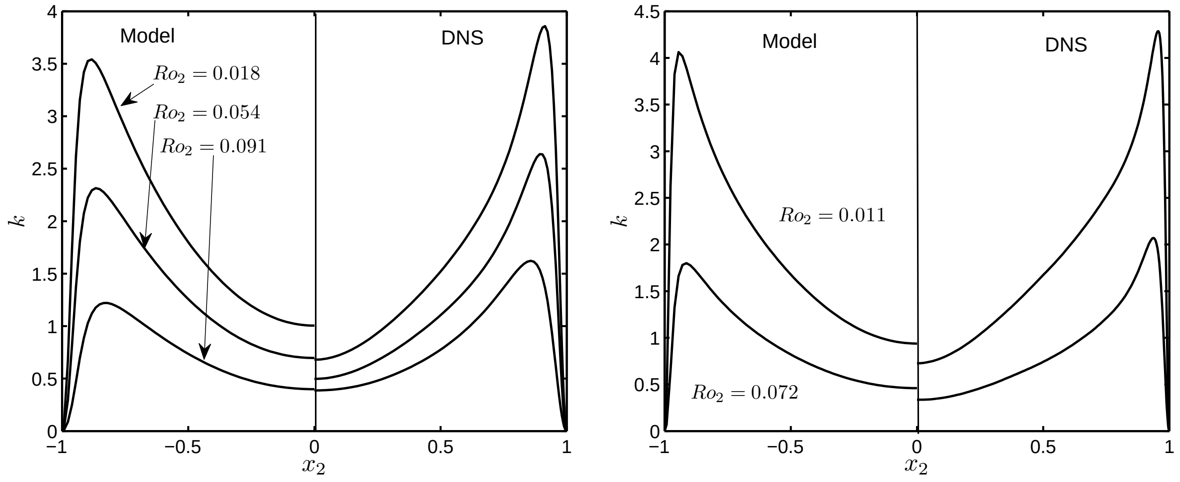

Figure 6.4: Comparison of the results obtained from the Chien model for the turbulent kinetic energy with DNS for $Re_{\tau_0} = 180$ (left) and $Re_{\tau_0} = 360$ (right) at different rotation rates.

6.9 Summary and Conclusion

In this chapter the ability of relatively simple turbulence model to predict the turbulent wall-normal rotating channel flow has been studied. In contrast to the turbulent channel flow rotating about the streamwise or the spanwise axes which are very difficult to predict using simple low-Reynolds-number model, the present flow could be predicted by a relatively simple RANS model. It is possible that, since the Coriolis terms appear directly in the mean flow equations in the streamwise and the spanwise directions and the Reynolds stress field is almost not affected by the rotation, the model was able to predict the flow. Similar to the DNS results the results obtained in this chapter also show that the turbulent channel flow with wall-normal rotation can be regarded as a two-dimensional turbulent channel flow. It should be noted that the model was able to predict the flow only in the fully turbulent region (at small rotation rates). Predicting the flow in the quasi-laminar region resulting from high rotation number effect requires more advanced turbulence models.

7 Summary and Discussions

In the present thesis the effects of the wall-normal rotation on laminar and turbulent channel flows have been investigated by means of numerical and analytical approaches. In the laminar case the Navier-Stokes equations can be solved analytically. It was found that the laminar plane channel flow is very sensitive to the wall-normal rotation. Even a rather small rotation rate can induce a relatively strong secondary motion in the spanwise direction making the flow three-dimensional. Further, it has been established that at very high rotation rates, where the Rossby number tends to zero the flow indicates a similar behavior compared to the laminar Ekman layer or in the other words there are certain commonalities between this flow at very high rotation rates and the laminar Ekman layer.

In the turbulent case however, there is no analytical solution of the RANS equations. So in order to establish the effects of the wall-normal rotation on the turbulent plane channel flow a numerical approach i.e. DNS has been used. Direct numerical simulations have been performed for wide ranges of rotation rates at two different Reynolds numbers based on the friction velocity in the non-rotating case i.e. ($Re_{\tau_0} = 180, 360$). It was found that similar to the laminar case turbulent plane channel flow is also very sensitive to the wall-normal rotation and is highly affected even by a small rotation rate. Wall-normal rotation induces a mean spanwise velocity and as a result all six components of Reynolds stress tensor become non-zero. However, the wall-normal rotation affects the Reynolds stress field only slightly and thus the flatness factor and the structure parameter are only slightly deviated from the ones of non-rotating case. This may imply that a turbulent wall-normal rotating channel flow can be regarded as a two-dimensional turbulent plane channel flow. It is interesting to note that in both cases (laminar and turbulent) the streamwise and the spanwise mean velocities indicate similar behaviors against the rotation. Increase in the rotation rate causes the turbulence to be damped and leads the flow to the quasi-laminar region. In this region the Reynolds number is below the corresponding critical Reynolds number and the inflection points are visible in the velocity profiles. A result of the inflection points in the mean velocity profiles is elongated coherent structures extended along the channel. By further increasing of the rotation rate the turbulence is completely damped or in other words the flow is completely laminarized and reaches a fully laminar steady state for which there is the above mentioned analytical solution. It should be noted that the rotation rate at which the changing of the flow state occurs is obviously dependent on the Reynolds number (Re_{τ_0}). The higher the Reynolds number, the higher rotation rate is needed to leading to the quasi-laminar state. The same is also true for the rotation rate at which the flow is completely laminarized.

Furthermore, the Lie-symmetry approach has been applied to the RANS equations describing a turbulent wall-normal rotating channel flow at very high Reynolds number. The obtained results only indicate a constant distribution of the flow direction in the core region of the channel which may imply again that the turbulent channel flow with wall-normal rotation could be approximated by a turbulent channel flow without rotation. Because of the existence of the unclosed terms in the RANS equation the Lie-symmetry approach was not able to provide further information about statistical quantities of the flow.

Finally the ability of a simple turbulence model to predict the turbulent wall-normal rotating channel flow has been investigated for very small rotation rates. Contrary to the turbulent channel flow rotating about the streamwise or the spanwise axes which can not be predicted by simple two equations turbulence models, the Chien model was able to predict the flow. This is very probably due to the fact that the Coriolis terms enter directly into the mean flow equations and immediately affect the mean velocities. Hence one can deduce that every turbulence model which can predict the non-rotating channel flow could also predict the present flow at small rotation numbers. At higher rotation rates the process includes relaminarization effects which are very challenging and more advanced models either in RANS or in LES are required to capture these effects.

8 Bibliography

ABE, H., KAWAMURA, H., MATSUO, Y. (2001): Direct numerical simulation of a fully developed turbulent channel flow with respect to the Reynolds number dependence. *Journal of Fluids Engineering 123(2)*, 382–393.

BARDINA, F. J. H., D., ROGALLO, R. (1985): Effect of rotation on isotropic turbulence. *J.Fluid Mech. 154*, 321–336.

BLUMAN, G., ANCO, S. (2002): *Symmetry and integration methods for differential equations*, Bd. 154 von *Applied mathematical sciences*. Springer-Verlag.

BLUMAN, G. W., KUMEI, S. (1996): *Symmetries and Differential Equations*. 2nd edn. Springer Verlag.

BROWN, R. A. (1974): *Analytical methods in planetary boundary-layer modeling*. Wiley and Sons.

CALDWELL, D., VAN ATTA, C. W. (1970): Characteristics of Ekman boundary layer instabilities. *J.Fluid Mech. 44*, 79–95.

CHEVIAKOV, A. F. (2007): GeM software package for computation of symmetries and conservation laws of differential equations. *Comp. Phys. Comm. 176* , 48–61.

CHIEN, K. Y. (1982): Predictions of channel and boundary-layer flows with a loe-Reynolds-number turbulence model. *AIAA Journal 20, No. 20*, 33–38.

CHOU, P. Y. (1945): On the velocity correlations and the solution of the equations of turbulence fluctuation. *Quart. Appl. Math. 3*, 38.

COLEMAN, G., FERZIGER, J., SPALART, P. (1990): A numerical study of the turbulent Ekman layer. *J.Fluid Mech. 213*, 313–348.

DAVIDOV, B. I. (1961): On the statstical dynamics of an incompressible fluid. *Doklady Akademiya Nauk SSSR 136*, 47.

DEARDORFF, J. W. (1972): Numerical investigation of neutral and unstable planetary boundary layers. *J. Atmos. Sci 29*, 91–115.

DURBIN, P. (1995): Near wall turbulence modeling without damping functions. *Theoretical and Computational Fluid Dynamics 3, No. 1*, 1–13.

EKMAN, V. (1905): On the influence of the earths rotation on ocean-currents. *Ark. Mat. Ast. Fys 2 I-52*, 32.

ELSAMNI, O., KASAGI, N. (2001): The effects of system rotation with three orthogonal rotating axes on turbulent channel flow. *In proceeding of 7th internationalcongress on fluid dynamics and propulsion, Egypt* .

ETLING, D., BROWN, R. A. (1993): Roll vortices in the planetary boundary layer: A review. *Boundary-Layer Meteorology 65*, 215–248.

FALLER, A. J. (1963): An experimental study of the instability of the laminar Ekman boundary layer. *J.Fluid Mech. 15*, 560–576.

FALLER, A. J. (1965): Large eddies in the atmospheric boundary layer and theit possible role in the formation of cloud rows. *J. Atmos. Sci 22*, 176–184.

FERZIGER, J. H., PERIC, M. (2002): *Computational methods for fluid dynamics*. 3nd edn. Springer Verlag.

FOIAS, C., MANLEY, O., ROSA, R., TEMAM, R. (2001): *Navier-Stokes equations and turbulence*, Bd. 83 von *Encyclopedia of mathematics and its application*. Cambridge University Press.

GREENSPAN, H. P. (1980): *The theory of rotating fluids*. Cambridge University Press.

GRUNDESTTAM, O., WALLIN, S., V. JOHANSSON, A. (2008): Direct simulations of rotating turbulent channel flow. *J.Fluid Mech. 598*, 177–199.

HARLAW, F. H., NAKAYAMA, P. I. (1968): Transport of turbulence energy decay rate. *Los Alamos Sci. Lab., University of California Report LA-3854* .

HICKEY, J.-P., KHUJADZE, G., OBERLACK, M. (2008): Hydrodynamic instabilities of a streamwise rotating Poiseuille flow: beyond eigenvalues. *Private communication* , 177–199.

HOFFMANN, N., BUSSE, F. (2001): Linear instability of Poiseuille-Couette-Ekman flows: Local results for flows between differentially rotating disks with throughflow. *Phys.Fluids. 13*, 2735–2738.

HOYAS, S., JIMÉNEZ, J. (2006): Scaling of the velocity fluctuations in turbulent channels up to Re_τ=2003. *Phys. Fluids 18*, 0011702.

JOHNSON, J., HALLEEN, R., LEZIUS, D. (1972): Effects of spanwise rotation on the structure of two-dimensional fully develpoed turbulent channel flow. *J.Fluid Mech. 56*, 533–557.

JOHNSTON, J., HALLEEN, R., LEZIUS, D. (1972): Effects of spanwise rotation on the structure of two-dimensional fully developed turbulent channel flow. *J. Fluid Mech. 56*, 533–557.

JONES, W. P., LAUNDER, B. E. (1972): The prediction of laminarization with a two-equation model of turbulence. *International Journal of Heat and Mass Transfer 15*, 301–314.

KASAGI, N., TOMITA, Y., KURODA, A. (1992): Direct numerical simulation of a passive scalar field in a turbulent channel flow. *Journal of heat transfer 114*, 598–606.

KIM, J. (1982): The effect of rotation on turbulence structure. *In proceeding of the fourth international symposium on turbulence shear flows,Karlsruhe,Germany* , 614–619.

KIM, J., MOIN, P., MOSER, R. (1987): Turbulence statistics in fully developed channel flow at low Reynolds number. *J. Fluid Mech. 177*, 133–165.

KRISTOFFERSEN, R., ANDERSSON, H. (1993): Direct simulations of low-Reynolds-number turbulent flow in a rotating channel. *J. Fluid Mech. 256*, 163–197.

KURODA, A., KASAGI, N., HIRATA, M. (1989): A direct numerical simulation of the fully developed turbulent channel flow at a very low Reynolds number. 3rd International Symposium on Computational Fluid Dynamics, Nagoya, Japan, 1174–1179.

LAMBALLAIS, E., ME'TAIS, O., LESIEUR, M. (1998): Spectral-dynamic model for large-eddy simulations of turbulent rotating channel flow. *Theor. Comp. Fluid Dyn. 12*, 146–177.

LAUNDER, B. E., SHARMA, B. I. (1974): Application of the energy dissipation model of turbulence to the calculation of flow near a spinning disk. *Letters in Heat and Mass Transfer 1, No. 2*, 131–138.

LE MONE, M. A. (1973): The structure and dynamics of horizontal rolls votices in the planetary boundary layer. *J. Atmos. Sci 30*, 1077–1091.

LI, B.-Y., LIU, N.-S., LU, X.-Y. (2006): Direct numerical simulation of wall-normal rotating channel flow with heat transfer. *International Journal of Heat and Mass Transfer 49*, 1162–1175.

LUNDBLADH, A., HENNINGSON, D., JOHANSON, A. (1992): An efficient spectral integration method for the solution of the Navier-Stokes equations. Techn. Ber., FFA-TN 1992-28, Aeronautical Research Institute of Sweden, Bromma.

MEHDIZADEH, A., OBERLACK, M., HOSSEINZADEH, A. (2009): DNS and Modeling of Turbulent Channel Flow with Wall-Normal Rotation. *In proceeding of the Sixth International Symposium on Turbulence Shear Flow Phenomena, Seoul, Korea* , 557–562.

MOIN, P., KIM, J. (1982): Numerical investigation of turbulent channel flow. *J.Fluid Mech. 118*, 341–377.

MOSER, R., KIM, J., MANSOUR, N. (1999): Direct numerical simulation of turbulent channel flow up to $Re_\tau = 560$. *Physics of Fluids 11*, 943–945.

NAKABAYASHI, K., KITOH, O. (1996): Low Reynolds number fully developed two-dimensional turbulent channel flow with system rotation. *J.Fluid Mech. 315*, 1–29.

OBERLACK, M. (2000): *Symmetrie, Invarianz und Selbstähnlichkeit in der Turbulenz*. Habilitation, Inst. f. Techn. Mechanik, RWTH Aachen.

OBERLACK, M. ., CABOT, W., ROGERS, M. (1998): Group analys,DNS and modelling of a turbulent channel flow with streamwise rotation. *Studing Turbulence Using Numerical Database-VII, Center for Turbulence Research, Stanford University/NASA Ames* , 221–242.

OBERLACK, M., CABOT, W., PETTERSSON REIF, B., WELLER, T. (2006): Group analysis, DNS and modelling of a turbulent channel flow with streamwise rotation. *J.Fluid Mech. 562*, 383–403.

OLIVER, P. J. (1993): *Applications of Lie Group to Differential Equations*. 2nd edn. Springer Verlag.

ORLANDI, P., FATICA, M. (1997): Direct Simulations of turbulent flow in a pipe rotating about its axis. *J. Fluid Mech. 343*, 43–72.

ORSZAG, S., PATTERSON JR., G. (1972): Numerical simulation of three-dimensional homogeneous isotropic turbulence. *Phys. Rev. Lett. 28*.

PEYRET, R. (2002): *Spectral methods for incompressible viscous flow*. Springer, New-York.

RECKTENWALD, I., WELLER, T., SCHROEDER, W., OBERLACK, M. . (2007): Comparison of direct numerical simulation and particle-image velocimetry data of turbulent channel flow rotating about the streamwise axis. *Phys.Fluids. 19*, 085114: 1–11.

ROTTA, J. (1972): *Turbulente Strömungen*. Teubner, Stuttgart.

SCHAEFER, M. (1999): *Numerik in Maschinenbau*. Springer Verlag.

SHIMOMURA, Y. (1993): Turbulence modeling suggested by system rotation. *Near-Wall Turbulence Flows* , 115–123.

SHINGAI, K., KAWAMURA, H. (2004): A study of turbulence structure and large-scale motion in the Ekman layer through direct numerical simulations. *JOURNAL OF TURBULENCE 5*, DOI:10.1088/1468–5248/5/1/013.

SPALART, P. R., COLEMAN, G. N., JOHNSTONE, R. (2008): Direct numerical simulation of the Ekman layer: A step in Reynolds number, and cautious support for a log law with a shifted origin. *Phys.Fluids. 20*, 101507.

SPEZIALE, C. G. (1991): Analytical methods for the development of Reynolds-stress closures in turbulence. *Annu. Rev. Fluid Mech. 23*, 107–157.

WOLLKIND, R., DIPRIMA, R. (1973): Effect of Coriolis force on the stability of plane Poiseuille flow. *Phys.Fluids. 16*, 2045–2051.

WU, H., KASAGI, N. (2004): Effects of arbitrary directional system rotation on turbulent channel flow. *Phys.Fluids. 16*, 979–990.

Appendix A

The obtained infinitesimals by applying Lie symmetry method to the RANS equations (5.17) describing a wall-normal rotating channel flow at very high Reynolds numbers.

$$\xi_{x_2} = {x_2}^2 C_1 + C_2\, x_2 + C_3$$

$$\eta_{\bar{u}_1} = \frac{\left(-2\,\Omega_2\,\bar{u}_1 x_2 + \tau_{23}\right) C_1 + 2\,\Omega\, U C_4 + C_5 - 2\,\Omega_2\, U C_2}{2\Omega_2}$$

$$\eta_{\bar{u}_3} = \frac{-2\bar{u}_3\Omega_2 x_2 - \tau_{12} + C_1 G x_2 + (G - 2\Omega_2\bar{u}_3)C_2 + (2\Omega_2\bar{u}_3 - G)C_4 - C_6}{2\Omega_2}$$

$$\eta_{\tau_{23}} = C_1\,\tau_{23} x_2 + x_2 C_5 + C_4\,\tau_{23} + C_8$$

$$\eta_{\tau_{12}} = \tau_{12} x_2 C_1 + \tau_{12} C_4 + C_6\, x_2 + C_7$$

$$\begin{aligned}\eta_{\tau_{13}} = \frac{1}{4\Omega_2}&[(G - 2\Omega_2\bar{u}_3)D_2(F_1)(x_2, \tau_{12}, \tau_{22} + P, \tau_{23}) + 2\bar{u}_1 D_4(F_1)(x_2, \tau_{12}, \tau_{22} + P, \tau_{23})\Omega + \\ &D_1(F_1)(x_2, \tau_{12}, \tau_{22}+P, \tau_{23}) + ((-4\tau_{13} + 4\bar{u}_3\bar{u}_1)\Omega_2 - 2G\bar{u}_1)C_2 + (-8\Omega_2\bar{u}_3\bar{u}_1 + 4G\bar{u}_1)C_4 + 2C_6\bar{u}_1 \\ &- 8\Omega_2\tau_{13} x_2 C_1]\end{aligned}$$

$$\begin{aligned}\eta_{\tau_{11}} = \frac{1}{2\Omega_2}&[2\eta_{\tau_{33}}\Omega_2 + (2\Omega_2\bar{u}_3 - G)D_2(F_2)(x_2, \tau_{12}, \tau_{22} + P, \tau_{23}) - D_1(F_2)(x_2, \tau_{12}, \tau_{22} + P, \tau_{23}) \\ &- 2\Omega\bar{u}_1 D_4(F_2)(x_2, \tau_{12}, \tau_{22} + P, \tau_{23}) + ((-2\bar{u}_3^2 + 2\tau_{33} + 2\bar{u}_1^2 - 2\tau_{11})\Omega_2 + G\bar{u}_3)C_2 + \\ &((4\bar{u}_3^2 - 4\bar{u}_1^2)\Omega_2 - 2G\bar{u}_3)C_4 + (4x_2\tau_{33} - 4\tau_{11}x_2)\Omega_2 C_1 - C_5\bar{u}_1 - C_4\bar{u}_3]\end{aligned}$$

$$\eta_{\tau_{22}} = \left(-2\,{x_2}^2{\Omega_2}^2 - P\right) C_2 + \left(-2\,{\Omega_2}^2{x_2}^3 - x_2 P\right) C_1 + \left(P - 2\,{x_2}^2{\Omega_2}^2\right) C_4 - x_2 C_9 + C_{11}$$

$$\eta_{\tau_{33}} = T\left(x_2, \bar{u}_1, \bar{u}_3, P, \tau_{12}, \tau_{22}, \tau_{23}, \tau_{13}, \tau_{33}, \tau_{11}, g_{12}, g_{22}, g_{23}, g_{13}, g_{33}, g_{11}\right)$$

$$\eta_{g_{22}} = C_{13}$$

$$\begin{aligned}\eta_{g_{13}} &= \left(-\tau_{23}\, C_2 + 2\, C_4 \tau_{23} + x_2 C_5 + C_8\right) \bar{u}_1 + \left(-\tau_{12}\, C_2 + 2\, \tau_{12}\, C_4 + C_6 x_2 + C_7\right) \bar{u}_3 + \\ &\qquad F_2\left(x_2, \tau_{12}, \tau_{22} + P, \tau_{23}\right)\end{aligned}$$

$$\eta_{g_{11}} = 2\left(-\tau_{12}\, C_2 + 2\, \tau_{12}\, C_4 + C_6 x_2 + C_7\right) \bar{u}_1 + F_1\left(x_2, \tau_{12}, \tau_{22} + P, \tau_{23}\right)$$

$$\begin{aligned}\eta_{g_{12}} &= \frac{1}{2\Omega_2}[(-4\Omega_2^3 U x_2^3 + 6\tau_{23} x_2 \Omega^2) C_1 - 4\Omega_2 (U x_2^2 \Omega_2^2 - \Omega_2 \tau_{23} x_2) C_2 - 4\Omega_2 (\bar{u}_1 x_2^2 \Omega_2^2 - \Omega_2 \tau_{23} x_2) C_4 \\ &\qquad (-2\Omega_2 \bar{u}_1 x_2 + \tau_{23}) C_9 + 2\Omega_2 (\Omega_2 x_2^2 C_5 + 2\Omega_2 x_2 C_8 + \bar{u}_1 C_{11} + C_{12}]\end{aligned}$$

$$\begin{aligned}\eta_{g_{23}} &= \frac{1}{2\Omega_2}[(-4\Omega_2^3 \bar{u}_3 x_2^3 + (2x_2^3 G - 6\tau_{12} x_2^2)\Omega_2^2) C_1 + 2C_2(-2\bar{u}_3 x_2^2 \Omega_2^2 + x_2(-2\tau_{12} + \\ &\quad x_2 G)\Omega_2) + 2C_4(-2\bar{u}_3 x_2^2 \Omega_2^2 + x_2(-2\tau_{12} + x_2 K)\Omega_2) + C_9(-2\bar{u}_3 x_2 \Omega_2 - \tau_{12} + x_2 k) \\ &\qquad - 2\Omega_2(2\Omega_2 x_2 C_7 + C_6 \Omega_2 x_2^2 - C_{11} \bar{u}_3 - C_{14})]\end{aligned}$$

$$\begin{aligned}\eta_{g_{33}} &= \frac{1}{\Omega_2}[-\Omega_2 F_1(x_2, \tau_{12}, \tau_{22} + P, \tau_{23}) + (2\bar{u}_3 x_2 \Omega_2 + \tau_{12} + x_2 k) C_5 - \\ &\qquad 2C_2 \tau_{23}(\Omega_2 \bar{u}_3 - \frac{G}{2}) + 4C_4 \tau_{23}(\Omega_2 \bar{u}_3 - \frac{G}{2}) \\ &\qquad + C_{15}\Omega_2 + 2C_8 \Omega_2 \bar{u}_3 - \tau_{23} C_{14}]\end{aligned}$$

Curriculum Vitae

Amirfarhang Mehdizadeh

Personal data:

Date of Birth: 8. Januar 1979
Place of Birth: Iran
Nationality: Iranian
Marital Status: Married

Educations:

09/1998 - 02/2002	Bachelor of Science in Mechanical Engineering University of Tehran, Tehran-Iran
04/2005 - 04/2007	Master of Science in Computational Mechanical and Process Engineering Technische Universität Darmstadt, Darmstadt-Germany

Employment:

10/2005 - 10/2006	Research assistant at the Institute of Turbomachinery Department of Mechanical Engineering Technische Universität Darmstadt
05/2007 - Present	PhD student at the Chair of Fluid Dynamics Department of Mechanical Engineering Technische Universität Darmstadt

Publications:

Kniesner, B., Saric, S., Mehdizadeh, A., Jakirlic, S., Hanjalic, K., Tropea, C., Sternel, D., Gauss, F. and Schaefer, M. (2007)
Wall Treatment in LES by RANS Models:
Method Development and Application to Aerodynamic Flows and Swirl Combustors.
ERCOFTAC Bulletin, , 72, , 33-40,

Mehdizadeh, A., Oberlack, M, Hosseinzadeh, A. (2009)
DNS and Modeling of a Turbulent Channel Flow with Wall-Normal Rotation.
In proceeding of the Sixth International Sympsium on Turbulence Shear Phenomena, Seoul, Korea pp. 557–562

Mehdizadeh, A., Oberlack, M. (2009)
A study of turbulent Poiseuille-Ekman flow at different rotation rates using DNS.
In proceeding of the 12th EUROMECH, European Turbulence Conference,
Marburg, Germany, pp. 393–396